JUN 15 1982

Y 3.N88:25/2334

NUREG/CR-2334

COMPLETED
228

ORI

Interphase Transport in Horizontal Stratified Cocurrent Flow

Prepared by R. J. Jensen, M. C. Yuen

**Department of Mechanical and Nuclear Engineering
Northwestern University**

**Prepared for
U.S. Nuclear Regulatory
Commission**

NOTICE

This report was prepared as an account of work sponsored by an agency of the United States Government. Neither the United States Government nor any agency thereof, or any of their employees, makes any warranty, expressed or implied, or assumes any legal liability or responsibility for any third party's use, or the results of such use, of any information, apparatus, product or process disclosed in this report, or represents that its use by such third party would not infringe privately owned rights.

Availability of Reference Materials Cited in NRC Publications

Most documents cited in NRC publications will be available from one of the following sources:

1. The NRC Public Document Room, 1717 H Street, N.W.
   Washington, DC 20555
2. The NRC/GPO Sales Program, U.S. Nuclear Regulatory Commission,
   Washington, DC 20555
3. The National Technical Information Service, Springfield, VA 22161

Although the listing that follows represents the majority of documents cited in NRC publications, it is not intended to be exhaustive.

Referenced documents available for inspection and copying for a fee from the NRC Public Document Room include NRC correspondence and internal NRC memoranda; NRC Office of Inspection and Enforcement bulletins, circulars, information notices, inspection and investigation notices; Licensee Event Reports; vendor reports and correspondence; Commission papers; and applicant and licensee documents and correspondence.

The following documents in the NUREG series are available for purchase from the NRC/GPO Sales Program: formal NRC staff and contractor reports, NRC-sponsored conference proceedings, and NRC booklets and brochures. Also available are Regulatory Guides, NRC regulations in the *Code of Federal Regulations*, and *Nuclear Regulatory Commission Issuances*.

Documents available from the National Technical Information Service include NUREG series reports and technical reports prepared by other federal agencies and reports prepared by the Atomic Energy Commission, forerunner agency to the Nuclear Regulatory Commission.

Documents available from public and special technical libraries include all open literature items, such as books, journal and periodical articles, and transactions. *Federal Register* notices, federal and state legislation, and congressional reports can usually be obtained from these libraries.

Documents such as theses, dissertations, foreign reports and translations, and non-NRC conference proceedings are available for purchase from the organization sponsoring the publication cited.

Single copies of NRC draft reports are available free upon written request to the Division of Technical Information and Document Control, U.S. Nuclear Regulatory Commission, Washington, DC 20555.

Copies of industry codes and standards used in a substantive manner in the NRC regulatory process are maintained at the NRC Library, 7920 Norfolk Avenue, Bethesda, Maryland, and are available there for reference use by the public. Codes and standards are usually copyrighted and may be purchased from the originating organization or, if they are American National Standards, from the American National Standards Institute, 1430 Broadway, New York, NY 10018.

GPO Printed copy price: $6.50

NUREG/CR-2334
R2, R4

Interphase Transport in Horizontal Stratified Cocurrent Flow

Manuscript Completed: April 1982
Date Published: May 1982

Prepared by
R. J. Jensen, M. C. Yuen

Department of Mechanical and Nuclear Engineering
Northwestern University
Evanston, IL 60201

Prepared for
Division of Accident Evaluation
Office of Nuclear Regulatory Research
U.S. Nuclear Regulatory Commission
Washington, D.C. 20555
NRC FIN B6188

I

BLANK PAGE

ABSTRACT

The problem of interfacial transport in cocurrent, horizontal stratified gas-liquid systems is considered. Local condensation heat transfer coefficients and interface shear stress were obtained from mass and force balances. These balances were based on gas phase pitot traverses at various streamwise locations. Laser anenemometer measurements of liquid mean and rms fluctuation velocities were made at similar locations. The laser anemometer data supported the value for the interface shear velocity obtained by the gas phase force balance.

Based on cocurrent stratified air-water flow data the noncondensing interface shear stress was found to be a function of the relative velocity between the phases and the liquid fraction. Incorporated into Linehan's relation for condensing flow shear stress, the correlation was found to estimate the shear velocity for the condensation data considered. Local condensation heat transfer coefficients and gas absorption mass transfer coefficients were found to be directly proportional to the shear velocity. If the inner scales u_* and ν/u_* are substituted into Lamont's models for the interface mass transfer coefficient, many features of the present correlation for scalar transfer are predicted. The correlations for interfacial shear stress and scalar trasport can be combined to yield an iterative technique suitable for an engineering analysis of the interfacial heat, mass, and momentum transfer in a single driving force cocurrent system.

BLANK PAGE

TABLE OF CONTENTS

Page
ABSTRACT.. iii
LIST OF TABLES.. vii
LIST OF FIGURES... viii

CHAPTER 1 INTRODUCTION.. 1

CHAPTER 2 LITERATURE REVIEW................................... 5

2.1 Predictive Models.......................... 5

2.1.1 Film Theory....................... 6
2.1.2 Surface Renewal Models............ 7
2.1.3 Eddy Cell Theories................ 10
2.1.4 Eddy Diffusivity Models........... 13

2.2 Transport Data............................. 19

2.2.1 Linehan's Condensation Data....... 21
2.2.2 Noncondensing Mass and Momentum Transport................ 22

2.3 Summary 27

CHAPTER - 3 EXPERIMENTAL FACILITIES........................... 28

3.1 Channel Design............................. 28
3.2 Instrumentation............................ 30

3.2.1 Instrumentation for Steam Side-Mass and Momentum Balance Measurements...................... 30
3.2.2 Laser Anemometer and Associated Systems................ 32
3.2.3 Data Analysis Programs............ 38

3.3 Experimental Procedure..................... 40

3.3.1 Steam Side Instrumentation........ 41
3.3.2 Laser Anemometer.................. 42

CHAPTER - 4 THEORETICAL CONSIDERATONS......................... 44

4.1 Comparison of Gas and Liquid Phase Resistances................................ 44
4.2 Formulation of a Scalar Diffusion Equation 47
4.3 Scalar Transport Models for the Interface.................................. 54

BEST DOCUMENT AVAILABLE

4.4 Theoretical Consideratons Relating To Interface Shear.............................. 57
4.5 Summary 61

CHAPTER - 5 RESULTS AND DISCUSSION........................... 63

5.1 Review of Velocity and Shear Stress Data for the Present Experiment................. 63

5.1.1 LDA Data for Water Only Flows..... 64
5.1.2 Cocurrent Steam and Water Results........................... 66
5.1.3 Interface Shear Results........... 73

5.2 Correlation of the Interfacial Shear....... 77

5.2.1 Air-Water Shear Stress Data Correlations...................... 77
5.2.2 Condensation Shear Stress Data Correlation....................... 81

5.3 Mass and Heat Transfer Results............. 83

5.3.1 Comparisons with Published Scalar Transport Correlations..... 83
5.3.2 Discussion of the Present Correlation....................... 86
5.3.3 Comparison of the Modified Lamont Models to the Present Results........................... 91
5.3.4 Experimental Estimates for Turbulent Velocity and Length Scales.......................... 93

5.4 Engineering Estimates for K................ 94

CHAPTER - 6 CONCLUSIONS 100

APPENDIX A.1 - CHARACTERISTICS OF A CONVERGING BEAM PAIR INCIDENT OF A MULTILAYER SYSTEM................. 103
APPENDIX A.2 - ESTIMATES OF LDA MEASUREMENT VOLUME DIMENSIONS.. 109
APPENDIX A.3 - BROADENING CONSIDERATIONS.......................... 114
APPENDIX B.1 - DERIVATION OF THE HEAT TRANSFER COEFFICIENT..... 116
APPENDIX B.2 - INTEGRAL ANALYSIS OF MOMENTUM TRANSPORT......... 118
REFERENCES... 120
NOMENCLATURE... 126
TABLES... 138
ILLUSTRATIONS.. 143

LIST OF TABLES

Page

2-1 Summary of Other Cocurrent Flow Experiments............ 138

5-1 LDA Test Matrix.. 139

5-2 Interface Shear Velocity Measurements................. 140

5-3 List of Symbols for Air-Water Shear Data............... 141

5-4 List of Symbols for Heat and Mass Transfer Data........ 142

BEST DOCUMENT AVAILABLE

LIST OF FIGURES

Page

3.1 Schematic Diagram of the Steam and Water Loop.......... 143

3.2 Channel View. Dimensions in Centimeters............... 144

3.3 Laser Anemometer and Optical Bench..................... 145

3.4 Incident and Scattered Propagation Vectors............ 146

4.1 Illustraton of T, S, and L States with Fluxes Indicated.. 147

5.1 Liquid Layer Velocity Profile, $w_L = 1.3$ kg/s, $w_g = 0$, $x = .157$m.. 148

5.2 Liquid Layer Velocity Profile, $w_L = 1.8$ kg/s, $w_g = 0$, $x = .157$m.. 149

5.3 Liquid Layer Velocity Profile, $w_L = 1.3$ kg/s, $w_g = 0$, $x = .586$m.. 150

5.4 Liquid Layer Velocity Profile, $w_L = 1.8$ kg/s, $w_g = 0$, $x = .586$m.. 151

5.5 Energy Spectra Taken at the Interface for $w_L = 1.1$ kg/s, $x = .157$m. 152

5.6 Energy Spectra Taken at the Interface for $w_L = 1.8$ kg/s, $x = .157$................................... 153

5.7 Data Matrix.. 154

5.8a Mean Liquid Velocity for Steam Run 294a, x =.157m...... 155

5.8b Mean Liquid Velocity for Steam Run 294a, x = .306m..... 156

5.8c Mean Liquid Velocity for Steam Run 294a, x = .586m..... 157

5.9a Mean Liquid Velocity for Steam Run 254, x = .157m...... 158

5.9b Mean Liquid Velocity for Steam Run 254, x = .586m...... 159

5.10a Rms Liquid Fluctuation for Steam Run 294a, x = .157m... 160

5.10b Rms Liquid Fluctuation for Steam Run 294a, x = .306m... 161

5.10c Rms Liquid Fluctuation for Steam Run 294a, x = .586m... 162

5.11 Ratio of Streamwise Interface Fluctuation to u_{*LDA}. 163

5.12a Liquid Fluctuation Spectra for Steam Run 254, $x = .586m$, $y_L = .3$ and 4mm 164

5.12b Liquid Fluctuation Spectra for Steam Run 294a, $x = .586m$, y_L is 3 to 4mm 165

5.12c Liquid Fluctuation Spectra for Steam Run 297, $x = .586m$, $y_L = 0$ and 6mm 166

5.13 Ratio of Laser Anemometer Profile Fit u_{*LDA} to u_{*FB} Derived from Force Balance 167

5.14a Streamwise Shear Velocity Profile Steam Run 254 168

5.14b Streamwise Shear Velocity Profile Steam Run 274 169

5.14c Streamwise Shear Velocity Profile Steam Run 294a 170

5.14d Streamwise Shear Velocity Profile Stream Run 294b 171

5.14e Streamwise Shear Velocity Profile Steam Run 297, File 92 172

5.14f Streamwise Shear Velocity Profile Steam Run 297, File 93 173

5.15 Plate's Correlation for Shear Stress 174

5.16 Ratio of Actual to Predicted Shear Velocities Using Plate's Correlation 175

5.17 $\tilde{U}$ vs. $\tilde{\tau}$ for $\tilde{U} < 17.6$ 176

5.18 $\tilde{U}$ vs $\tilde{\tau}\left(18.4 \frac{\delta_L}{\delta_c}\right)^{-\mu}$ for $\tilde{U} \geq 17.6$ 177

5.19 Ratio of Actual to Predicted Shear Velocities Using Eq. (5.5) and Eq. (5.6) 178

5.20 Ratio of Actual to Predicted Shear Velocities for Condensation Data Using Linehan's Model for τ^* 179

5.21 Asia et al.'s Correlation 180

5.22 Theofanous et al.'s Correlation 181

5.23 Linehan's Stanton Number Correlation 182

5.24 Nusselt Number vs. $u_{*}x/\nu$ with Eq. (5.11) and (5.14) Shown.......... 183

5.25 Present Correlation with Eq. (5.14) Indicated.......... 184

A.1 Incident Beam Geometry in Projection.......... 185

A.2 Incident Beam Geometry in Perspective.......... 186

A.3 Projection of Incident Beam in x'- y' Plane.......... 187

A.4 Incident Beam Path.......... 188

B.1 Geometry of Elements in Stratified Flow Integral Analysis.......... 189

B.2 Force Balance on Element in Gas Phase.......... 189

CHAPTER 1

INTRODUCTION

Concern for the safety of plant personnel and the general population in the neighborhood of nuclear power generation stations existed long before the now famous Three Mile Island incident, and was reflected by extensive research both in the United States and abroad. The thermal and hydraulic behavior of reactor coolant systems both during normal and emergency operation is an area of concern specifically because of the range of regimes that may be encountered.

Complementary experimental and analytical efforts have been undertaken to hopefully better understand individual reactor components and the system as a whole. A topic that has received much attention is the hypothetical loss of coolant accident (LOCA) and the procedures for introduction of emergency core coolant (ECC) to prevent overheating of the core. Experimental studies serve to improve analytical codes by providing correlations that can replace detailed calculations of such items as interfacial transport rates or confirm their accuracy.

Condensation phenomena during reactor reflood operations has been the object of much study. Violent waterhammer effects which can endanger piping are possible (Block (1980)). Condensation induced heating of the ECC and interface shear augmented by condensation momentum transport tend to increase the delay between ECC System (ECCS) activation and reflood completion. Studies of scaling parameters have been conducted in experimental models of reactor components. Other research has examined the condensation mechanism and related areas in experiments of simple geometry.

The efforts of Northwestern University are representative of the second type. One particular goal is to understand condensation induced interfacial heat and momentum transport for systems where the liquid side controls the condensation rate. In order to obtain accurate estimates of the transport rates, these effects have been studied in simplified geometries, including stratified flows. The problem is analogous to that of river reaeration and chemical process gas contactors where studies of liquid side limited gas absorption have been conducted in similar facilities. The potential thus exists for comparisons with a larger data base than would be available from condensation studies alone and hopefully of establishing a general interfacial transport correlation.

Previous work at Northwestern has included experimental studies by Davidson (1978) and Lee (1979) in cocurrent, stratified steam and water loops. Davidson measured velocity and temperature profiles and obtained overall liquid side heat transfer coefficients for his two dimensional channel. In a system of improved design, Lee obtained heat transfer coefficients over the region from the entrance to the locations of traversable pitot probes in the gas phase. Since almost 80% of the steam typically was condensed, a mass balance on the steam side yielded an accurate estimate of the amount of the condensation flux. Lee proposed an experimental correlation for the liquid side Stanton number based on the average heat transfer coefficient from the entrance to the measurement station. Together with water film thickness measurements, Lee's data have been analyzed by Daly and Harlow (1980) using a two stream numerical analysis. Reasonable agreement is found between analysis and experiment when the condensation rate is related to the calculated root mean square turbulence intensity.

The present work was undertaken in a new facility with the goal to improve the reliability of the measurements which in some cases required a substantial correction factor based on a calibration. Lim (1981) has taken condensation data in this facility over a wide range of conditions using improved techniques. With more reliable data, it was hoped that accurate local heat transfer coefficients could be calculated. This was deemed important because the rates of change of the conditions affecting the condensation rate such as gas velocity and liquid subcooling were found to be large near the entrance. Acquisition of a laser anemometer system made complementary local measurements of the liquid turbulence possible. In turn, these local values could confirm and improve the accuracy of models such as the one used by Daly and Harlow. In a sense, continud improvement of the experimental results is part of an iterative process between analysis and experiment which would ideally converge to a correct understanding of the physics and lead to engineering estimate formulas that are reasonably easy to apply.

In summary, the goals of the research are the following:

1. To obtain the local heat and momentum transport for horizontal, cocurrent condensing steam and water flows at the Northwestern University facility;
2. To compare scalar (heat or mass) and momentum measurements from other facilities, correlate with the Northwestern data where possible, and suggest an interfacial transport model;
3. To validate formulas that, even if less accurate, are useful in an engineering design sense.

To implement these goals four tasks are proposed:

1. The present data of Lim will be analyzed for local heat transfer and interface shear values;
2. LDA measurements of the liquid layer will be made for conditions at which local values were obtained;
3. The data will be tested against previously published and newly hypothesized models for scalar transport in an attempt to find the correct model;
4. Engineering design formulas will be sought that relate the transport rate to readily estimated quantities such as the average phase velocities and temperatures.

CHAPTER 2

LITERATURE REVIEW

The following review will be divided into two subsections. The first section deals with a review of theoretical attempts to correlate heat and mass transfer at a liquid gas interface. The second part discusses published experimental data on interfacial transport which are later incorporated into attempts to obtain a correlation. Shear velocities where noted are always based on the liquid density such that

$$u_* \equiv \left(\frac{\tau_b}{\rho}\right)^{1/2}$$

where τ_b is the shear at a boundary of the liquid flow and ρ is the liquid density. Without a subscript u_* is the interface shear velocity while u_{*f} is a solid wall shear velocity.

2.1. Predictive Models

Many previous efforts to predict the transport at a gas-liquid interface can be classified into two approaches. These approaches are quasi-laminar diffusion theories and eddy diffusivity formulations. It is possible to draw comparisons and illustrate similarities in the final forms of these efforts by expressing all the results as mass transfer coefficients. The reason for the mass transfer coefficient presentation is that these models were developed to predict gas absorption due to a concentration driving force. The extension of these models to the prediction of heat transfer coefficients is straightforward when, as shown in the theoretical section, the thermal gradient is the dominant driving force.

A brief summary of the motivations for the two modelling approaches is in order. The quasi-laminar diffusion theories postulate specific flow structures near the interface and solve either the steady or nonsteady laminar diffusion equation to obtain the mass transfer coefficients. Three fundamental quasi-laminar models are discussed: film theory, surface renewal theory, and eddy cell theory. Film theory postulates that the transport is controlled by steady laminar diffusion through thin stagnant films in the gas and liquid phases at the interface. Outside the film region the flow is fully turbulent and offers no resistance. Surface renewal theory assumes that the flow circulates elements of fluid from the bulk to the interface where an unsteady laminar diffusion process occurs for a time equal to the characteristic time of the flow. Eddy cell theories specify the existance of a laminar cellular flow supposedly representative of turbulent eddies at the interface. These cells circulate fluid from the bulk to the interface where a steady, laminar diffusion process occurs until the fluid reaches the streamwise cell boundary and is convected back to the bulk. By contrast, eddy diffusivity theories start with a model for the turbulent eddy diffusivity. This is incorporated into either a film or surface renewal theory or is used in direct numerical simulation of the entire flow field. Advantages and limitations of each model will be discussed individually.

2.1.1 Film Theory

One of the earlist efforts to estimate gas absorption on liquid surfaces is a quasi-laminar approximation due to Lewis and Whitman (1924) who proposed that at the interface of fully turbulent flows there exist thin stagnant films in the gas and liquid phases. The one dimensional steady stagnant flow diffusion equation is solved and the mass transfer coefficient, k_L, is found to be

$$k_L = D/\delta \tag{2.1}$$

where D is the laminar diffusion coefficient and δ is the diffusion layer thickness.

However (2.1) simply transfers the problem to that of an a priori estimation of an effective film thickness which in general is found to be flow dependent. The assumption that a purely laminar diffusion layer exists at the interface uninterrupted in space or time by the bulk phase turbulence is also somewhat artificial. Film theory is often used in conjunction with an eddy diffusivity (D_t) model to predict δ and thus k_L as well. In such a case, D in the stagnant film equation is replaced by the effective diffusivity, $D + D_t$. This point will be examined further in the section on eddy diffusivity models.

2.1.2. Surface Renewal Models

Higbie (1935) originated the concept of a renewal or replenishment of the surface with unsaturated liquid at a frequency set by the flow. While in contact with the surface, elements of fluid undergo an unsteady laminar diffusion process. For a constant solute flux and characteristic time t_e, k_L is

$$k_L = 2\left[\frac{D}{\pi t_e}\right]^{1/2} \tag{2.2}$$

The problem is shifted to the determination of t_e, which is dependent on the turbulence. Equation (2.2) is also known as penetration theory.

In an attempt to generalize Higbie's model to one where a hopefully more realistic representation of the exposure time is employed, Danckwerts

(1951) postulated a probability density function for the fractional surface area having an exposure time between t and t+dt

$$\Phi(t)dt = s\ \exp[-st]dt \qquad (2.3)$$

where s is a characteristic turbulence frequency. Instead of substitution of a fixed time t_e, the time dependent solution for the flux is integrated from t=0 to $t \rightarrow \infty$ using $\Phi(t)$ as a weighting function. The result is

$$k_L = (Ds)^{1/2} \qquad (2.4)$$

Although the form is the same as (2.2) it might be supposed that the constant term (unity) is better justified in (2.4) due to a more realistic modelling of the turbulence.

O'Connor and Dobbins (1958) performed a similar analysis using Danckwerts' $\Phi(t)$ function, but restrict the concentration gradient to the finite depth, δ. By contrast, Higbie and Danckwerts both assumed that the gradient vanished at infinity. The solution to the steady one dimensional laminar diffusion equation is

$$k_L = (Ds)^{1/2}\coth[\frac{s\delta^2}{D}]^{1/2} \qquad (2.5)$$

For vanishing s or δ, the result of film theory Eq. (2.1) is recovered, while for large values of the hyperbolic cotangent argument such that

$$\coth[\frac{s\delta^2}{D}]^{1/2} \approx 1$$

Danckwert's result, Eq. (2.4), is recovered. The value of the hyperbolic cotangent term is .99 when the function argument is

$$(\frac{s\delta^2}{D})^{1/2} = 2.65$$

which may be considered a critical value of this group. At this value and above, k_L follows the surface renewal law while below this value (for thin, quiescent films) film theory holds.

Values of s are based on the assumption that the renewal rate equals the ratio of the turbulence velocity scale to the mixing length, which is set proportional to the channel depth. The surface renewal result for nonisotropic turbulence is

$$k_L = \left(\frac{D u_{*f}}{\kappa\ \delta_L}\right)^{1/2} \tag{2.6}$$

where κ is the von Karman constant and δ_L is the channel depth. For deep channels such as rivers, O'Connor and Dobbins suggest the flow is effectively isotropic and recommend

$$k_L = \left(D\ U_L/\delta_L\right)^{1/2}$$

where U_L is the mean liquid velocity.

Obviously the nonisotropic and isotropic solutions for k_L are reasonably straightforward to apply. However in the case of a sheared interface an estimate of the renewal rate s might well depend on the interface shear and an interface length scale rather than floor shear and channel depth.

Hughmark (1971) proposed a type of surface renewal model for transport from a solid wall in pipe flow based on an estimate of a streamwise length scale associated with the turbulence burst phenomenon. Citing data for pipe flows available at the time, a burst frequency T_B^{-1} where

$$T_B^{-1} = 9.1 \times 10^{-3}\ u_{*f}^2/\nu$$

is assumed. Here u_{*f} is the pipe wall shear velocity. The distance between fluctuations based on T_B and the laminar sublayer velocity profile was estimated to be

$$x_B = 236\ \nu/u_{*f} \tag{2.7}$$

Together with an estimate for the effective value of the free stream velocity U_∞

$$U_\infty \sim (\text{const})\ u_{*f}$$

the value for x_B is substituted into the Pohlhausen result for laminar flow heat transfer (Schlichting (1968)). Cast in the form of a mass transfer relation

$$k_L = .078\ u_{*f}\ Sc^{-2/3} \tag{2.8}$$

Hughmark's model is in close agreement with Harriot and Hamilton's (1965) experimental pipe flow result which is

$$k_L = .0816\ u_{*f}\ Sc^{-2/3} \tag{2.9}$$

This agreement suggests that the appropriate characteristic length and velocity are based on "inner" or "wall" scales. Such scaling emphasizes the role of the flow immediately adjacent to the interface where transport is occurring. Since the present work will attempt to correlate transport data for sheared interfaces, the success of Eq. (2.8) suggests that inner scales might be appropriate for a model of cocurrent flow transport. This point will be examined again in the theoretical chapter.

2.1.3. Eddy Cell Theories

Fortescue and Pearson (1967) postulate the existence of large eddies near the surface which control the mass transfer rate across the interface. These eddies are idealized as counter-rotating cells with square cross sections in the plane of the streamwise and transverse coordinates. The authors postulate a cell velocity field and integrate the two dimensional steady diffusion equation. An average result is obtained for k_L

$$k_L = 1.46\ \left(D\ u'/\Lambda\right)^{1/2} \tag{2.10}$$

where u' is the rms turbulence fluctuation and Λ is the turbulence macroscale.

By contrast, Lamont (1966) develops models which emphasize the small scale eddy contributions to the transport. Square eddy cells are again postulated. The stream function of the motion is obtained from a simplified form of the steady Navier-Stokes equations in which viscous dissipation balances pressure gradients. With the boundary condition

$$\frac{\partial u}{\partial y} = 0$$

where u is the streamwise cell velocity at the interface, the fundamental solution of the laminar diffusion equation is

$$k_{LFS} = .445 \left(Du_c/\ell\right)^{1/2} \tag{2.11}$$

where k_{LFS} is the free surface mass transfer coefficient, u_c is the cell velocity scale and ℓ is the cell length scale. For the solid wall boundary condition the solution is

$$k_{LS} = .815 \left(u_c\right)^{1/3}\left(\frac{D}{\ell}\right)^{2/3} \tag{2.12}$$

where k_{LS} is the solid wall mass transfer coefficient.

With ℓ set equal to

$$\ell = \pi/n_w$$

where n_w is the wavenumber, u_c is estimated from

$$u_c \sim \left(n_w E(n_w)\right)^{1/2}$$

where $E(n_w)$ is the Kovasznay turbulent energy spectrum (Hinze (1975)). The fundamental mass transfer coefficient solutions are found by integrating over the range of the spectrum. Results for the overall transport coefficients are for the free surface and solid wall

$$k_{LFS} \sim Sc^{-1/2}(\varepsilon\nu)^{1/4}$$

and (2.13)

$$k_{LS} \sim Sc^{-2/3}(\varepsilon\nu)^{1/4}$$

where ε is the turbulence dissipation rate. Although Lamont's models do not explain his bubble flow absorption data, the concepts evolved are interesting and will be reexamined later.

Theofanous et al. (1976) propose a synthesis of large and small eddy cell models. The constants and range of applicability of each model is based on comparisons with open channel flow, bubble flow and jet flow data. Below a critical turbulence Reynolds number Re_t of 500 where

$$Re_t \equiv u'\Lambda/\nu$$

the large scale model is appropriate

$$k_L = .7\ I(t_T)\ \left(\frac{Du'}{\Lambda}\right)^{1/2} \tag{2.14a}$$

where $I(t_T)$ is a time dependent function which represents inlet effects such that with the dimensionless time scale t_T

$$t_T = \sqrt{2}\ t_{ex}/(\Lambda/u') \tag{2.14b}$$

the function is given by

$$I(t_T) = 1. + .44/t_T \quad \text{for} \quad t_T > .85$$

Here t_{ex} is the time of interface exposure from the inlet based on the liquid velocity, and t_T is the ratio of t_{ex} to the large eddy time scale, Λ/u'.

For turbulent Reynolds numbers above 500, a small eddy model is postulated to apply

$$k_L = .25\ \sqrt{D}\ \left(\frac{\varepsilon}{\nu}\right)^{1/4} \tag{2.15}$$

The dissipation rate ε is estimated from Batchelor (1967) where

$$\varepsilon = \frac{u'^3}{\Lambda} \tag{2.16}$$

A similar set of expression for large and small scales for the heat transfer coefficient has been proposed by Bankoff (1978). Thus in terms of a Nusselt number

$$Nu_t = .7\ I(t_T) Re_t^{1/2}\ Pr^{1/2} \qquad Re_t < 500 \qquad (2.17a)$$

$$= .25\ Re_t^{3/4}\ Pr^{1/2} \qquad Re_t > 500 \qquad (2.17b)$$

Here the Nu_t is defined by

$$Nu_t = h\Lambda/k$$

where k is the thermal conductivity and h is the heat transfer coefficient.

The data considered by Theofanous include only shear free interface conditions. Hence the sheared interface channel data base considered in this work is a new test of the validity of the model.

2.1.4. Eddy Diffusivity Models

Levich (1962) proposed that the limiting resistance is due to a diffusional sublayer near the surface similar to film theory. The thickness of the diffusional sublayer, δ , is obtained by solving for the location where the laminar and turbulent diffusion coefficients are equal so that

$$D = D_t(\delta)$$

where D_t is the eddy diffusivity. According to Levich

$$D_t \sim u'\ y_L^2/r_L$$

where y_L is the distance to the surface and r_L is the thickness of the region of surface tension damped turbulence near the interface. Note that D_t vanishes at $y_L = 0$. The depth of the damped region obtained from a force balance between the turbulent momentum flux normal to the interface and the capillary pressure acting on a surface distortion of radius proportional to r_L . Thus r_L is approximated by

$$r_L = \sigma/\rho(u')^2 \qquad (2.18)$$

where σ is the surface tension. Then δ is found from

$$\delta = \left(\frac{D\sigma}{\rho(u')^3}\right)^{1/2}$$

and from film theory (Eq. (2.1))

$$k_L = \frac{D}{\delta} = \left(\frac{\rho D(u')^3}{\sigma}\right)^{1/2} \tag{2.19}$$

This model complements film theory by estimating δ . However, pressure drag which causes wave growth in the case of a cocurrent gas phase flow is not considered in (2.18). The importance of pressure forces relative to capillary effects is expressed by the Weber number which is defined as

$$We \equiv \rho_g\, U_g^2 r_L/\sigma = \rho_g\, U_g^2/\rho(u')^2$$

where r_L is defined in (2.18). For We much greater than unity, it is expected that the scale of the surface distortion r_L is governed by the pressure distribution over the wavelet rather than a balance between the turbulent liquid momentum flux and surface tension. Equation (2.19) is likely more appropriate to flows without interfacial pressure forces. Davies (1972) shows examples of the application of the Levich model to stirred vessels and liquid jets.

Kishinevsky (1955) postulates that the total effective diffusivity is the sum of laminar and turbulent diffusivities

$$D_{eff} = D + D_t$$

and is a constant in the neighborhood of the interface. If a surface renewal model is postulated, using the effective diffusivity a result analogous to (2.2) is obtained

$$k_L = 2\left(\frac{D_{eff}}{\pi t_e}\right)^{1/2} \tag{2.20}$$

If the eddy diffusivity is large, the mass transfer coefficient should be independent of the laminar diffusion coefficient. This effect should be quite obvious from an examination of the data over a wide range of scalar diffusivities. Kishinevsky and Serebryansky (1956) conclude that D_t does not vanish at the interface and is larger than D on the basis of vigorously stirred vessel experiments.

King (1966) postulates an eddy diffusivity of a general form given by

$$D_T = ay^m \tag{2.21}$$

where a is a dimensional coefficient and m is an exponent both chosen to fit experimental data. He obtains analytical solutions of the nonsteady mass transfer equation similar to surface renewal theory. A dimensionless phase contact time t_K is given by

$$t_K = a^{2/m} \, t_a \, D^{\left(\frac{2}{1-m}\right)} \tag{2.22}$$

where t_a is the surface age, which is the time elapsed since the last surface renewal. To within a factor of 1/2, the penetration solution is recovered for m=2 and t_K small

$$k_L = \left(\frac{D}{\pi t_a}\right)^{1/2} \tag{2.23}$$

For large t_K and m=4

$$k_L = .9a^{1/4}D^{3/4}$$

In order to determine a, King approximates Calderbank and Moo-Young's (1961) semiempirical result with the following

$$k_L = .25 \, Sc^{-3/4}(\varepsilon\nu)^{1/4} \tag{2.24}$$

Here the value of -2/3 for the Schmidt number exponent in Calderbank and Moo-Young's correlation has been replaced by -3/4. For wetted wall column data, a relation of the form of Eq. (2.23) is reasonable for small t_k while for large t_K , (2.24) yields a better prediction.

For open channels and rivers, King recommends a model based on Krenkel and Orlob's (1962) results and dimensional analysis to accommodate Danckwerts' theory such that

$$k_L \sim (\varepsilon \delta_L)^{1/3} (\frac{D}{\nu})^{1/2} = (Ds)^{1/2} \qquad (2.25)$$

Equation (2.25) does not follow from his analysis and thus seems to indicate that the proper model for the mass transfer depends on the geometry and source of turbulent agitation.

Ueda et al. (1977) postulate an eddy diffusivity for open channel flow which is dependent on surface wave damping factors. This approach is similar to that of the widely used Van Driest model which accounts for solid wall turbulence damping. Levich's (1962) model for a surface wave in a viscous fluid is used to estimate the wavelength dependent amplitudes of the vertical and tangential velocities which when normalized by the values at the free surface constitute the interface damping factors. The eddy diffusivity is proportional to a polynomial consisting of products of the floor and interface motion damping factors. To determine the value of the constants in the surface wave damping factor, a characteristic wavelength was obtained from a curve fit to the eddy diffusivity profile in a heated open channel flow. The authors recommend

$$\lambda = 140 \quad \nu/u_{*f} \qquad (2.26)$$

Near the interface with this value for λ the eddy diffusivity simplifies to

$$D_t = 4.33 \times 10^{-4} \nu \, (\frac{y_L u_{*f}}{\nu})^3 \qquad (2.27)$$

where y_L is the distance from the interface. From the solution of the stagnant film diffusion equation (film theory) the mass transfer coefficient is

$$k_L = .0626\, u_{*f}\, Sc^{-2/3} \qquad (2.28)$$

The authors show that this estimate for k_L correlates a wide variety of river and laboratory channel flow data, particularly the open channel data of Krenkel and Orlob (1962) for which there was no wind shear. It is interesting to note the similarity in form between Hughmark's pipe flow relation (2.8) and Eq. (2.28) which differ by a constant. However, in the case of pipe flow the primary transport resistance is at the pipe wall while for open channel flow the resistance is at the free surface. For flows with shear at one boundary only, these relations would seem to imply that the shear velocity scales the mass transfer coefficient, whether mass transfer occurs at the sheared boundary or not.

Daly and Harlow (1980) model the eddy viscosity and the condensation rate in a numerical simulation of Lee's (1979) experiments. A turbulence kinetic energy balance was used to estimate the effective turbulence intensity at each station. With a turbulent Prandtl number of unity, the eddy viscosity ν_t and eddy thermal diffusivity k_t were estimated from

$$\nu_t = \frac{k_t}{\rho c_p} \equiv .03\, \delta_L \left(2q_L\right)^{1/2}$$

where q_L is the turbulence kinetic energy and δ_L is the liquid layer thickness. The condensation rate was given by

$$G = \frac{J_c \rho\, c_p}{H_{fg} d} \left(T_S - T_L\right) S_L {q_L}^{1/2} \qquad (2.29)$$

Here G is the condensation mass flux, J_c is a constant, c_p is the liquid specific heat, H_{fg} is the heat of vaporization, d is the thermal boundary layer thickness, S_L is the turbulence decay length, T_S is the saturation temperature, and T_L is the liquid temperature at the edge of the thermal boundary layer. The form of the heat transfer coefficient implied by Eq. (2.29) will be considered in the discussion of the results. As mentioned in the introduction, the code predicted the effects of varying inlet parameters in Lee's data reasonably well. This equation implies a proportionality between the computed heat transfer coefficient and the computed turbulence intensity. Comparison of the measured heat transfer coefficient and a characteristic turbulence velocity scale of the present more accurate data set is certainly desirable.

In summary, a variety of models for transport across a fluid interface have been proposed in the literature. Most of the models are for flows where shear is applied at a wall rather than the interface and it is thus likely that these models may require modification to emphasize turbulent velocities and length scales at the sheared interface. This is because most of the models postulate a dependence on concentration gradients which should be sensitive to the existence of a near surface shear flow if some similarity exists between scalar and momentum transport, such as the Reynolds analogy. This point will be further examined in the theoretical section.

Many of the models, particularly the surface renewal and eddy cell theories assume that intermittent or cellular laminar diffusion processes control the interface transport. However, equivalent final results for k_L can be obtained independent of whether a turbulent diffusivity or a quasi-laminar flow structure is postulated, as shown by Eq. (2.28) of Ueda et al. and Eq. (2.8) of Hughmark. Hence, the final correlation for k_L will not indicate which of these two approaches is most correct. The best that can be hoped for is an elimination of some of the candidate models and that a consistent hypothesis can be recommended.

2.2. Transport Data

Several sets of transport data from channel flows with wind or vapor shear at the interface will serve as a data base, together with the present experimental results.

Besides data from the Northwestern University condensation experiment, the data sets included are:

1. Linehan's (1968) condensation experiment.
2. Gas absorption and shear stress data from the two contactors at Toulouse (Asia et al. (1981)).
3. Mattingly's (1977) gas absorption and shear stress data.
4. Eloubaidy's (1969) gas absorption data.
5. Plate's (1966, 1969) shear stress data.
6. Cohen's (1964, 1968) shear stress data.
7. Theofanous's (1975) shear stress data.
8. Wu's (1968) shear stress data.

Table 2-1 summarizes the facility dimensions and inlet Reynolds number ranges. Here

$$Re_g \equiv 2U_g b\ \delta_g/[\nu_g(b + \delta_g)]$$

in which Re_g is the gas Reynolds number based on the hydraulic diameter, U_g is the average gas velocity, b is the channel width, δ_g is the gas layer height, and ν_g is the gas kinematic viscosity. The liquid Reynolds number based on thickness is

$$Re_L = U_L\delta_L/\nu\ .$$

By restricting the data considered to that with nonzero interface shear, and hence hopefully of similar flow structure near the interface, a less ambiguous picture of the transport mechanism may be obtained. However, even with this restriction, some variance can be expected due to the fact that data from both developing and reasonably developed cocurrent flows are included. The data base also incorporates both condensation and gas absorption results and a wide range of gas and liquid phase thicknesses.

The inclusion of gas absorption data with condensation data is reasonable if in each case a single driving force in the liquid, due either to a concentration or temperature difference, is dominant in the scalar transfer process. The suitability of the single driving force hypothesis will be discussed in the theoretical section. It is sufficient to note that for condensation on a subcooled liquid film in a single component system and for absorption of a slightly soluble gas on a liquid, conditions for this single driving force are met so that the governing scalar diffusion equations are identical in form. In these cases, the heat and mass transfer coefficients are likely to be similar functions of the interface shear, the ratio of viscous to transport scalar diffusivities (that is, the Prandtl number in the case of heat transfer and the Schmidt number in the case of gas absorption), and the Reynolds numbers of the system. The functional relationship between the heat or mass transfer coefficients and the corresponding diffusivity ratio should be quite clear for this data set because the range of this ratio is almost three orders of magnitude. Specifically Prandtl numbers range between

$$2 \lesssim Pr \lesssim 10$$

while the Schmidt number range is approximately

$$400 \lesssim Sc \lesssim 700$$

It can be hoped that if the mechanism of transport is common and the functional form of the heat or mass transfer coefficient is well defined for the sheared interface data, a better understanding in the case of transport with vanishing interface shear will also be possible.

2.2.1. Linehan's Condensation Data

In addition to the results of the Northwestern University horizontal cocurrent steam and water loop summarized by Lim (1981), one other condensation experiment will be considered. Linehan's (1968) well known experimental work which included a study of the condensation of saturated steam on subcooled thin films in cocurrent, two-dimensional flow bears a strong resemblance to the present work. The experimental facility was much smaller, however, as shown in Table 2.1, and the liquid flowed in a thin film that ranged up to a millimeter in thickness, as measured by conductivity probes. Inlet gas and liquid phase Reynolds numbers are shown.

Heat transfer coefficients were computed by a first law balance on the liquid layer. Thermocouples spaced at even intervals in the streamwise direction were assumed to measure the average liquid temperature. The interface shear stress was implied by an integral analysis which incorporated a model for the augumentation of the adiabatic shear by condensation. To estimate the adiabatic shear, Linehan correlated Cohen's (1964) data for the three dimensional wave regime by the following law

$$\begin{aligned} f &= 7.5 \times 10^{-5}\, Re_L + .0272 \qquad \text{for } Re_L < 340 \\ f &= 9.26 \times 10^{-6}\, Re_L + .0524 \qquad \text{for } Re_L > 340 \end{aligned} \tag{2.30}$$

The total shear stress with condensation, τ^*, was modeled after Carpenter and Colburn (1951)

$$\tau^*/\tau = 1 - b_f \tag{2.31}$$

for a blowing parameter b_f given by

$$b_f = -G\, U_g/\tau \tag{2.32}$$

with

$$\tau = \rho_g \frac{f}{8} U_g^2$$

where U_g is the average gas velocity, G is the condensation rate, ρ_g is the vapor density, and f is given by Eq. (2.30). By way of comparison Kays and Crawford (1980) recommend the Mickley et al. relation

$$\tau^*/\tau = \frac{b_f}{e^{b_f} - 1} \tag{2.33}$$

for suction boundary layers.

Heat transfer results were expressed by a simple constant liquid Stanton number relationship based on a constant eddy diffusivity model

$$\frac{h}{\rho U_L c_p} = .0073 \tag{2.34}$$

Equation (2.34) has been incorporated into the TRAC-P1A reactor analysis code (Rohatgi and Saha (1980)) for annular flow heat transfer. By way of comparison Linehan found his heat transfer coefficients a factor of 2.5 to 4.2 times larger than Carpenter and Colburn's correlation for annular flow in a tube type condenser which is

$$h = .045\rho\, c_p u_* Pr^{-1/2} \tag{2.35}$$

2.2.2. Noncondensing Mass and Momentum Transport

A series of horizontal cocurrent air-water gas absorption experiments have been performed at the Institut de Mecanique des Fluides at Toulouse. A summary of gas absorption data based on several theses is given by Asia, et al. (1981). Two facilities were used. In the smaller gas contactor the flow was fully developed at the measurement stations whereas for the larger contactor the gas phase boundary layer at the interface was observed to grow continuously.

Absorbed gas concentrations are measured in the liquid by traversable conductivity probes for CO_2 and floor mounted polarographic probes for O_2. Interfacial shear stress is calculated from the pressure drop and the elevation of the maximum in the gas velocity profile for the small contactor, after Hanratty and Engen (1957). Following Cohen and Hanratty (1968), the effective interfacial roughness was obtained from the Colebrook formula (Schlichting (1968)) for the small facility. Turbulent shear stress measurements in the gas and liquid phases and curve fitting of the logarithmic velocity profiles in the gas phase were used to obtain the interface shear velocity for the large contactor. The fitted profiles also yielded the effective interfacial roughness.

Overall Asia et al. observed their results were approximated by

$$.1 \leq \frac{k_L Sc^{1/2}}{u_*} \leq .2 \qquad (2.36)$$

where k_L is the mass transfer coefficient and u_* is the interfacial shear velocity. A Theofanous type of small eddy model given by

$$\frac{k_L Sc^{1/2}}{u_*} = .5 \left(\frac{u_* k_s}{\nu}\right)^{-.25} \qquad (2.37)$$

where k_s is the effective roughness and $u_* k_s/\nu$ is the roughness Reynolds number, is compared to the data for

$$\frac{u_* k_s}{\nu} \gtrsim 100$$

and

$$\frac{\rho}{\rho_g} \frac{u_*^2}{g\delta_L} > 2 \quad .$$

A few data are shown to satisfy (2.37) for the conditions indicated. However, the bulk of the data are represented by (2.36) for

$$10 < \frac{u_* k_s}{\nu} < 10^4$$

and do not appear to be strongly dependent on the roughness Reynolds number.

Mattingly (1977) performed a set of oxygen absorption experiments at the Institute of Statistical Mechanics of Turbulence at Marseille. Oxygen concentrations in the liquid were established using the Winkler technique. The interfacial friction velocity and effective roughness were obtained from curve fits to gas phase velocity profiles. Several measurements were made of wave height, wave length, and wave speed. Generally, the magnitudes of all three characteristics increased with air velocity and fetch.

Eloubaidy (1969) has made measurements of O_2 absorption in a wind-water tunnel at Colorado State University. Absorption measurements with and without air flowing were made with the aid of Beckman oxygen analyzers and liquid sampling probes. For the wind driven case the average wave height, wave length, and frequency were established using capacitance probes. Wave height, speed, and length increased with each fetch and wind speed. The interface shear stress was estimated from Hidy and Plate's (1966) correlation which will be discussed presently along with several other works coauthored by Plate.

Plate has produced a series of papers dealing with experimental wave statistics and comparisons with existing wave growth rate theories. Plate and Hidy (1966) conducted experiments with a wind-wave facility having a standing water pool of variable depth. Interface shear stress, drift currents, wave speed, wavelength, wave amplitude spectra, and growth rates were the principal measurements. Interfacial shear stress was determined by pressure drop measurements for most of the data except for a few obtained from curve fits to the logarithmic velocity profile in the gas phase. One of the more notable results was the dimensional correlation for shear stress

$$\tau = 6.67 \times 10^{-4} \rho_g U_g^3 \qquad (2.38)$$

where U_g is the average gas velocity. If the maximum velocity is related to the average velocity by

$$.8\, U_\infty = U_g$$

then

$$\tau = 3.41 \times 10^{-4} \rho_g U_\infty^3 \qquad (2.39)$$

As in other similar efforts, wave amplitude, wavelength and wave speed of the dominant waves were found to increase with fetch and wind velocity. In examining the growth rates near the conditions of wave inception, Plate, Chang and Hidy (1969) identified qualitatively the existance of a critical wind speed for a given fetch at which waves would first be visible. The critical wind speed was indicated as being in the neighborhood of 3 m/s although a critical velocity as high as 4 m/s was found for one data set at 3.5 meters downsteam. From gas phase velocity profiles, Chang, Plate and Hidy (1971) infer that lee side separation occurs for the dominant waves. This observation agrees with Levich's (1962) hypothesis.

Cohen and Hanratty (1968) have measured the shear stress over thin films in fully developed flow of liquids with varying viscosity. Film thicknesses were typically 2.5 to 5mm. Streamwise pressure gradients and transverse gradients in the streamwise velocity were recorded. Wave amplitude was continuously monitored using a light absorption technique.

The shear stress was computed using the method of Hanratty and Engen (1957).

Shear coefficients are shown to be functions only of the ratio δ_L'/δ_{gmax} where δ_L' is the wave amplitude and δ_{gmax} is the displacement of the gas velocity maximum. The shear coefficient is related to the effective sand grain roughness using the Nikuradse formula (Schlichting (1968)). For

$$\frac{\delta_L' u_*}{\nu} > 12$$

it is found that the roughness and wave amplitude have a constant relation

$$k_s/\delta_L' = 3\sqrt{2} \quad .$$

Theofanous et al. (1975) have made similar measurements with a cocurrent air-water facility but for thicker water films of order 1 cm. The method of determining the interfacial shear stress is again that of Hanratty and Engen (1957). Pressure drop measurements are found to be well represented by the Lockhart-Martinelli correlation (Wallis (1969)) multiplied by a factor of .47.

Wu (1968) has performed measurements of wave statistics and gas phase velocity profiles over a standing pool. The nominal depth was 1.2m. Effective roughness and interface shear velocity were obtained from a curve fit to the logarithmic portion of each velocity profile. A conductivity probe was used to measure dominant wave amplitude. A device for detecting the light reflected from ripples was used to obtain the frequency of the smaller waves. Wu shows agreement between his data and Charnock's (1955) relation which is

$$\frac{gk_s}{u_*^2} \rho_g/\rho = .337 \qquad (2.40)$$

for "high wind velocities" when the roughness is proportional to the wave amplitudes and proposes a surface tension dominated relation

$$\frac{\rho^2 u_*^2 k_s}{\rho_g \sigma} = \text{const} \qquad (2.41)$$

for lower velocities. He further suggests that a shear discontinuity between the gas and liquid phases exists to account for growth in wave energy, and that form drag is the primary momentum exchange mechanism.

2.3. Summary

A wide variety of theoretical models and experimental data have been reviewed. With the exception of King's (1966) work and Theofanous et al.'s. (1976) model, generally correlations have been applied to data sets that are predominantly from one source in each case. It is desirable to examine model-data combinations for these data and the Northwestern University stratified, cocurrent condensing flow results with the hope of obtaining a unified correlation for the case of scalar transport at a sheared gas-liquid interface. Other conditions such as bubbly flows may have a significantly different turbulence structure which could make the matter of finding a general correlation more difficult. It is felt that limiting the data set to conditions for which the turbulence structure might be expected to be reasonably similar in the region of the interface should give a clearer picture of the relationship between the turbulence and the transport rate. To support this hypothesis, the modification of existing models to emphasize sheared interface parameters will be considered.

CHAPTER 3

EXPERIMENTAL FACILITIES, INSTRUMENTATION AND PROCEDURE

The discussion of facilities and instrumentation will be divided into three main sections. The first section deals with the steam and water loop design. The second section discusses the major instrumentation including the steam side pitot tubes and conductivity probes, and the laser anemomenter system. The third section is an outline of the experimental procedure.

3.1. Channel Design

An optimum design for the test facility would assure reasonably two dimensional stratified flow of steam and water and permit continuous use with minimum maintenance. Therefore, a rectangular cross-section channel having a length of 1.60m, a width of .3048m, and a height of .0635m was fabricated out of welded 304L stainless steel plate (see Figs. 3.1 and 3.2). The nominal wall thickness is .64cm except for the flanges at the inlet and exit which are .95cm.

Visual access to the test section is provided by three rectangular Pyrex windows (10.2 x 6.25cm) on each side of the channel and five circular Pyrex windows (10.2cm diameter) in the floor of the channel. All (1.27cm thick) windows were mounted flush with the interior surface of the channel and sealed with silicone gaskets and sealant. The circular windows are located with centers at .157m, .306m, .586m, .868m, and 1.23m from the point of initial phase contact, which is used as the streamwide coordinate (x) reference. The rectangular windows were located at the first, third, and fourth circular window streamwise postions. No obvious flaws that would preclude laser anemometer operation were noted in the visual area of the glass. Five circular aluminum plates were used in place of the circular windows in the top of the channel. Thermocouples, static pressure holes, and traversable Prandtl tubes and conductivity probes were mounted in these plates. This instrumentation will be discussed in detail later. The top and sides of the channel were insulated with a 5cm layer of fiber glass.

The rectangular channel was one element in the system. There are separate loops for supplying the steam and water. The steam comes from the building supply which is nominally saturated and at a pressure of .83 MPa (120 psia). A steam separator and throttling valve assured dry, superheated steam at the entrance to the steam venturi manifold. Either a 3.18cm (1.25in.) or a 5.08cm (2in.) diameter venturi could be selected. Absolute pressure and temperature are monitored at the venturi. The manifold outlet was connected to the steam inlet plenum. Seven 50 x 50 mesh stainless steel screens in the inlet steam plenum insured uniform flow distribution. Water vapor that is not condensed in the facility passes to an outlet plenum and eventually to the atmosphere. The water, by contrast, flows in a closed loop which includes a 1700 liter (450 gallon) reservoir tank, inlet and outlet pumps, a plate type heat exchanger, and a 3.18cm (1.25in.) diameter venturi. Inlet and outlet temperatures were monitored with thermocouples. The heat exchanger allowed variation of the inlet water subcooling. The venturi calibrations were rigorously performed and are detailed by Lim (1981). The maximum flow rate for the water was approximately 2 kg/s and limited mainly by the outlet pump capacity. The maximum steam flow rate was .16 kg/s at the inlet. Normally the steam had about 40°C superheat and was assumed to be at one atmosphere pressure for the purposes of calculating the enthalpy.

3.2. Instrumentation

Two sets of complimentary instrumentation have been assembled for the facility. The first set is the group of probes and transducers that performs the steam side balance measurements. Included in this group are the Prandtl tubes, the static pressure taps, conductivity probes, thermocouples, venturis, and the corresponding pressure transducers. The second instrumentation set is used to investigate the liquid layer velocity. It consists of a laser doppler anemometer with associated mirror and lens platforms. Each set will be discussed presently.

3.2.1. Instrumentation for Steam Side-Mass and Momentum Balance Measurements

The principal instrumentation for measuring mass and momentum flux of the steam is a set of conductivity and pitot probes arranged at streamwise intervals and mounted on a vertically traversable table. A stepping motor drives the table, and two dial gauges give reference elevation and table tilt. The pitot probes are 3.18mm (.125in.) in diameter and are thermally insulated and electrically heated to minimize condensation within the pitot tube. The static and dynamic lines from each Pitot tube are connected to a Validyne DP-103 differential pressure transducer with a ± 345Pa (± 0.05 psid) range. The conductivity probes consist of pointed 3.18 mm (.125in.) diameter brass rods connected to a dc source. The O-ring fitting through which each rod passes is embedded in a Teflon plug in the upper channel wall and thus is electrically insulated from the facility. The probe is grounded only when the rod contacts the water. These probes are located at .157, .306, .586, .868, and 1.23 intervals from the point of initial phase contact. Wall static pressure measurements are made at .125, .275, .554, .837, and 1.2 meter intervals using the same differential pressure transducer bank. Several fixed and individually traversable stainless steel sheathed Cr-Al thermocouples of .254 and .508 mm (.01 and .02in) diameters are attached to the facility upper wall. Fixed thermocouples are installed in the steam venturi and water inlet and outlet plenums.

The accuracy of the mass flux measurements was established by completely condensing all the steam and water performing a first law energy balance. Comparisons of steam mass flux obtained by venturi, integration of the steam velocity profile obtained by the pitot probes, and the energy balance were in agreement within ± 3% . Steam air content was estimated by a Winkler test of the dissolved oxygen in samples of steam condensate to be less than or equal to 4ppm. A more complete discussion of this equipment can be found in Lim (1981).

A computer program was written which collects and reduces 16 channels of data, performing averaging and mass flux integration. Hardware used to accomplish this task is a PDP 11/34 computer with a 16 channel A/D converter, a CRT computer terminal located at the test site, and a 16 channel DC amplifier. The amplifier has 16 separate differential inputs with chopper stabilized integrated circuits. The gain of each channel can be varied from 1 to 1000 in discrete steps, allowing thermocouple measurements to be read directly by the computer. The computer program consists of a main program which manages and reduces the data and calls on subprograms to sample the 16 channels, linearize thermocouple, pitot tube and venturi readings, and calculate steam specific volume. Data sampling is performed at 240 readings per second over a 30 second interval. When the data scan is complete, the average velocity at each pitot tube, venturi mass fluxes and temperature are displayed. At that point, data can either be retaken or stored for that elevation. A new elevation is set and data are taken again. The data are automatically stored on a magnetic disk and optionally printed out on a Decwriter terminal at the conclusion of the experiment. The data on the magnetic disk can be plotted on a Tektronix graphics terminal and is available for further analysis.

3.2.2. Laser Anemometer and Associated Systems

A laser anemometer operating in the dual beam backscatter mode was used to measure the streamwise liquid velocity. All optical components for the LDA system are mounted on a rigid bench made of aluminum channel (5.08cm (2in.) x 12.7cm (5in.) cross section) and rigidly attached to the test section support frame. By doing so the relative motion between the test section and optics is minimized (see Fig. 3.3). The basic elements of the LDA system consist of an Argon laser, a beam splitter, a focusing lens, a backscatter receiving assembly, and a photomultiplier. The signal processor is a TSI model 1990 counter. These components will be discussed in more detail.

The integrated optical system consisting of the beam splitter, receiving optics and photomultiplier modules is mounted on a platform on the output side of the laser. The beam splitter produces two coherent beams with 50mm spacing and can be rotated to obtain orthogonal velocity components in a plane perpendicular to the optical axis.

The two parallel laser beams are directed to the focusing lens by the mirror modules A, B, and C as shown in Fig. 3.3. Mirror A is rigidly fixed to the frame. Then mirror modules B and C can be moved in the streamwise direction to any of several fixed locations corresponding to floor viewing windows. The Kelvin clamp type mountings at each of thse locations allows the modules to be removed and replaced with no change of displacement or orientation.

At module C, the fixed mirror was set at an angle of 50° with respect to the local horizontal so that the incident beams impinge on the window surface of the channel at an angle of 10° from the vertical. The focusing lens is attached to a traversing stage above the mirror so that the lens can travel vertically as much as 2.5cm in air. The focal point location in the liquid must be corrected for the index of refraction of the liquid (see Appendix A.1). A dial gauge was used to measure the vertical travel of the lens.

The measurement volume is approximately an ellipsoid in shape with major axis aligned with the optical axis and having approximate dimensions of .5 x .1mm, with the minimum dimension along the direction of flow. Operational procedures reduced the effective volume dimensions to .3 x .1mm. (See Appendix A.2 for details of the calculations to determine these dimensions.) Backscattered light from particles moving in the liquid layer is collected by the focusing lens. The 104mm focal length of the lens is not only suited to the dimensions of the optical layout but also maximizes (for the set of lenses supplied) the collection aperture and hence the scattered intensity. This is important because index of refraction gradients in the liquid may attenuate the light at a particular viewing angle. The scattered light passes back through the mirror system coaxially with respect to the input beams. To minimize the effect of stray light, the scattered light from the measurement volume is spatially filtered by a 0.28mm diameter pinhole in the receiving optics. Signal rate maximization requires careful alignment of the pinhole and photomultiplier.

Detailed discussion of the operational principles of the laser doppler anemometer are found in many references, among them Durst et al. (1976), Adrian (1980), and the Proceedings of the LDA-Symposium, at Copenhagen (1975). Consider Fig. 3.4 with input wave number vectors $\vec{k}_{li}$ and $\vec{k}_{ri}$ and scattered wave number vector $\vec{k}_{sc}$. The doppler frequency shift in the angular frequency ω of the light as it is scattered by particles in the flow, as shown by George (1975), is for the system

$$\omega_{Dl} = (\vec{k}_{li} - \vec{k}_{sc})\cdot\vec{u}$$
$$\omega_{Dr} = (\vec{k}_{ri} - \vec{k}_{sc})\cdot\vec{u}$$

where λ is the incident frequency. The photomultiplier is sensitive to intensity and therefore the square of the modulus of the net scattered electromagnetic field vector, $\vec{E}_{ls} + \vec{E}_{rs}$. Considering the contributions from both beams, the intensity I(t) is

$$I(t) \sim |\vec{E}_{ls}|^2 + |\vec{E}_{rs}|^2 + 2|\vec{E}_{ls}||\vec{E}_{rs}|\cos(\omega_{Dl} - \omega_{Dr})t$$

where t is time. The intensity thus has a time varying component with frequency f_D such that

$$f_D = \frac{(\omega_{Dl} - \omega_{Dr})}{2\pi} = \frac{2u}{\lambda} \sin \phi/2 \qquad (3.1)$$

which is the classical doppler frequency for a single particle.

The photomultiplier tube (PMT) senses both the mean and time varying intensity of the doppler signal. The PMT signal is amplified and processed by the counter. Stepwise variable high and low pass filters are provided to remove low and high frequency noise components of the signal and allow accurate measurement of the doppler frequency. A variable gain for the input is provided. When the amplified and filtered signal from a doppler event exceeds a 50mv threshold, a Schmitt trigger is activated.

For the "N cycle mode" of operation, the signal processor timer measures the time for a preselected number of filtered doppler signal zero crossings: that is, the times for N/2 and N zeroes of the doppler burst (where $N \equiv 2^n$ and n is a user selected integer value) are compared by a digital division. If the result is a factor of two to within stepwise selectable percentage tolerance, the signal is accepted. This criterion is to eliminate data from events caused by multiple particles in the measurement volume which may cause a loss of doppler signal zero crossings (Durst, et al. (1976)) through superposition of signals, resulting in an invalid estimate of the velocity.

The velocity data is available in either analog or digital form. The digital output consists of a twelve bit mantissa and a four bit exponent, proportional to the time for N zero crossings of the signal to occur. The processor has a 2 ns resolution. The timer can thus report particle velocities with a precision of better than one part in 1.34×10^8 . Additional digital outputs are available for computer-signal processor communication. By comparison, analog output for a fixed amplification is only resolved to one part in 1024 by the AR11 input board on the PDP 11/34. The signals are conveyed to the DR11C digital interface in the PDP 11/34 computer by a shielded cable. Line drivers and receivers located at the cable ends isolate the data lines and eliminate the occurrence of false signals caused by ground loops. Together with the facts that the signal processor is fundamentally a digital instrument and that high resolution is afforded by the digital format, the low susceptibility of digital signals to noise makes the use of the digital output preferable to the use of the analog output on the TSI anemometer.

Data from the DR11C and a programmable KW11P clock internal to the computer are stored in an array by an assembly language subprogram called by a Fortran data acquisition main program. Together with another assembly language subroutine which samples the analog data inputs, these programs collect and store velocity and run condition information on a floppy disk for analysis after the experiment.

The Fortran main program requests parameters such as: dial gauge readings of the channel floor, measurement volume intersecton point, number of doppler signal cycles, N, the steam venturi in use, the streamwise measurement location, the test number, and the date. Prior to each call to the LDA data acquisition subroutine, the dial gauge readings at the measurement point is requested. Then an assembly language subprogram samples and averages analog venturi and thermocouple data over a 8.5 second period at 240 samples per second.

When the LDA assembly language data acquisition routine is invoked, the anemometer data ready output line is repeatedly examined or polled by a loop in the program. When a data point has been accepted, the computer signals the processor to inhibit further data transmission until the doppler event velocity and the time between data points have been stored. Provision is made for a double word representation of the time between events within the computer memory. Although this procedure could allow the recording of time intervals between data up to 10^4 seconds, practical considerations required a loop which returns control back to the main program if after 20 seconds no new data are validated. A maximum of 6249 events may be stored in one call to this routine. This number is approximately the maximum permitted for the size of the available computer memory and is reduced if the time between data points requires the use of a double word representation. Since the velocity data is in a form not recognized by the computer, bit masking and shift operations isolate the mantissa and exponent information to allow the Fortran main program to compute event averaged velocity and turbulence intensity.

Up to nine 6249 event data records consisting of LDA output and the time between doppler events along with associated steam flow and temperature information can be stored on the floppy disk. Space is available also for the storage of the event averaged velocity and turbulence intensity as well as operational conditions of an additional 142 time sequences. As in the Pitot probe data acquisition case, reduced and unreduced data are displayed, and a flexible command structure allows rejection or storage of the data, a change of input specifications, or a program exit in response to printed options.

3.2.3. Data Analysis Programs

A family of data analysis programs have been written to perform statistical analyses of the time series data on the PDP 11/34. Two sets of programs make up this analysis package. Due to the size of the individual programs in the statistical package, each analysis task is handled by a series of separate codes which are automatically run in sequence within each set. Intermediate results are stored on the disk of the data from the corresponding input file.

Time averaged mean and rms velocity data as well as experimental conditions are obtained from the programs in the first program set. The data, which consists of randomly occurring doppler events, is sampled at equal time intervals and optionally stored on the disk to obtain a data sequence suitable for the fast Fourier transfrom (FFT) algorithm analysis. To implement this technique, samples are taken from linear interpolations between randomly spaced points. For sufficiently high data rates this approach should be reasonably representative of the time sequence. The number of samples per second can be set by the user or set equal to the average data rate for a given time series. The mean velocity and turbulent intensity are calculated from both this equal increment time series and from the original random data for comparison purposes.

McLaughlin and Tiederman (1973) discuss the nature of random data bias when using a counter type of anemometer signal processor to investigate turbulent flow. Basically the bias is due to the fact that for a turbulent flow with uniform seeding density, on the average a larger number of high velocity particles will be convected through the measurement volume than low velocity particles. Averages which are based on the sum of the event velocities divided by the number of the events (N_{ev})

$$\langle V \rangle = \sum_{i=1}^{N_{ev}} V_i / N_{ev}$$

should be larger than the true time average

$$\bar{V} = \frac{1}{T_{sd}} \sum_{i=1}^{N_{ev}} V_i \, \Delta t$$

where V_i are taken at equal time intervals Δt and T_{sd} is the period of the data record. The amount of this discrepancy varies with seeding particle distribution and any asymmetry in the intensity distributin within the measurement volume. For sufficiently high data rates, the equal increment sampling technique is adequate.

Histograms of the velocity and random time between events are also available. The velocity histogram was particularly useful in determining whether low frequency noise in the optical signal had been eliminated. Fluctuation velocity broadening due to the fact that the transverse velocity gradient was aligned along the major axis of the measurement volume is corrected for in a separate program (see Appendix A.3 for further details).

The second set of statistical analysis codes which contains the FFT algorithm is now considered. The FFT algorithm performs the transformation from time to frequency domain faster and with greater accuracy than direct transformation by the use of standard Fourier transform formulae. The reduction in computational time is roughly inversely proportional to the number of points. Improvements in accuracy are achieved by a reduction in the number of computations. The assembly language FFT code accepts two integer input arrays, representing the real and imaginary time series data, of up to 8192 elements each. Both forward and inverse transform functions are available. The equal time increment sampled data sequence is transformed using the FFT algorithm and then squared to yield the turbulence fluctuation power spectrum. The spectrum may be smoothed using a low side lobe leakage GEO window (Otnes and Enochson (1972)) for each of the spectral estimates and also by averaging neighboring estimates to yield constant bandwidth resolved spectra. Results are printed for logarithmically varying increments of the frequency while the entire spectrum is plotted on a Tektronix 4052 graphics terminal and associated hardcopy unit.

The value of the spectrum is normalized by $u'^2\Delta n$ where u' is the rms velocity (obtained by integrating the unscaled spectrum over the frequency range) and Δn is the fundamental frequency increment

$$\Delta n = 1/T_{sd}$$

Scaling in this manner yields a power spectrum function F(n) such that

$$\int_0^\infty F(n)dn \equiv 1 \qquad (3.2)$$

where n is frequency.

3.3. Experimental Procedure

The procedure for the operation of the laser anemometer will be discussed in detail following a short presentation of the procedure involving the steam side instrumentation. The reader is referred to Lim (1981) for a more detailed account of the Pitot tubes and conductivity probes.

3.3.1. Steam Side Instrumentation

The Pitot tube heating coils are turned on and a small amount of air is allowed to bleed through the pressure lines to preclude condensation during warmup. Then steam is permitted to flow through the facility to heat the walls and probes and to achieve stable operation of the steam venturi. The steam flows through a separator and is throttled ahead of the venturi to assure that only dry (superheated) steam flows through the venturi. Seal pots on the venturi pressure lines are bled to remove any air such that the vapor pressure will equal the pressure on the liquid surface. The differential pressure transducers for the steam and water venturis are zeroed with both sides of each transducer in pressure equilibrium. This procedure is also performed at the end of each run to check for any significant drift. The transducers are then connected to the high and low pressure ports of the venturis by means of valves to read the fluid pressure drop. The water side heat exchanger is turned on before two phase operation is initiated. Also prior to starting the water flow, the purge air to the Pitot tubes is shut off, the Pitot tube transducers are zeroed, and then the probe outputs are examined for stability. The computer data acquisition system is activated at this time as well.

When the water flow has been started, the water layer thickness and the steam velocity profile are measured. The traversing table is adjusted to place each conductivity probe at the water surface at the five measurement locations. Dial gauge readings of the traverse table are keyed into the computer. Following this, the Pitot tubes are traversed across the vapor space in stepwise fashion. At each elevation, dial gauge readings are noted and typed in. At the end of the traverse, the steam and water flow rates are readjusted and the liquid layer thickness and Pitot measurements are repeated for the new test conditions. Pressure drop measurements are taken separately using upper wall static taps and transducers. Mass and momentum flux integrations are performed by a separate computer program. Results of the flux integrations are plotted as a function of streamwise distance and curves are faired through the data. This procedure has been found to yield the most satisfactory estimates for streamwise gradients. Heat transfer calculations and data correlations are performed on the Northwestern University CDC Cyber 170 system.

3.3.2. Laser Anemometer

The procedure for the laser anemometer includes a single phase (water) alignment check prior to the two phase startup. The Argon laser is turned on and set to a low power with a beam attenuator in place. The mirror and lens modules B and C (Fig. 3.3) are installed at the desired streamwise location. A coarse adjustment is made on the receiving optics so that the measurement volume image is focused at the PMT pinhole.

After starting the water flow, the laser power is increased to .5w. The focusing lens is traversed upward so that the measurement volume is in the liquid flow. Fine adjustments are made in the mirror and PMT aperture positions to maximize the doppler event rate. The number of doppler cycles, N, is set at 32 and the tolerance for the factor of 2 digital division is 3%. These choices were found to reject low frequency noise likely due to interface reflections while maintaining a high data rate. The amplified and filtered output is displayed on an oscilloscope to allow for qualitative verification of the characteristic doppler signal and sufficient signal level to activate the Schmitt trigger. Silicon carbide particles are added to the water reservoir if the seeding level is insufficient.

The steam is turned on and zeroing of the water and steam venturis is performed as for the pitot tube traverse tests. Conductivity probe measurements of the interface location are recorded. Due to thermal expansion of the facility and pipes, the floor of the channel is displaced upward. Therefore the dial gauge reading at which the measurement volume is at the floor must be taken when the system is in operation and in thermal equilibrium. Then the liquid layer is traversed in stepwise fashion. Usually ten to twenty measurement locations are selected with several points repeated to verify the consistancy of the data. The interface is taken to be the elevation at which the doppler event rate falls to approximately 50% of its near surface value. At the close of the traverse, steam and water rates are readjusted and a new traverse is initiated.

CHAPTER 4

THEORETICAL CONSIDERATIONS

The specific forms of correlations for the transport process across a sheared gas-liquid interface will now be considered. Three sections will deal with scalar transport and the fourth section will discuss the interface shear. In the first section vapor and liquid phase resistances are compared. In the second the scalar transport equation and the interface boundary condition is formulated. This development indicates a basis for comparison of condensing heat transfer data and gas absorption data in the case where a single driving force controls the transport. A generalized transport coefficient will be defined for this type of problem. The next section is devoted to an examination of Lamont's eddy cell relationships with wall or inner scales substituted for the characteristic length and velocity. The resultant generalized transport coefficient predicted by the model is proportional to u_* . The fourth section discusses a hypothesis about the form of a general correlation for the interface shear stress in cocurrent flow.

4.1. Comparison of Gas and Liquid Phase Resistances

As a preliminary to the formulation of the liquid side diffusion equation, the reasonableness of considering only the liquid side resistance for condensation heat transfer will be shown. Since the gas and liquid resistances act in series, the controlling phase has the smallest thermal conductance. Kinetic theory results will be used to estimate the heat transfer coefficient for the case with no liquid resistance. This estimate will be compared with previous data from the Northwestern

University cocurrent steam and water loop. For gas absorption, if the gas solubility is low such as is the case for O_2, N_2, and CO_2 which are gases involved in the absorption studies considered, the interface concentration is in equilibrium with the gas phase and no diffusion layer or significant gas side resistance exists.

Shankar and Marble (1971) have developed a model from kinetic theory for transient condensation on or evaporation from a nonadiabatic plate. As the time of exposure becomes infinite the limiting rate is

$$G = .287\, \rho_g\, a_g\, \frac{\Delta p}{p_g} \tag{4.1}$$

where G is the mass flux; ρ_g, a_g, and p_g are the vapor density, isentropic sound speed, and pressure, respectively; and Δp is the difference between the saturation vapor pressure corresponding to the surface temperature and p_g. For slight departures from equilibrium, G can be quite large due to the magnitude of a_g .

Butterworth and Hewitt (1977) suggest a similar form for the mass flux in kinetics limited condensation. Their result is

$$G = 1.33 \left[\frac{M}{2\pi R}\right]^{1/2} \left[\frac{p_g}{T_g^{1/2}} - \frac{p_L}{T_L^{1/2}}\right] \tag{4.2}$$

where M is the molecular weight, T_g and T_L are the absolute gas and surface temperatures, and p_L is the vapor pressure at $T = T_L$. Here T_L is used instead of the liquid saturation temperature because no thermal diffusion layer exists in the liquid layer for gas kinetics limited condensation. Also the accommodation coefficient is set equal to .8. Equations (4.1) and (4.2) were originally formulated for slight departures from thermal equilibrium between the phases so that results obtained for a large temperature difference are considered qualitative.

A definition for the heat transfer coefficient h which is consistent with Davidson's (1978) and Lee's (1979) works is

$$h \equiv GH_g/(T_S - T_L)$$

where H_g is the steam enthalpy, T_S is the saturation temperature at one atmosphere, and T_L is the bulk liquid temperature. Here we note that H_2O enthalpies in this work are referred to the $0^\circ C$ datum. For

$$T_S = 100^\circ C$$

$$T_L = 20^\circ C$$

and

$$T_g = 140^\circ C$$

which are representative of inlet conditions in the present data set, Eq. (4.1) and the definition for h yields

$$h = 2.6 \times 10^3 \text{ kw/m}^2 \,{}^\circ C$$

while (4.2) yields

$$h = 4.1 \times 10^3 \text{ kw/m}^2 \,{}^\circ C$$

If measured condensation rates were to approach this value, the liquid side would have negligible resistance such that the condensation process would be gas phase limited. Davidson and Lee each report typical values for h of order 10 $\text{kw/m}^2 \,{}^\circ C$. This is much lower than the kinetic theory result and hence the principal heat transfer resistance is on the liquid side. The case where noncondensables are present in the gas phase such that the limiting resistance is on the vapor side is considered by Lim (1981).

4.2. Formulation of a Scalar Diffusion Equation

Consider an element of fluid with some conserved scalar property θ in two dimensional turbulent flow. The quantity θ may be enthalpy or the concentration of an absorbed specie. In the case of enthalpy transport, viscous heating of the fluid is neglected. This formulation also does not consider mass generation or chemical reactions.

The conditions for which the same equation applies to both simple mass transfer and combined heat and mass transfer will be discussed. A similar form for the equation is desirable because the gas absorption problem, which corresponds to simple mass transfer, and the condensation problem, which is combined heat and mass transport, may then be governed by the same mechanism. To simplify the problem, only flows with nonzero momentum transport at the interface will be considered. This restriction does not exclude the condensing stratified system of the present work and other experiments of interest. In such a case, corresponding transport coefficients may share similar data correlations and predictive models.

Kays and Crawford (1980) show several cases for which the diffusion flux terms for the combined heat and mass transfer case are identical to those of the simple mass transfer problem. The cases of interest, subject to the condition of no chemical reaction, are twofold:

1) Lewis number $\equiv \mathrm{Pr}/\mathrm{Sc}_j = 1$ for all components where Sc_j is the Schmidt number of the jth component.
2) Equal specific heats for all components.

The case with uniform composition is a special form of the second category and corresponds to the situation in condensing flows.

Considering Fick's Law diffusion only, the two dimensional transport equation is (Kays and Crawford (1980))

$$\frac{\partial\theta}{\partial t} + u\,\frac{\partial\theta}{\partial x} + v\,\frac{\partial\theta}{\partial y} = \frac{\partial}{\partial y}\left(\gamma\,\frac{\partial\theta}{\partial y}\right) + \frac{\partial}{\partial x}\left(\gamma\,\frac{\partial\theta}{\partial x}\right) \tag{4.3}$$

where γ is either a mass or thermal diffusivity, u and v are streamwise and transverse velocities, t is time, and x and y are streamwise and transverse coordinates. Defining mean and fluctuating components, time averaging and neglecting streamwise gradients in the laminar diffusion and turbulent flux terms yields the result

$$\bar{u}\,\frac{\partial\bar{\theta}}{\partial x} + \bar{v}\,\frac{\partial\bar{\theta}}{\partial y} = -\,\frac{\partial}{\partial y}\left(\overline{v'\theta'}\right) + \frac{\partial}{\partial y}\left(\gamma\,\frac{\partial\bar{\theta}}{\partial y}\right) \tag{4.4}$$

which is the boundary layer form of the transport equation. Here the over bar means a time averaged quantity and the prime means a fluctuating quantity.

A nondimensionalized form of (4.4) is desirable. In the case of turbulent shear flows, the shear velocity characterizes the logarithmic velocity profile and the value of the rms fluctuation velocity (Hinze (1975), Tennekes and Lumley (1972)). For asymmetric channel flow, Hanjalic and Launder (1972) find that u' near the rough wall is of order $2u_*$ where u_* is the rough wall shear velocity. Hadj-Fredj (1978) shows cocurrent flow data where the fluctuation at the base of the waves in the liquid is of the order of $2u_*$ to $4u_*$. Hence the interface shear velocity is a reasonable choice for the turbulence velocity scale. The difference between the interface and bulk values of $\bar{\theta}$ is a characteristic value of the transported scalar $\Delta\theta$ such that

$$\Delta\theta = \bar{\theta}_S - \bar{\theta}_L$$

where $\bar{\theta}_S$ is the surface value and $\bar{\theta}_L$ is the bulk value.

A suitable length scale is now hypothesized. If the resistance is primarily in the region of the interface, the characteristic length, may be reasonably estimated by what Hinze (1975) refers to as an inner or wall scaling, ν/u_*. It is noted that the characteristic length ν/u_* is for turbulent shear flow near a solid boundary. Although the liquid interface is not bounded by a solid wall, the fact that a wind generated shear force exists at the surface for all the data considered suggests the use of ν/u_* to scale near-interface regions. As noted in (2.7) Hughmark uses a length scale proportional to ν/u_{*f} as a characteristic turbulence burst length. Ueda et al. (1977) used a similar length scale in Eq. (2.26) although for the channel flows they considered, the shear occurs at the floor while transport occurs across the unsheared free surface. Nonetheless, the length scale is inversely proportional to the characteristic shear velocity of the flow. The appropriateness of this hypothesis versus the choice of a more conventional length scale such as the film thickness or interfacial roughness must be shown from an examination of the data.

With these assumptions, the dimensionless variables are

$$\begin{aligned} y_+ &= \frac{yu_*}{\nu} & \overline{v'\theta'}\Big|_+ &= \frac{\overline{v'\theta'}}{u_*\Delta\theta} \\ x_+ &= \frac{xu_*}{\nu} & \theta_+ &= \frac{\bar{\theta}}{\Delta\theta} \\ u_+ &= \frac{\bar{u}}{u_*} & v_+ &= \frac{\bar{v}}{u_*} \end{aligned} \tag{4.5}$$

So that for constant γ, Eq. (4.4) becomes

$$u_+ \frac{\partial\theta}{\partial x_+} + v_+ \frac{\partial\theta_+}{\partial y_+} = -\frac{\partial\overline{v'\theta'}\big|_+}{\partial y_+} + \frac{\gamma}{\nu}\frac{\partial^2\theta_+}{\partial y_+^2} \tag{4.6}$$

The solution for θ_+ is then of the form

$$\theta_+ = \theta_+\left(u_+,\ v_+,\ x_+,\ y_+,\ \frac{\gamma}{\nu},\ \overline{v'\theta'}\big|_+\right)$$

so that for similar mean flow and turbulence (i.e., similar u_+, v_+ and $\overline{v'\theta'}|_+$) the result is a function of dimensionless coordinates and γ/ν , the diffusivity ratio.

To find the flux of θ_+ across the interface, the boundary conditions must also be considered. However, the boundary condition of a sheared interface is quite complex. Random phase intermittency adds additional turbulent convective flux and laminar gradient terms over those that would be present in a turbulent flow with a fixed phase boundary. It might be hoped that an idealization of the interface as a flat surface could permit a tractable representation of the interface boundary conditions. For waves of large wavelength to amplitude ratio this is not unreasonable. With this assumption the nature of the transport is examined for a one-dimensional scalar flux at the boundary of a two phase system having a single driving force. Following Spalding (1963), Kays and Crawford (1980) identify two characteristic regions in the neighborhood of the boundary called the S and T states, as shown in Fig. 4.1. A third state which will be called the L state is also shown. Note that the location of this L state differs from that used by Kays and Crawford.

The T state is a region of zero scalar gradients far from the interface in the bulk neighboring (gas) phase. The S state is immediately adjacent to the interface in the considered (liquid) phase. The L state is within the bulk of the considered phase. Fluxes Q_T, Q_S, and Q_{SD} of the property $\bar{\theta}$ are also shown. Q_T and Q_S are mean convective fluxes of $\bar{\theta}$ at T and 0 while Q_{SD} is a diffusive flux at S and represents both laminar and turbulent diffusion. The states T and S are assumed close enough to the boundary so that the total flux is constant

$$Q_T = Q_S + Q_{SD} \tag{4.7}$$

Note that since no gradients exist at T, the transport of $\bar{\theta}$ is wholly convective in nature in the gas phase. The mass flux G is also constant so that

$$Q_T \equiv G\bar{\theta}_T \tag{4.8}$$

$$Q_S \equiv G\bar{\theta}_S \tag{4.9}$$

The Q and G fluxes are positive in the indicated directions.

A generalized transport coefficient will now be sought in the form of a Spalding conductance. The conductance g_{sp} (Spalding (1963)) is given by

$$g_{sp} \equiv G\left[\frac{\bar{\theta}_T - \bar{\theta}_S}{\bar{\theta}_S - \bar{\theta}_L}\right] = \frac{Q_{SD}}{\bar{\theta}_S - \bar{\theta}_L} \tag{4.10}$$

and hence it is seen that the conductance is directly proportional to the diffusive flux.

For condensation, $\bar{\theta}$ is enthalpy. The conductance defined in terms of the heat transfer coefficient is (Spalding (1963))

$$g_{sp} \equiv \frac{h_{sp}}{c_p} \tag{4.11}$$

where h_{sp} is the Spalding heat transfer coefficient. Hence for this case

$$g_{sp} = \frac{G}{c_p} H_g\left[\frac{1 - c_p T_S/H_g}{T_S - T_L}\right] \tag{4.12}$$

where enthalpies are with reference to the $0^\circ C$ datum, T_S is the saturation temperature, and T_L is the time average bulk liquid (fully mixed) temperature.

In mass transfer $\bar{\theta}$ is the time average mass fraction Y. The conductance is given by

$$g_{sp} \equiv G\left[\frac{Y_T - Y_S}{Y_S - Y_L}\right]$$

In the case of a slightly soluble gas such that $Y_S/Y_T \ll 1$

$$g_{sp} \simeq G\left[\frac{Y_T}{Y_S - Y_L}\right]$$

Since with the density ρ_S at S the mass flux is

$$\rho_S k_L (Y_S - Y_L) = G\ Y_T$$

it is clear that

$$k_L = g_{sp}/\rho_S \tag{4.13}$$

To facilitate representation of the results, a generalized transport coefficient is defined

$$K \equiv g_{sp}/\rho_S = \frac{G}{\rho_S}\left[\frac{\bar{\theta}_T - \bar{\theta}_S}{\bar{\theta}_S - \bar{\theta}_L}\right] \tag{4.14}$$

so that for mass transfer from (4.13)

$$K = k_L \tag{4.15}$$

and the diffusivity ratio is the Schmidt number. For heat transfer from (4.11)

$$K = h_{sp}/\rho_S c_p \tag{4.16}$$

and the diffusivity ratio is the Prandtl number. Davies (1972) uses the notation k_H for a group similar to that of (4.16). Overall, the flux of $\bar{\theta}$ based on (4.8) and (4.14) is

$$Q_T = G\bar{\theta}_T = \rho_S K\ \bar{\theta}_T\left[\frac{\bar{\theta}_L - \bar{\theta}_S}{\bar{\theta}_S - \bar{\theta}_T}\right] \tag{4.17}$$

Integrating the right hand side of Eq. (4.4) and evaluating yields the diffusional contribution to the flux, Q_{SD}. The total flux at the interface based on Eq. (4.7) is

$$Q_T = Q_S + Q_{SD} = G\bar{\theta}_S + \rho_S \overline{v'\theta'}\Big|_S - \rho_S \gamma \frac{\partial \bar{\theta}}{\partial y}\Big|_S \tag{4.18}$$

where the subscripts mean evaluation at state S conditions. Using the relationship between K and G from (4.14) and equating (4.17) and (4.18) yields

$$K = [\overline{v'\theta'}|_S - \gamma \frac{\partial\bar{\theta}}{\partial y}|_S]/\Delta\theta \tag{4.19}$$

Applying the nondimensionalizations of (4.5) to (4.19) yields

$$K/u_* = \overline{v'\theta'}|_{+S} - [\frac{\nu}{\gamma}]^{-1} \frac{\partial\theta_+}{\partial y_+}|_{+S} \tag{4.20}$$

where the subscripts +S mean nondimensionalized quantities evaluated at the interface. As is reasonable, K is scaled by the characteristic velocity u_* . Depending on the magnitudes of the Reynolds and diffusive fluxes, the diffusivity ratio ν/γ may characterize the transport coefficient.

The Reynolds flux term represents intermittent convection and is independent of the molecular diffusivity. If the Reynolds flux dominates the transport, ν/γ should not be a significant parameter, as suggested by Kishinevsky and Serebryansky (1956) for the case of gas absorption by a vigorously stirred liquid. Even if the Reynolds flux vanishes at the interface, the eddy diffusivity in the neighborhood of the surface can influence the functional relationship between K and ν/γ , as shown for example by King (1966) among others. The transport coefficient may then also be a function of the streamwise Reynolds numbers $x_+(= u_*x/\nu)$ and $u_+x_+(= U_Lx/\nu)$ such that in general

$$K \sim u_*\Gamma(\frac{\nu}{\gamma}, \frac{u_*x}{\nu}, \frac{U_Lx}{\nu}) \tag{4.21}$$

where Γ is a function to be determined. Although the significance of x_+ and u_+x_+ are difficult to assess without a complete solution for K, it is reasonable to suppose that a boundary layer develops at the interface and the transport coefficient is a function of an appropriate Reynolds number until the flow is fully developed. This development may be difficult to closely model and the appropriate velocity scale u_* or U_L may well be apparent only from data plotted with $u_* x/\nu$ and $U_L x/\nu$ as independent variables.

In view of these considerations, if the solution to the equation satisfies both the single driving force heat and gas transfer problems as hypothesized, then all the scalar transport data can be reasonably plotted together to determine a correlation for K, the generalized transport coefficient. Furthermore, since it has been shown that Sc and Pr represent the generalized diffusivity ratio ν/γ with which K is to be correlated, the range of Pr and Sc define the range of ν/γ . For the data considered it is found that

$$O(1) \lesssim \frac{\nu}{\gamma} \lesssim O(10^3) \quad .$$

The lower bounds are heat transfer data where

$$Pr \equiv \frac{\nu}{\gamma}$$

and the upper bounds are mass transfer data where

$$Sc \equiv \frac{\nu}{\gamma}$$

Considering the indicated range of ν/γ , it should be possible to define the dependence of K on ν/γ , and hence hopefully begin to identify the transport mechanism for the sheared interface transport case. A more explicit representation of (4.21) is desirable to properly choose correlating variables. This topic is pursued in the following section.

4.3. Scalar Transport Models for the Interface

In an effort to obtain a more mechanistic understanding of the postulated relation between the transport coefficient K and u_* , several eddy cell and surface renewal models for turbulent film flow will be considered. The form of these models when inner length and velocity scales are substituted will be discussed. For simplicity the correlation will be considered in mass transfer variables, k_L and D .

Substituting inner scales for length (ν/u_*) and velocity (u_*) into Lamont's fundamental eddy models Eq. (2.11) and (2.12) yields for the free surface or shear free (zero velocity gradient) mass transfer coefficient

$$k_{LFS} \sim C_1 u_* \, Sc^{-1/2} \tag{4.22}$$

and for the solid wall or sheared (nonzero velocity gradient) mass transfer coefficient

$$k_{LS} \sim C_2 u_* \, Sc^{-2/3} \tag{4.23}$$

with order one constants C_1 and C_2. The implications of the terms "shear free" and "sheared" in the context of stratified flow with interfacial momentum transfer will be investigated after considering the relationship between k_L and the energy dissipation.

Laufer (1954) shows that the u_* and ν/u_* are the proper scales to nondimensionalize ε near a sheared surface such that

$$\varepsilon \sim u_*^4/\nu \tag{4.24}$$

Substituting Eq. (4.24), into Eqs. (4.22) and (4.23) yields the results of Lamont's eddy models integrated across the energy spectrum

$$k_{LFS} \sim Sc^{-1/2}(\varepsilon\nu)^{1/4}$$

and (2.13)

$$k_{LS} \sim Sc^{-2/3}(\varepsilon\nu)^{1/4}$$

Eqs. (2.13) are somewhat more general in that the energy dissipation can be estimated for a given flow irrespective of the mechanism of turbulent energy generation.

The difference between shear free and sheared interfaces is now considered. The following discussion assumes that the liquid flow near the interface is turbulent, irrespective of wave amplitude. Kays and Crawford (1980) point out that for rough surfaces, pressure drag on the roughness elements is responsible for momentum transport. Hanratty and Cohen (1968) indicate that pressure-velocity correlations at fluid interfaces do not vanish, unlike the case for solid walls, and hence enhance the interfacial transport of turbulent energy. Experimental velocity measurements of Chang, et. al. (1971) suggest profile separation on the lee side of the waves in the gas phase, also in support of the profile drag mechanism. When the source of dissipated energy is interfacial pressure drag or, in the case of open channel flow, floor shear, the velocity gradient at the interface might be much less (or even zero) compared to that required to produce the floor or interface shear stress by a viscous shear mechanism. For the simple laminar eddy cell models considered by Lamont, viscous shear was the only means of momentum transport at the interface. Hence the nonzero velocity gradient solution for k_{LS} was associated with a shear flow near a solid wall and the zero velocity gradient solution for k_{LFS} was associated with an unsheared free surface. However a more general interpretation of the eddy cell solution would associate the k_{LS} solution with flows having appreciable viscous drag immediately at the eddy cell boundary while the k_{LFS} solution should apply when the source of dissipated energy originates from pressure drag at the interface or shear stress at a remote boundary, like a channel floor.

Based on the previous discussion for the case of nonzero momentum transport of a gas-liquid interface, pressure drag should dominate over viscous drag if the wave amplitude is sufficiently large. Therefore Eq. (4.22) should apply. Between that case and the case of zero relative velocity between the gas and liquid streams, the interface will be relatively smooth and the viscous drag contribution at the interface is dominant. Thus Eq. (4.23) should be used. The range of validity of each model might be obtained from an examination of the shear stress data to determine where the form of the shear stress correlation changes as the relative velocity between the gas and liquid increases. As the shear decreases ε is no longer proportioal to u_*^4/ν and Eqs. (2.13) are likely more appropriate.

By way of comparison if inner scales are substituted into (4.19) Theofanous et al.'s (1976) models (2.14) and (2.15) and Fortescue and Pearson's (1967) model Eq. (2.10), the solution for k_{LFS} results. Also if the renewal rate s in Danckwerts's (1951) model Eq. (2.4) is expressed in inner scales by

$$s \sim u_*^2/\nu$$

his result also reduces to Eq. (4.22).

4.4. Theoretical Considerations Relating to Interfacial Shear

As a means of determining τ , the adiabatic interface shear, and hence b_f in Linehan's and Mickley's models for the shear with condensation, a correlation for τ based on wind sheared channel flow data will be sought. A successful correlation could help decide which of the models for estimation of the shear with high mass transfer rates is correct. Also together with a Linehan or Mickley type of relation, a wind shear correlation for noncondensing flows would allow formulation of engineering estimates for the generalized transport coefficient if

$$K \sim u_*$$

as suggested in Section 4.2 and if u_* is not known a priori. This estimating algorithm would be a function of bulk flow parameters such as the phase velocity difference and bulk temperatures and could then be of more practical use in an engineering design sense.

The shear velocity at the interface can be estimated accurately from a relation obtained specifically for a given facility and used with confidence, such as Street (1979) and Gayral (1979) have done. However such a procedure would not be useful for computer code predictions of transport rates. For such purposes, a more generally applicable if less accurate method would be to test correlations against noncondensing shear stress data from several cocurrent horizontal flow experiments. The latter procedure has been adopted in this study.

In addition to the interface shear laws discussed in the literature review, an additional hypothesis will be considered. Levich (1962), Chang, et. al. (1971), and Wu (1968) suggest that the wind shear is primarily due to profile drag. If this is true, then the shear stress τ might will be proportional to the product of a function of the wave amplitude and the dynamic pressure in the gas

$$\tau \sim \rho_g \left(U_g - U_L\right)^2 f_s\left(\delta_L'\right) \tag{4.25}$$

Here f_s is a dimensionless function of the amplitude δ_L'. Note that the average phase velocity difference has been used. A further hypothesis is that an effective wave amplitude can be represented by

$$\delta_{LE}' \sim \left(U_g - U_L\right)^2/g \tag{4.26}$$

where g is the gravitatonal acceleration. The data of Mattingly (1977), Eloubaidy (1969), Hidy and Plate (1966), and Wu (1968) all indicate that the amplitude increses with velocity and so (4.26) is not unreasonable. In the following development δ'_{LE} will be substituted for δ'_L.

For fully developed flows of the small contactor at Toulouse (Asia et. al. (1981)), Theofanous et. al.'s (1975) data and Cohen's (1964) data, transverse channel and liquid layer dimensions are also likely to influence the magnitude of the shear stress. In the three data sets mentioned the streamwise distance measured from the entrance to the fully developed condition has the range of

$$\frac{x}{\delta_c - \delta_L} \gtrsim 37 \quad \text{and} \quad \frac{x}{\delta_L} \gtrsim 90 \qquad (4.27)$$

Here δ_c is the channel height and $\delta_c - \delta_L$ is the net gas phase thickness. Values of these ratios for the other shear stress experiments are less. Specifically for

$$\frac{x}{\delta_c - \delta_L} \lesssim 25 \text{ , or } \frac{x}{\delta_L} \lesssim 90$$

either or both the gas and liquid flows are developing. By comparison, Nikuradse (Schlichting (1968)) finds that entrance lengths for turbulent single phase pipe flows are in the range

$$25 \lesssim \frac{x}{D_p} \lesssim 40$$

where D_p is the pipe diameter. Additional confirmation of the developing nature of the flows which do not satisfy (4.27) comes from the repeated observation that wave amplitudes continue to grow with fetch for those experiments.

Wallis's (1975) correlation for the interfacial shear coefficient for annular flows which is

$$c_f = .005\left(1 + 300\frac{\delta_L}{D_p}\right)$$

suggests that an appropriate form for δ'_{LE} for fully developed flows might be

$$\delta'_{LE} \sim \left(\frac{\delta_L}{\delta_c}\right) \frac{(U_g - U_L)^2}{g} \tag{4.28}$$

Noting that δ_L/δ_c is equal to the liquid fraction, (4.28) is seen to imply that as the liquid fraction increases and slug flow is approach , the effective wave amplitude increases.

Further support for (4.28) is given by Suzanne (1977) who found that the small contactor data and Theofanous's results could be correlated by

$$\frac{\tau}{\rho g\ \delta_L} = 1.5 \times 10^{-17} Re_g$$

such that τ is proportional to δ_L. It is noted that the transverse dimensions of the two facilities are reasonably similar so that the proper functional relationship between τ and δ_c could not be discovered by examination of these data alone. However, δ_c in Cohen's (1964) facility is about one quarter the channel height for the other two (fully developed) data sets. Hence, with Cohen's data included, the appropriateness of the liquid fraction term can be confirmed with more confidence.

A normalizing velocity is chosen to be the minimum wave speed as shown in Lamb (1945),

$$c_m = \sqrt{2}\left(g \frac{\sigma}{\rho}\right)^{1/4} \tag{4.29}$$

where σ is the surface tension. A normalized amplitude is then given by

$$\delta'_{LE}/(c_m^2/g) \sim \tilde{U}^2$$

for developing flows of Eq. (4.26) and

$$\delta'_{LE}/(c_m^2/g) \sim \tilde{U}^2(\delta_L/\delta_c)$$

for developed flows of (4.28). Here a characteristic velocity $\tilde{U}$ is given by

$$\tilde{U} \equiv (U_g - U_L)/c_m$$

A dimensionless interface shear stress is similarly defined

$$\tilde{\tau} \equiv \tau/\rho_g\ c_m^2$$

For simplicity f_s is taken equal to the normalized effective wave amplitudes. Thus for developing flows it is proposed that in dimensionless form

$$\hat{\tau} = d_1 \hat{U}^4 \tag{4.30}$$

while for fully developed flows

$$\hat{\tau} = d_2 (\delta_L / \delta_c) \hat{U}^4 \tag{4.31}$$

where d_1 and d_2 are constants. The constants d_1 and d_2 and the value of the exponent of $\hat{U}$ can be obtained from curve fits to the data. The dependence of $\hat{\tau}$ on $\hat{U}$ would be different if $\hat{U}$ is less than a critical velocity for the appearance of substantial waves. In this case a smooth wall relationship such that

$$\hat{\tau} \sim d_3 \hat{U}_g^2 \tag{4.32}$$

is more likely, where d_3 is a constant.

4.5. Summary

In this section the nature and specific form of the liquid resistance in single driving force scalar transport problems with interface shear have been examined and a generalized transport coefficient defined. For an inner or wall variable scaling, the transport coefficient is suggested to be proportional to the product of u_* and functions of the diffusivity ratio and flow Reynolds numbers, and a specific form based on Lamont's models is discussed. The data base considered in this work seems to be governed by the single driving force scalar diffusion equation that is developed. Hence the condensation and gas absorption transport coefficient data can be plotted together. The diffusivity ratio (ν/γ) range for this data base is large enough to clearly establish the functional relationship between K and ν/γ .

Additionally a specific form for the correlation of the interface shear with no condensation has been proposed. The shear stress is hypothesized to be proportional to the product of an effective amplitude and the dynamic pressure at high enough velocities. A further hypothesis for an effective amplitude as a function of the relative velocity yields a model in which the shear stress is proportional to the fourth power of the phase velocity difference. An additional factor of the liquid fraction (film thickness to channel height ratio) is suggested for fully developed flows.

Comparisons of these hypotheses with other models and the data are considered in the results section which follows.

CHAPTER 5

RESULTS AND DISCUSSION

In this chapter three aspects of the work will be considered: the fundamental LDA results will be compared with force balance data, published correlations and the newly hypothesized models of Chapter 4 will be compared to the shear stress and transport data, and finally an engineering estimate will be sought for K, the generalized transport coefficient. The validated models for the interface shear stress and interface transport each contribute to the formulation of the engineering estimate, which is intended to facilitate numerical prediction of either the heat transfer or gas absorption mass transfer rate in cocurrent stratified flow.

5.1. Review of Velocity and Shear Stress Data for the Present Experiment

The velocity and shear stress data will be discussed in two sections: the first dealing with the LDA results for water only flows and the second part relating the LDA data to gas phase force balance results for cocurrent steam and water operation. Special attention will be given to u_*, the liquid side interface shear velocity. Specific questions to be answered are whether the laser anemometer results are correct, whether the shear velocity results obtained by independent means are in agreement, and how the interface turbulent fluctuation level is related to the shear velocity.

5.1.1 LDA Data for Water Only Flows

Liquid velocity profiles without steam flowing taken at water mass flow rates of 1.3 and 1.8 kg/s are shown in Figs. 5.1 through 5.4. With the exception of a slight tendency for a jet-like flow near the floor at location 1, the velocity profiles appear to be typical of open channel flow (Nalluri and Novak (1973), Raichlen (1967)) which show a floor boundary layer and the absence of a significant gradient at the interface. Location 1, Figs. 5.1 and 5.2, show a distorted profile with a local maximum near the lower wall. The reason for this distortion may possible be a nonuniform distribution of the glass marbles which formed the liquid plenium packing. Prior to use of the packing, spanwise variation of the flow caused large (0(10-20%)) discrepancies between the integrated mass flow using the velocimeter data and the water venturi data. Following the installation of the packing, the data in all cases indicated discrepancies of 0(5%) or less, with an average of 2.4%. This agreement is of the order found in the water venturi calibration measurements and confirms the accuracy of the anemometer.

The streamwise fluctuation or u' profiles are relatively constant except near the floor, where as expected u' increases near the floor. Care should be taken in the interpretation of the absolute magnitude of u' in the floor shear layer since these results have not been corrected for velocity gradient broadening. At location 1, the data show a slight increase in the rms fluctuation near the interface. This may well be due to the fact that the water levels indicated in Figs. 5.1 and 5.2 that are specified by the desired flow rate, exceed the height of the water outlet duct (1.6cm) in the test facility. It is noted that for similar water flow rates with steam the liquid is accelerated, reducing the depth. When normalized by the local mean velocity, the interfacial rms fluctuation at location 1 varies from 7 to 17%, with most values below 15%. By contrast location 3 turbulence intensities near the interface ranged from 4 to 6%. The location 3 values compare favorably with data for developed open channel flows (no interface shear). Nalluri and Novak (1973) show $u'/\bar{U}$ data in the range of 2 to 4% for Re_h of $O(10^4$ to $10^5)$, Richardson and McQuivey (1968, 1969) in the range of 3 to 6% for Re_L of $O(10^4)$, and Raichlen (1967) in the range of 4 to 5% for $Re_h = O(10^5)$. Here Re_h and Re_L are defined as

$$Re_h \equiv U_L D_h/\nu \quad \text{and} \quad Re_L = U_L \delta_L/\nu$$

and where U_L is the mean velocity, D_h the hydraulic diameter and δ_L is the depth. By comparison, the Reynolds numbers Re_h of liquid only flows for the present experiment ranged from 7×10^3 to 2×10^4. Laufer's single phase rectangular channel centerline turbulent intensities were in the range 2.7 to 3.4% for Reynolds numbers of $O(10^4$ to $10^5)$, where the characteristic length is the channel half width and the maximum velocity is used. Hence for the present facility at a sufficient distance from the inlet, the mean and rms fluctuation velocities with no steam flowing are characteristic of fully developed free surface flows.

Considering the free surface flow turbulent energy spectra, Figs. 5.5 and 5.6 show turbulent energy spectra (solid lines) taken at the interface at location 1 for water mass flow rates of 1.1 and 1.8 kg/s, which correspond to Re_h of 1.2×10^4 and 1.9×10^4. Also shown are channel flow spectra taken by Richardson and McQuivey (1968), McQuivey and Richardson (1969), and Nalluri and Novak (1973) at various depths. The spectra show that the -5/3 slope associated with the inertial subrange (Hinze (1975)) is confined to the range between 10 and 60 Hz. This behavior seems to be characteristic of low Reynolds number flows. The agreement shown is considered reasonable and confirms the consistancy of the LDA turbulence measurements. If the present result had deviated from previous work, there would be reason to suspect that perhaps significant amounts of noise in the PMT signal perhaps from stray reflections was being validated by the anemometer. The lack of a peak at 60 Hz indicates the absence of electrical noise which was a problem when, prior to using the anemometer digital output, data was transmitted in analog format between the laboratory and computer. Since wind amplification of waves does not occur, no significant peaks are expected or seen in the spectra. The tendency for the measured spectra to depart from the published data for frequencies less than 1 Hz is likely due to limitations on the duration of the LDA data sample imposed by the PDP 11/34 computer.

5.1.2 Cocurrent Steam and Water Results

In this section the LDA and force balance data will be presented and compared. A summary of steam pitot traverse conditions is given in Fig. 5.7. The data are from Lim (1981). For comparison with the gas absorption and wind shear stress data listed in Table 2.1, the range of inlet conditions for the present experiment are

$$1.6 \times 10^4 < Re_g < 6.5 \times 10^4$$

and

$$6.6 \times 10^2 < Re_L < 6.8 \times 10^3$$

Also shown on Fig. 5.7 are five conditions at which LDA liquid velocity measurements were made. These conditions are given in Table 5.1 where the run numbers correspond to steam pitot traverse test numbers. The five conditions are from the portion of the overall test matrix for which data rates were sufficiently high to guarantee well defined turbulence quantitites. The inlet water and steam temperatures were 25°C and 140°C , ± 5°C, respectively.

The interface location appeared to be indicated most reliably by the elevation of the LDA measurement volume at which "loss of signal" would occur. The loss of signal point was taken to be the elevation at which a decrease in the doppler event rate on the order of one half (as compared with neighboring elevations) would occur. The conductivity probe film thickness measurements are sensitive to channel floor displacements which occur during steam and water operation since the floor reference is determined in an unheated, zero flow condition. Although a measured correction factor was applied to account vertical thermally induced distortion of the facility of up to .4 cm, this correction represented only an average. Hence conductivity probe measurements of liquid depths are comparatively less accurate than the LDA loss of signal criterion on a run by run basis. In the discussion of LDA results therefore, the symbol y_L indicates the distance below this loss of signal point at a given x value. It should be noted that the conductivity probe measurements are sufficiently accurate to calculate the steam mass and momentum fluxes since errors in the estimate of the thickness of the steam boundary layer make only a small contribution to the flux integrals.

Mean velocity profiles were found to correlate reasonably well with a logarithmic law. The fits were performed by a nonlinear least squares algorithm and the von Karman constant was assumed to be .4 to determine u_{*LDA} , the shear velocity based on the mean liquid velocity profile. Sample profiles and the calculated logarithmic law fits (indicated by the solid lines) obtained by the least squares technique are shown in Figs. 5.8a-c for steam run 294a. The i-j data numbering convention in the figure titles indicates that the data from the jth LDA test is stored on the number i flexible (floppy) disk. For these plots

$$u_+ \equiv u_L(x,y)/u_{*LDA}$$

which is the normalized mean liquid velocity and

$$y_+ \equiv y_L u_{*LDA}/\nu$$

as in Eqs. (4.5). Values of u_{*LDA} , the shear velocity obtained from the fit, were used to calculate y_+ and u_+ for the plots after the fit had been obtained. The logarithmic law seems to approximate the data between $y_+ = 40$ and $y_+ = 10^3$, although a few data of other runs exceed these limits. The range of y_+ for which the fits were successful appears reasonable in comparison with pipe flow experiments (Schlichting (1968)).

Table 5-2 shows the entire u_* data set including force balance and velocity profile fit results. The LDA run number corresponds to the numbering convention for the floppy disks on which the data runs were stored. Steam run numbers correspond to the inlet flow condition matrix identification numbers indicated in Fig. 5.7.

One flow condition, number 173 indicated in Table 5-2 did not yield a good logarithmic fit. This condition corresponded to steam pitot traverse test number 254 at x = .157 ($Re_L = 2.4 \times 10^3$ and $Re_g = 3 \times 10^4$). The data for this condition are shown in Fig. 5.9a. The interface was relatively smooth at this water flow rate and the flow is suspected to be transitional. Using the laminar shear relation to approximate u_{*LDA} , that is

$$u_{*LDA} = \sqrt{\nu \, \partial u_L / \partial y} \qquad (5.1)$$

u_{*LDA} was calculated for 173 in Table 5-2 on the basis of a least squares exponential function fit to the mean velocity profile. The fact that the agreement between u_{*LDA} using Eq. (5.1) is poor is likely due to the difficulty in accurately measuring the velocity particularly near the interface where a large gradient existed for this flow condition. Location 3 at pitot traverse test number 254 (Fig. 5.9b) is by contrast reasonably approximated by the logarithmic law. The surface wave amplitude and frequency had also increased at this condition so that the turbulence was clearly more developed.

The fact that the mean velocity profile is well characterized by the interface shear velocity across the liquid layer thickness suggest the dominance of the interface shear over the floor shear. For the case where the interface shear is larger than the floor shear, the flow should accelerate, causing the liquid film to decrease in thickness. The large value of the interface shear is due to condensation momentum transport, a point which will be more quantitatively discussed in the shear stress correlation section. By contrast, the air-water data of Hadj-Fredj (1978) for the liquid layer shows that the floor shear velocity and distance from the floor consistently scale the logarithmic velocity profiles in the lower half of the liquid layer. No fit to the near interface data, which deviated from the floor shear law, was shown. Jeffries et al. (1969) in another air-water experimental facility find that the solid wall shear velocity scales the profiles except in a region near the interface. When the interface shear and the distance from the interface is used, no clear logarithmic region is in evidence. It should be noted that the air-water data cited were measured at a minimum of 2m from the inlet whereas the present LDA measurements were made at a maximum of .59m from the inlet of the NU facility. Thus the liquid floor boundary layer has had a greater distance to develop in the facilities of Hadj-Fredj and Jeffries et al.

A parameter of considerable interest is the liquid rms turbulent fluctuation. Figures 5.10a through 5.10c show u'/u_* vs. y_L/δ_L for the same steam condition run 294a. Here y_L is the distance measured from the interface into the liquid and δ_L is the liquid film depth determined by the loss of signal criterion. The measured intensity increases as the interface is approached. Near the interface, the intensity is likely to be representative of wave induced fluctuations as well (Theofanous et al. (1976) and Akai et al. (1980)).

Away from the surface the influence of the waves is reduced and the turbulence intensity approaches a constant for each run. Initially the bulk turbulence might be quite independent of the interface, but with development of the floor and interface boundary layers, u' should be proportional to u_*. If the value of the average fluctuation at $y_L/\delta_L = .5$ from faired curves of u' vs. y_L is denoted by $u'_{.5}$, the average ratio of the bulk fluctuation to interface shear velocity is found to be

$$u'_{.5}/u_{*LDA} \sim 1.2 \tag{5.2}$$

As an estimate of the variance of u' with transverse location, u' at $y_L/\delta_L = .4$ and .6 were measured. On the average, $u'_{.4}$ and $u'_{.6}$ showed a ± 8.6% deviation from $u'_{.5}$. By comparison the values for u'_i/u_{*LDA} at the interface showed an average value of 2.9. This data is shown in Fig. 5.11. Lines connect data at various steam pitot and LDA run conditions which are nominally similar. The value 2.9 is reasonable and compares favorably with liquid side interface fluctuation measurements for the large and small Toulouse facilities (Hadj-Fredj (1978)) which showed a range of

$$2 \lesssim u_i'/u_* \lesssim 4$$

Hadj-Fredj showed that u_i'/u_* was also a function of the ratio of the interface and floor shear stresses. The value 2.9 is larger than the limiting interface value of u_g'/u_{*g} which is (Hadj-Fredj (1978), Hanjalic and Launder (1972)) approximately

$$u_g'/u_{*g} \sim 2$$

where u_g' is the gas phase interface fluctuation and u_{*g} is given by

$$u_{*g} = u_* \sqrt{\rho_g/\rho}$$

This variation is due to possible differences in the momentum transport mechanism in the liquid and gas phases. The differences could arise from the fact that at large enough amplitudes, separation and reattachment occurs in the gas phase while the corresponding flow in the liquid phase is likely well represented by potential flow gravity waves.

Energy spectra obtained for steam and water operation show an increase in the fluctuation normalized energy F(n) at higher frequencies over the single phase results. The energy spectra for elevations where the signal rate is sufficiently large to permit calculation of F(n) up to n = O(100) Hz (which is the approximate frequency range of the energy containing motions) are invariant with y_L . Figures 5.12a-c show typical energy spectra for location 3 at steam test numbers 254, 294a, and 297 for the conditions indicated in Table 5-1. Lines of slope -1 which are characteristic of low frequency portions of shear flow energy spectra are shown. The negative unity slope occurs at lower wave numbers than the dissipation range and is derived by Tchen (1953) from the turbulent energy balance for the case where strong interaction occurs between the mean and turbulent flow vorticity. Hinze (1975) shows data confirming Tchen's hypothesis. If vorticity is proportional to gradients in the mean and fluctuating velocities and noting that these gradients increase near the surface, it can be suspected that strong interaction between the mean and turbulent vorticity will occur for the wind or steam sheared liquid layer. Hence a negative unity slope is reasonable. The spectra shown here seem to follow this -1 slope in the neighborhood of $n = 10$ Hz. This region is followed by an increase in the slope for the higher frequency components which are more isotropic. A slope of -5/3 is also indicated and seems valid for frequencies in the region around 60 Hz.

No characteristic wave frequencies are clearly obvious. Theofanous et al. (1975) and Gayral (1979) (large contactor data) show spectra with pronounced peaks at frequencies between 5 and 10 Hz. Conversely Gayral's results indicate that the small contactor at Toulouse has no preferred wave frequenices. It is suspected that the coherence and amplitude of the waves increases with fetch. Hence shorter length facilities such as the NU experiment and the small Toulouse contactor would have energy spectra characteristic of single phase flows with no strong wave induced maxima. Additionally in the present experiment the free stream vapor velocity decreases by a factor of three to five over the facility length due to condensation. This is quite unlike constant gas mass flow air-water wave generation experiments. Also in the case of the NU condensation experiment, the doppler signal rate decreased as the interface was approached, due partly to the flux of particle-free condensate into the surface. This interfered with measurements of the spectrum in the two phase region by reducing the measurable fluctuation bandwidth.

5.1.3. Interface Shear Results

The laser anemometer results for the shear velocity support the values for u_{*FB}, the liquid side interface shear velocity, obtained by an independent force balance on the vapor phase. As discussed in the previous section, the shear velocity was obtained from a logarithmic fit to the mean liquid velocity profile data as measured by the laser velocimeter in the liquid phase. In the vapor, a force balance is made using pressure drop data, a streamwise momentum balance, and the assumption that wall losses are reasonably predicted by the Blasius correlation. The details of the balances are discussed in Appendix B. For the bulk of the data, the solid wall shear stress contribution is O(20%) or less and tending to average about 10% of the interface shear balance (Eq. (B.7)). Hence the calculation is not strongly dependent on the accuracy the solid wall frictional loss estimate. This is confirmed by the fact that the use of the standard turbulent boundary layer shear law (Schlichting (1968))

$$c_f = .0576 \left(U_g \, x/\nu_g\right)^{-.2}$$

at the solid upper wall for representative data sets changed the interface shear velocity by about 1% on the average.

Some additional comments are in order about the interfacial shear stress. An element of the stratified system is shown in Fig. B.2. Considering stratified flows with no condensation Shemdin (1972), Kondo (1975), and Street and Miller (1977) all assume shear continuity at the wavy interface. For a developing wave system, Wu (1968) suggests that a force balance should include the rate of change of momentum of the waves, which he relates to a streamwise surface wave potential energy gradient. Thus the net forces on the gas and liquid single phase regions would be unequal. However, Street and Miller observe that the effect is a relatively constant factor of 0(10 to 20%) so that the correction could be handled by a multiplicative constant. They further comment that for transport controlled by interfacial dynamics ,u_{*FB} as determined from the gas phase force balance might likely be more appropriate. For the present experiment it is observed that generally the waves diminish in amplitude with fetch as the average gas velocity decreases and the average liquid velocity increases. Segev et al. (1980) makes similar observations for countercurrent steam and water flow. The momentum loss to the waves is thus not likely to be an important factor and shear stress continuity is a reasonable assumption.

With combined momentum and mass transport, a flux of momentum between phases normal to the interface occurs and must be estimated in a force balance. As shown in Fig. B.2, the magnitude of the flux is GU_i where G is the condensing mass flux and U_i is the gas and liquid interface velocity, if no slip is assumed. In general U_i is not known since the LDA experiments cover only a subset of conditions of the total steam pitot traverse test matrix. An estimate of U_i has been made by noting that in the case of Couette flow, the maxium velocity is twice the average velocity:

$$U_i = 2U_L \tag{B.6}$$

Despite streamwise acceleration of the liquid phase, the Couette flow model for the liquid layer seems to be a reasonable approximation of the interface velocity. The Couette flow estimates average about 88% of the interface velocity as indicated by the laser anemometer data. The agreement improves with streamwise distance from

$$\left.\frac{2U_L}{U_{i_{LDA}}}\right|_{AVE} = .73$$

at location 1 ($x = .157$m) to

$$\left.\frac{2U_L}{U_{i_{LDA}}}\right|_{AVE} = .98$$

at location 3 ($x = .586$m). Furthermore, it will be seen below that the interfacial shear for the present data will be well approximated by the asymptotic suction layer result

$$\tau^* \sim G(U_g - U_i) \tag{5.3}$$

so that for

$$U_g >> U_i \sim 2U_L$$

the magnitude of the interface momentum convection term is much smaller than τ^* , the shear stress with condensation.

Comparison of the values for u_* for the five operating conditions at three streamwise locations showed an average absolute discrepancy of 15% between LDA and force balance results. Figure 5.13 shows u_{*LDA}/u_{*FB} vs. $U_L x/\nu$. Here u_{*FB} is the local force balance interface shear velocity. The data scatter up to ± 30% about unity and any systematic deviation suggesting a discontinuity of forces at the interface is less than the 30% error bars. Similar agreement between turbulent shear stress in the gas and liquid at the interface in air-water flows has been observed by Hadj-Fredj (1978) and Gayral (1979), although u_{*g} values obtained from logarithmic fits to gas phase velocity profiles do disagree with their turbulent shear stress results for conditions with large amplitude waves. This is understandable because large amplitude waves make the problem of defining the interface location more difficult. In turn, this uncertainty in the interface location affects the process of fitting a logarithmic law (which is a function of y_g) to the gas velocity data.

Figures 5.14a through 5.14f show plots of u_* vs. streamwise coordinate for the conditions considered. The force balance data and the laser anemometer profile derived data are shown by the circle and square symbols, respectively.

Slight run to run variations in the conditions could appreciably change u_* in regions where du_*/dx is large and may account for some of the discrepancies between the two techniques shown in these figures, especially for high flow rate conditions like 297. This is because the liquid and vapor velocity data could not be taken simultaneously due to the considerably greater amount of time needed to obtain the liquid velocity profile. Conversely, the low flow rate condition 254 presented difficulties in that the profile at the first streamwise location was not logarithmic. The estimate for u_* based on (5.1) shows a 40.5% discrepancy from the force balance, which is likely more accurate. Overall, however, the agreement between the two independent measurement techniques is quite good and supports the use of the force balance analysis to obtain u_* for the entire steam pitot test matrix. For simplicity, u_* will be used to represent u_{*FB} in the rest of this work.

5.2. Correlation of the Interfacial Shear

As was noted earlier, correlation of the interface shear with bulk flow varibles is desirable from the standpoint of developing predictive codes. In the case of low mass transfer rates, the shear at the interface is largely due to profile drag on the large amplitude waves (Wu (1968)). The effect of high mass transfer rates which occurs in the condensing flows considered is effectively that of a suction for the gas phase, thinning the boundary layer and increasing the shear stress.

This section will be divided then into two subsections. In the first subsection, several candidate correlations for the adiabatic shear stress will be tested against the data base of Chapter 2. In the second subsection, the best correlation for the adiabatic shear stress will be incorporated into a model for the shear stress with condensation and compared to the condensing shear stress data of Linehan and the present work. An accurate shear stress model is necessary to formulate the engineering estimate algorithm for the transport coefficient based on bulk flow parameters.

5.2.1. Air-Water Shear Stress Data Correlations

The correlations proposed by Wu (1968) and Hidy and Plate (1966) as well as Eqs. (4.27) and (4.28) were tested against a data base of 160 points obtained from the sources discussed in Chapter 2. Specifically the data sets are from the large and small facilities at Toulouse (Asia et al.

(1981)), Mattingly (1977), Theofanous et al. (1975), Cohen (1964), Hidy and Plate (1966), Plate et al. (1969), and Wu (1968). A key for the data is presented in Table 5-3. Wu's (1968) correlations for high and low gas velocities were considered first. The present data did not support

$$\frac{k_s g}{u_{*g}^2} = .377 \tag{2.40}$$

which was based on Charnock's (1955) recommendation for aerodynamically rough flow nor Wu's own hypothesis

$$\frac{\rho u_{*g}^2 \; k_s}{\sigma} = 5.4$$

for low flow velocities. Additionally, Wu's correlations require prior knowledge of the interface roughness which is in general unknown. For predictive code purposes, it would seem these two equations are not suitable.

Figure 5.15 is a plot of $\hat{\tau}$ vs. $\hat{U}$. A dimensionless form of Hidy and Plate's (1966) correlation, Eq. (2.38) is

$$\hat{\tau} = 1.54 \times 10^{-4} \, \hat{U}^3 \tag{5.4}$$

which is also shown in Fig. 5.15. It is seen that Eq. (5.4) does pass through the bulk of the data for $\hat{U} > 20$ ($U_g - U_L \sim 4.6$ m/s). Below this velocity a lower value of the exponent for $\hat{U}$ would seem to better represent the data. This is not surprising because the correlation was obtained for velocities in the range of 6 to 12 m/s. To determine the usefulness of (5.4) in predicting the shear velocity, Fig. 5.16 shows $u_*/u_*|_{5.4}$ vs. $\hat{U}$. Here u_* is the interface liquid shear velocity from the air-water data set noted at the beginning of this section (5.2.1) and $u_*|_{5.4}$ is the predicted value based on Eq. (5.4). Again below $\hat{U} = 20$, a different shear stress law seems to hold. Further comment on Fig. 5.16

will be deferred until after the proposed correlation of this work is examined.

In Chapter 4, the hypothesized form of the shear stress relation was

$$\tilde{\tau} = d_1 \tilde{U}^4 \qquad (4.30)$$

for developing flows and

$$\tilde{\tau} = d_2 \tilde{U}^4 (\delta_L / \delta_c) \qquad (4.31)$$

for fully developed conditions. It was noted that the data of the small Toulouse contactor (Asia, et al. (1981)), Cohen (1964), and Theofanous, et al. (1975) which were considered fully developed were characterized by the dimensionless inlet parameter ranges

$$\frac{x}{\delta_c - \delta_L} \geq 37 \quad \text{and} \quad \frac{x}{\delta_L} \geq 90 \qquad (4.27)$$

Hence these three data sets would be used to examine the validity of Eq. (4.31) while the rest of the noncondensing interface shear data could be used to test Eq. (4.30). These two relations were hypothesized for wavy surface shear stress prediction. Below a value $\tilde{U}_{crit}$ of the normalized velocity a shear stress correlation more representative of a smooth surface relation was suggested. For $\tilde{U} < \tilde{U}_{crit}$ it was proposed that

$$\tilde{\tau} \sim d_3 \tilde{U}^2 \qquad (4.32)$$

As part of the effort to evaluate (4.30) through (4.32) it is necessary to obtain values for d_1, d_2, and d_3 by fitting the model equations to the data.

Figure 5.17 shows

$$\tilde{\tau} = \simeq 5.0 \times 10^{-3} \tilde{U}^2 \text{ for } \tilde{U} \leq \tilde{U}_{crit} \simeq 17.6 \qquad (5.5)$$

Although (5.5) tends to confirm (4.32), more data would be desirable. The maximum value of $\tilde{U} = 17.6$,.which equals 4 m/s at 20°C for water, corresponds to Plate et al's. (1969) maximum reported critical velocity which is the velocity required to cause visible waves. This value of U_{crit} is also supported by earlier observations about a change in shear law for $\hat{U} \leq 20$ as suggested by Fig. 5.16. The significance of $\hat{U} = 17.6$ is discussed further in the examination of the $\hat{U} > 17.6$ data.

Figure 5.18 shows that for $\hat{U} \geq 17.6$ a good correlation is

$$\hat{\tau} = 7.3 \times 10^{-6}\, \hat{U}^{3.8} \left(\frac{18.4\, \delta_L}{\delta_c}\right)^{\mu} \tag{5.6a}$$

where

$$\mu = \begin{cases} 1 & \text{for } \dfrac{x}{\delta_c - \delta_L} \geq 37, \quad \dfrac{x}{\delta_L} \geq 90 \\ 0 & \text{otherwise} \end{cases} \tag{5.6b}$$

The liquid fraction multiplier (δ_L/δ_c) was applied only for the data of the Toulouse small contactor, Theofanous, and Cohen. These experiments were considered developed two phase flows for which the overall liquid fraction would likely scale the wave amplitude and shear stress, as discussed in Chapter 4. A trial and error process confirmed that the shear law changes at about $\hat{U} = 17.6$, reinforcing the critical velocity argument. This value for the critical velocity does not necessarily imply that at all flow conditions for $\hat{U} < 17.6$ the surface will be glassy smooth since the liquid layer is probably turbulent for most of the data considered. A more likely explanation is that surface wave amplitudes become substantial enough to cause a change in the dominant shear generation mechanism, perhaps from viscous to profile drag. The exponent of $\hat{U}$ is 3.8 and is quite close to the hypothesized value of 4. The slight discrepancy could imply that the shear stress is proportional to the dimensionless wave amplitude raised to the .9 power instead of unity. Considering the wide range of data examined including developing and fully developed, thick and thin film data, the correlation is remarkable.

wide range of data examined including developing and fully developed, thick and thin film data, the correlation is remarkable.

The critical numbers for the entrance length parameters $x/(\delta_c - \delta_L)$ and x/δ_L that are indicated are considered provisional because the data are concentrated at extreme ranges of these two parameters, leaving substantial gaps in between. Furthermore, a contiuous functional relationship between the two cases where $\dot{\mu}=0$ (undeveloped wavy flows) and $\mu=1$ (developed wavy flows) is physically more realistic. The gap problem makes determination of this fairing law difficult using the present data set.

A law for the shear stress can be synthesized from the previous relations. Thus for $\tilde{U} < 17.6$ Eq. (5.5) is recommended while for $\tilde{U} \geq 17.6$ Eq. (5.6) is used. Figure 5.19 shows u_*/u_{*c} where $u_*|_{c*}$ is the predicted value for the liquid shear velocity based on Eqs. (5.5) and (5.6). The result is considerably better than Fig. 5.16 which is based on Plate's relation. Hence in this work Eq. (5.5) and Eq.(5.6) will be used to calculate τ when data is not available. The increase in shear stress with condensation is discussed in the next section.

5.2.2. Condensation Shear Stress Data Correlation

To correlate the shear stress with mass transfer, two models that of Mickley et al. (1954) and Linehan (1968) will be considered. As noted in the literature review, Kays and Crawford (1980) recommend Mickley's relation

$$\tau^*/\tau = \frac{b_f}{e^{b_f} - 1} \qquad (2.33)$$

with $b_f = -G(U_g - U_i)/\tau$

for transpired boundaries. Here $(U_g - U_i)$ is substituted for U_g to indicate the relative average gas phase velocity with respect to the interface Linehan (1968) has found that a Carpenter and Colburn (1951) relation

$$\tau^*/\tau = 1 - b_f \tag{2.31}$$

works well for his data.

With the combined correlation of Eqs. (5.5) and (5.6), the range of b_f for the condensation data of Linehan and the present experiment is

$$-.1 \gtrsim b_f \gtrsim - 56$$

Linehan's data reside primarily at the low end of the range and average about -5. Most of the present data have b_f in the range of -5 to -20 with an average of about -13.

It is observed that the ratio of (2.33) to (2.31), which indicates the relative magitude of the shear stress with condensation obtained by the two correlations is

$$\tau^*|_{2.33}/\tau^*|_{2.31} = \frac{b_f}{(1 - b_f)(e^{b_f} - 1)} \tag{5.7}$$

For b_f equals to -1, the above relation yields a value of .79, indicating that in the range where the adiabatic shear and asymptotic sucton layer contributions are equal, Linehan's expression predicts a larger total shear stress. In the limit of large b_f , both equations yield the asymptotic suction layer result which is

$$\tau^* = G(U_g - U_i) \tag{5.3}$$

Hence the low b_f behavior is the distinguishing factor.

Considering first Linehan's recommended relation, Fig. 5.20 shows $u_*/u_*|_{c^*}$ where $u_*|_{c^*}$ is based on (2.31) with τ from (5.5) or (5.6) depending on $\tilde{U}$. A key for the data is shown in Table 5-4. It is clear that Linehan's u_* is somewhat underpredicted, although the majority of the data are within ± 30% error margins. Form the foregoing paragraph it is clear that Mickley's relation, Eq. (2.33) would be slightly less satisfactory for the predominantly low b_f data of Linehan, causing his points to rise further above the unity line in Fig. 5.20. Although Linehan's relation, Eq. (2.31), is indicated to be the better correlation of his own data it is as yet unclear whether the Linehan correlation is better in general. In the absence of other data, Linehan's Eq. (2.31) will be tentatively recommended.

5.3. Mass and Heat Transfer Results

Several of the correlations previously reviewed will be examined presently. Specific attention will be focused on forms of Theofanous's models Eqs. (2.14) and (2.15) and the modifications of Lamont's eddy cell models using inner variable scaling proposed in Chapter 4.

5.3.1. Comparisons with Published Scalar Transport Correlations

Data considered in this section include the small and large contactor data sets of Asia, et al. (1981) and data from Mattingly (1977), Eloubaidy (1969), Linehan (1968), and the Northwestern University horizontal facility. Table 5-4 identifies the symbols. Overall, these sources yielded 295 data points. Since the shear stress was not measured in Eloubaidy's experiment, u_* was calculated from (5.6) for this and all following tests of proposed correlations in this section. The bulk or fully mixed temperature T_L is used to define Pr. The heat transfer coefficient h_{sp}, defined in Eq. (B.3) in Appendix B resembles a Spalding conductance such that the condensate convected heat transport at the interface was subtracted out of the total heat flux to compute h_{sp}.

Indicated in Fig. 5.21 is a form of a Kolmogorov eddy transport model cited by Asia et al. (1981) and similar to that recommended by Theofanous. The relation is

$$k_L = .5\, u_* \left(\frac{u_* k_s}{\nu}\right)^{-.25} Sc^{-1/2} \tag{2.37}$$

for mass transfer and

$$h_{sp} = .5\, \rho\, c_p\, u_* \left(\frac{u_* k_s}{\nu}\right)^{-.25} Pr^{-1/2} \tag{5.8}$$

for heat transfer. No strong correlation between k_L and k_s is noted. Data from near the inlet of the present experiment generally indicate a lower value of $h_{sp} Pr^{1/2}/(\rho c_p\, u_*)$ than data taken further downstream. Davies and Lozano (1979) found Kolmogorov eddy frequencies too high to explain their data so that the lack of correlation with a model using Kolmogorov scales is not surprising. Asia et al's. recommendation

$$.1 < \frac{k_L Sc^{1/2}}{u_*} < .2 \tag{2.36}$$

is also shown but fails to represent much of the condensation data.

In Fig. 5.22 Theofanous's relations

$$Sh_t \text{ or } Nu_t = .7I(t_T) Re_t^{1/2}\, Pr^{1/2} \quad \text{for} \quad Re_t < 500 \tag{2.17a}$$

and

$$Sh_t \text{ or } Nu_t = .25\, Re_t^{3/4}\, Pr^{1/2} \quad \text{for} \quad Re_t > 500 \tag{2.17b}$$

are examined. Here for simplicity $I(t_T)$ is set to unity for characteristic times $t_T >> 1$. Also approximating Λ the macroscale by δ_L, the liquid layer thickness

$$Nu_t \equiv h_{sp} \delta_L / k \tag{5.9a}$$

$$Sh_t \equiv k_L \delta_L / D \tag{5.9b}$$

and

$$Re_t \equiv 3u_*\delta_L/\nu \qquad (5.9c)$$

are defined. The factor of three is used in the definition of Re_t to agree with the conclusion about the rms fluctuation at the interface for the present experiment, which from Fig. 5.11 is

$$u_i' \sim 3u_* \qquad (5.10)$$

Thus the critical value of the independent variable $u_*\delta_L/\nu$ defining the regions of validity of the small and large eddy models is

$$\frac{u_*\delta_L}{\nu} = \frac{1}{3}\, Re_t^* = 167$$

The majority of the data are at Reynolds numbers larger than this value and thus within the range of validity of the small eddy model.

The small eddy relation does pass through much of the data. However, it is seen that the slope of the correlation does not match the slope of the data, which indicates an exponent greater than 3/4 is required. Additionally, the scatter in the data for the $Nu_t/Pr^{1/2}$ vs. $u_*\delta_L/\nu$ plot is large. Hence it seems that like k_s , δ_L is not the characteristic length scale. This is reasonable since the phenomena considered should be primarily controlled by interface scales, as suggested by the strong influence that the inlet steam mass flow has on the condensation rate (Lim (1981)), rather than bulk liquid turbulence length scales of which δ_L should be characteristic.

Linehan's constant Stanton number model is shown in Fig. 5.23 in a plot of St vs. $U_L x/\nu$. The heat transfer data scatter around

$$St = \frac{h_{sp}}{\rho U_L c_p} = .0073 \qquad (2.34)$$

but the gas absorption data are not at all correlated, suggesting that (2.34) is not the proper mechanistic model. This is not surprising since the thin film flows of Linehan may not be fully turbulent.

Figure 5.24 shows that the data as a whole are better fit by taking the exponent of Pr and Sc to be 1/2, Danckwerts' (1951) recommended value. At values of $u_* x/\nu > 2 \times 10^4$ a reasonable fit for the data is

$$\frac{Sh_x}{Sc^{1/2}} \text{ or } \frac{Nu_x}{Pr^{1/2}} = .0405 \left(\frac{u_* x}{\nu}\right)^{1.1} \qquad (5.11)$$

Equation (5.11) is shown by the solid line. Shown for comparison is the dashed line representing Eq. (5.14) which is considered in the following discusion. The data are reasonably well correlated at large values of $u_* x/\nu$ but scatter for values less than 2×10^4.

5.3.2. Discussion of the Present Correlation

Figures 5.21, 5.22, and 5.24 indicate that u_* is the appropriate velocity to scale h_{sp} and k_L and that the Prandtl or Schmidt number exponent and streamwise distance have some influence. One might suspect that the bulk liquid phase resistance, which could be of importance for entrance regions should also be taken into account. Considering the fact that typical smooth solid wall scalar transport correlations such as (Krieth (1968))

$$Nu = .023 \left(\frac{U_\infty x}{\nu}\right)^{.8} Pr^{1/3}$$

indicate that the Prandtl or Schmidt number exponent should be 1/3 for the Nu or Sh relation, it would be reasonable to use this exponent for relatively smooth interface conditions. For the large range of diffusivity ratio (Pr or Sc) considered, correct specification is required to formulate a general correlation.

Five inlet conditions of the present condensation test matrix were observed to have a relatively smooth interface with little or no waves. For the mass transfer data a "critical velocity" condition at which small wavelets appear as observed by Plate et al. (1969) might be used. In their paper, the critical wind speed was given approximately as 3 to 4 m/s at 3.5 to 4.9m, fetches typical of much of the gas absorption data. Small waves might be expected on the surface of any turbulent liquid even for no gas flow. However, what is suggested here is that the waves are amplified by the wind shear such that above the critical velocity not only the momentum transfer but also the mass transfer mechanism changes. Taking the critical relative gas velocity for noncondensing flows to be $\tilde{U} = 17.6$, nine points of the 101 gas absorption data are affected. Several of these points were markedly below the rest of the data of Fig. 5.21 in which the exponent of 1/2 was used for Sc and Pr. Above the critical wind speed, an exponent of 1/2 would seem reasonable since the majority of the data are well correlated in Fig. 5.24 by that choice.

It should be noted that for the present heat transfer data, although the relative gas velocity $\tilde{U}$ may fall below the critical value as the vapor is condensed, waves generated upstream (where the relative gas velocity is higher) persist throughout the test facility. Conditions under which smooth interfaces occurred were observed and recorded.

Following this reasoning, it is proposed that the groups $h_{sp} Pr^{\beta} / \rho u_{*} c_{p}$ and $k_L Sc^{\alpha} / u_{*}$ be plotted vs. $U_L x/\nu$. The exponents α and β have the following values:

$$\alpha = \begin{cases} 2/3 & \text{for } \tilde{U} < 17.6 \\ 1/2 & \text{for } \tilde{U} \geq 17.6 \end{cases} \qquad (5.12)$$

$$\beta = \begin{cases} 2/3 & \text{for smooth interfaces} \\ 1/2 & \text{for wavy interfaces} \end{cases}$$

The streamwise liquid Reynolds number is used to attempt to introduce some measure of the development of the turbulence in the bulk liquid flow away from the interface. A gradual transition between a Reynolds number dependent behavior at low $U_L x/\nu$ to Reynolds number independence at high $U_L x/\nu$ and therefore fully turbulent conditions could be expected. Hence the groups $h_{sp} Pr^{\beta}/(\rho c_p u_*)$ and $k_L Sc^{\alpha}/u_*$ should be constant at large Reynolds numbers. Development of the interfacial transport mechanism could also account for an increase in the value of these groups.

Figure 5.25 shows $h_{sp} Pr^{\beta}/\rho c_p u_*$, and $k_L Sc^{\alpha}/u_*$ vs. $U_L x/\nu$. Two regions on either side of a streamwise Reynolds number of 1.8×10^5 are considered. The majority of the data of the first and second streamwise locations of the present condensation experiment fall in the lower Reynolds number range. Although $k_L Sc^{\alpha}/u_*$ and $h_{sp} Pr^{\beta}/\rho c_p u_*$ could realistically be expected to increase with $U_L x/\nu$ approaching a constant value at high Reynolds number, a simple relation that best describes this fitting curve for $U_L x/\nu$ less than 1.8×10^5 is

$$\frac{h_{sp} Pr^{\beta}}{\rho u_* c_p} = .1 \tag{5.13}$$

which is not a function of Reynolds number.

This result is surprising also because this region includes data from both smooth interface and the largest amplitude surface wave conditions. Perhaps the reason that this relation is a constant below a Reynolds number of 1.8×10^5 is that many factors vary near the inlet such that the net effect is a constant relation. In particular, there is a three to five-fold decrease in the steam velocity as the interface boundary layer develops in the liquid. Due to the large interfacial shear, the liquid depth decreases typically by a factor of one half and this may affect interfacial boundary layer development as well. For these reasons Eq. (5.13) must be viewed as being somewhat tentative since relatively few data points from the literature, primarily from Linehen's experiment, fall in this region. Gas absorption data at these lower Reynolds numbers having relatively constant free stream gas velocities and depths could settle the question of whether (5.13) is a general law or simply a specific correlation for condensing cocurrent flows.

The high Reynolds number range includes all of the gas absorption data and most of the heat transfer data. Here

$$\frac{h_{sp} Pr^{\beta}}{\rho u_{*} c_{p}} \quad \text{or} \quad \frac{k_{L} Sc^{\alpha}}{u_{*}} = .14 \qquad (5.14)$$

is a reasonable correlation. The solid line represents Eq. (5.14) in Fig. 5.25. Equation (5.14) is also shown in Fig. 5.24 and agrees reasonably well with the data there. It is noted that the left hand sides in Eq. (5.14) have the form of a modified Stanton number, based on the shear velocity, times a Pr or Sc factor. Linehan's data show the most scatter. This may be due partly to the fact that the majority of his data was for liquid films less than 1mm in depth and possibly not fully turbulent in nature.

Since a physical explanation is desired for these results, several models and correlations discussed in Chapter 2 will now be compared to the present results. The correlations and models that will be studied are from Carpenter and Colburn (1951), Daly and Harlow (1980), and Levich (1962) which have not yet been tested with the results. With appropriate substitutions the first two models imply that K is proportional to u_{*} , similar to the present correlation. By contrast, Levich's model will be shown to be inappropriate for the case of wind sheared wavy interfaces.

Equations (5.13) and (5.14) resemble Carpenter and Colburn's (1951) correlation for condensing flows in tubes with nonadiabatic walls which is

$$h = .045\ \rho c_p u_* \mathrm{Pr}^{-1/2} \tag{2.35}$$

In their experiment, a significant portion of the heat transfer resistance was in the wall viscous sublayer, and should thus represent a different mechanism than the present experiment which has adiabatic walls. Hence the significance of the resemblence of their result with (5.13) and (5.14) is unclear, except that the wall is also a sheared boundary.

If the heat transfer coefficient is

$$h_{sp} = G\left(\frac{H_g - c_p T_S}{T_S - T_L}\right) \tag{B.3}$$

then Daly and Harlow's model implies

$$h_{sp} = J_c \rho c_p \left[\frac{H_g - c_p T_S}{H_{fg}}\right] \frac{S_L}{d} q_L^{1/2} \tag{5.15}$$

where q_L is the liquid turbulence kinetic energy and the bulk temperature T_L is assumed equal to the temperature at the edge of the thermal boundary layer. If the square root of the turbulence energy is proportional to the streamwise rms fluctuation, that is if

$$q_L^{1/2} \sim u'$$

and if at the interface (based on Fig. (5.11)) u_i' the interface fluctuation is proportional to u_* then aside from a Pr factor, (5.15) like (5.13) and (5.14) shows $h_{sp} \sim u_*$. This fact likely accounts for the success of the Daly and Harlow model in predicting Lee's (1979) data.

Although Levich's model

$$k_L = \left(\frac{\rho (u')^3}{\sigma} D\right)^{1/2} \tag{2.19}$$

was not investigated explicitly, substituting u_* for the turbulence intensity into Eq. (2.19) yields

$$k_L \sim u_*^{3/2}$$

Thus far, the best fit in each case has tended to indicate

$$k_L \sim u_*$$

so that (2.19) is not a likely candidate correlation. As noted in Chapter 2, this result is not surprising since for the data sets considered

$$O(10) \lesssim We \lesssim O(10^2)$$

where the interface distortion Weber number is

$$We \equiv \frac{\rho_g U_g r_L}{\sigma} = \frac{\rho_g U_g^2}{\rho (u_i')^2}$$

Here u_i' is the rms liquid fluctuation velocity. For this range of Weber number the gas phase dynamic pressure is much larger than capillary forces. Hence Levich's model is inappropriate for wind sheared flows because the dynamic pressure is neglected in the force balance.

5.3.3. Comparison of the Modified Lamont Models to the Present Results

In Chapter 4, models for K were introduced, a generalized transport coefficient. These models which are based on a modification of Lamont's results predict many of the observed features of Fig. 5.25. Primary attention will be focused on the data for which $U_L x/\nu > 1.8 \times 10^5$ since lower Reynolds number data may reflect a complicated interaction of streamwise gradients in the vapor velocity and liquid depth with development of the liquid interfacial boundary layer in condensing flows. Additionally the liquid phase bulk resistance is likely minimized in the high Reynolds number range. Therefore the high Reynolds number conditions can reasonably be characterized by the interface resistance alone, as Thomas (1979) suggests. Lamont's models yield the functional form of this resistance as will be seen.

The modified eddy cell result for the interface with relatively negligible viscous shear (pressure drag dominated case) is, in terms of K and γ

$$K = C_1 u_* \, (\nu/\gamma)^{-1/2} \tag{4.22}$$

For the viscous sheared (nonzero velocity gradient) interface, the model is

$$K = C_2 u_* \, (\nu/\gamma)^{-2/3} \tag{4.23}$$

where γ is either D for gas absorption or $k/\rho c_p$ for heat transfer. Both (4.22) and (4.23) are based on an eddy cell model of the interface turbulence. The agreement with the observed proportionality between K and u_* in the correlation Eq. (5.14) is clear. Furthermore, the variation of the exponent of the diffusivity ratio matches the observed best fit values for α and β in Eq. (5.12), as discussed earlier. That is, if for rough surfaces the momentum transport is primarily by means of pressure rather than viscous drag, then relative to the total interfacial shear, the viscous shear and velocity gradient at the interface is relatively small. Such a case, for which the vanishing velocity gradient or shear free model Eq. (4.22) seems appropriate, matches the conditions in (5.12) at which α or β equals 1/2. In the case of the NU data, the condition of an observed smooth interface is used to select the value 2/3 for β. Otherwise β is set to 1/2. For Linehan's data the inlet velocities are of the O(10 m/s) and the flow is assumed wavy. Hence β is assigned the value 1/2. Similarly, the air-water data for which $\tilde{U} \geq 17.6$ uses a value of 1/2 for α . The air-water data for which the exponent 2/3 has been selected (most of which are from the Toulouse small contactor and are all at $U_L x/\nu > 1.8 \times 10^5$) represent only about 4% of the entire data set considered in this work. Clearly further experimental verification is in order. However a definite improvement in the data correlation is realized by the use of an exponent of 2/3 instead of 1/2 for that data.

In summary, for wavy surfaces Eq. (4.22) and for relatively smooth interfaces Eq. (4.23) with constants

$$C_1 = C_2 = .14 \quad \text{for} \quad U_L x/\nu > 1.8 \times 10^5$$

are considered to be the best model for the present data set. This statement is based on the agreement between the form of the correlation and the modified Lamont models. Further justification for the use of inner velocity and length scales will now be considered.

5.3.4. Experimental Estimates for Turbulent Velocity and Length Scales

Inner scales were substituted for the eddy velocity and length u_c and ℓ in Eq. (2.11) and (2.12) on the basis of an argument that u_* and ν/u_* characterize the inner region of a sheared boundary. If u_c is estimated by u'_i, it has already been seen from Fig. 5.11 that

$$u'_i \sim 3u_* \tag{5.10}$$

on the average for the LDA data set. Furthermore the u' and v' data obtained in the liquid layer by Hadj-Fredj (1978) for the two Toulouse facilities similarly supports (5.10).

The interface length scale was hypothesized to be of the form

$$\ell = \xi \, \nu/u_* \tag{5.16}$$

Photographic data taken of the interface in the present experiment confirm the presence of small scale three dimensional waves for Reynolds numbers $U_Lx/\nu > 1.8 \times 10^5$. Estimates of the wavelength at a streamwise station where a regular (more or less pebbled) pattern is in evidence show scatter but average to about

$$\frac{\lambda u_*}{\nu} \sim 130 \tag{5.17}$$

Here λ is a streamwise wavelength of the pattern in the range of U_Lx/ν where Eq. (5.14) is valid. This estimate is considered to be accurate to the order of magnitude and, although preliminary, encouragingly resembles Ueda el al.'s (1977) result for λ_+ in Eq. (2.26) and Hughmark's (1971) relation for x_B in Eq. (2.7).

The existence of small waves of wavelength $\lambda \sim \nu/u_*$ suggests the presence of near surface turbulent motions which are scaled by ℓ. It is therefore reasonable to suppose that

$$\xi \sim O(100)$$

although this should be confirmed by turbulence measurements. At low velocities between the gas and liquid, surface disturbances related to the effective turbulent motions may not be obvious. However the use of ν/u_* as a characteristic length scale is not unreasonable since even for that case as long as the liquid flow is turbulent the resistance should be at the interface and characterized by inner scales.

5.4. Engineering Estimates for K

From the standpoint of numerical analysis, the question occurs whether or not prediction of the heat or mass transfer at the free surface is possible in terms of bulk variables. This is significant because neither K nor u_* are known generally, even at the entrance or exit. It would be reasonable to attempt to formulate an engineering estimate for K which would be a function of the bulk variables. This could be accomplished by combining correlations obtained for u_* and h_{sp} and k_L and using appropriate approximations to simplify the final formula.

The procedure for the heat transfer data is to model the interface shear with condensation by the Linehan result Eq. (2.31). In turn, the condensing mass flux G is obtained from a first law balance relating the condensing heat flux G H_g to the heat transfer coefficient. Next, the heat transfer coefficient is related to u_* through the experimental correlations, Eqs. (5.13) and (5.14) with a step function change from one to the other at a Reynolds number $(U_L x/\nu)$ of 1.8×10^5 for simplicity. In this manner an estimate u_{*e} is obtained for u_* in terms of bulk flow variables. Substitution of the result for u_{*e} in (5.13) and (5.14) yields h_e as a function of bulk quantities. Since Linehan's model has the correct limit

$$\tau^* = \tau \tag{5.18}$$

when

$$G = 0 \tag{5.19}$$

the equation for u_{*e} in a condensing flow yields the correct estimate for u_* in the vanishing G case which is representative of gas absorption. Substitution of the estimated value for u_* into the mass transfer form of Eq. (5.14) yields then k_{Le} the estimated value for k_L in terms of bulk quantitites.

The specific relations are now discussed. For the heat transfer data the relation between the heat transfer coefficient and G (the condensation rate) from Appendix B is

$$G = h_{sp}\left(\frac{T_S - T_L}{H_g - c_p T_S}\right) \qquad (B.4)$$

where H_g is the gas enthalpy, T_S is the saturation temperature, and T_L is the bulk liquid temprature. The shear velocity is obtained from a solution of a quadratic equation based on Linehan's shear stress model (2.31), (B.4), and the transport correlations (5.13) and (5.14). This equation is

$$\begin{aligned} \rho u_{*e}^2 &= \tau + G(U_g - U_i) \\ &= \tau + \Omega \rho c_p \; u_{*e} Pr^{-\beta}\left[\frac{T_S - T_L}{H_g - c_p T_S}\right](U_g - U_i) \qquad (5.20) \end{aligned}$$

where Ω is .14 for $U_L x/\nu > 1.8 \times 10^5$ and .1 for $U_L x/\nu < 1.8 \times 10^5$, u_{*e} is estimated value for u_*, τ is the adiabatic shear given by (5.5) and (5.6), and β is given by (5.12). The term Ω equals the constants in (5.13) and (5.14). The gas velocity factor in the expression for b_f in (2.32) has been modified to become a net velocity such that

$$b_f = - G(U_g - U_i)/\tau$$

From Appendix B assuming Couette flow, the interface velocity is approximated by

$$U_i = 2U_L \qquad (B.6)$$

Hence u_{*e} is obtained from

$$u_{*e} = -b_*/2 + \sqrt{b_*^2/4 + \tau/\rho} \qquad (5.21)$$

where

$$b_* = - \Omega c_p Pr^{-\beta}\left[\frac{(T_S - T_L)}{H_g - c_p T_S}\right] (U_g - 2U_L) \qquad (5.22)$$

BEST DOCUMENT AVAILABLE

It is seen that for large values of b_f, (5.21) yields the asymptotic suction layer result while for vanishing G, (5.20) yields the value for the adiabatic shear stress directly.

The relation for the estimated heat transfer coefficient h_e is then based on (5.13) and (5.14) with an abrupt change in Ω at a Reynolds number of 1.8×10^5. The relation is thus

$$h_e = \Omega \rho c_p u_{*e} Pr^{-\beta} \qquad (5.23)$$

For the gas absorption case k_{Le} is given by

$$k_{Le} = \Omega u_{*e} Sc^{-\alpha} \qquad (5.24)$$

where now

$$u_{*e} = \sqrt{\tau/\rho} \qquad (5.25)$$

and α is from (5.12).

The adiabatic shear stress τ is modelled for $\tilde{U} \geq 17.6$ by

$$\tau = 7.3 \times 10^{-6}\, \tilde{U}^{3.8} \left(18.4 \frac{\delta_c}{\delta_L}\right)^{\mu} \qquad (5.6a)$$

with

$$\mu = \begin{cases} 1 & \text{for} \quad \dfrac{x}{\delta_c - \delta_L} \gtrsim 37 \;,\; \dfrac{x}{\delta_L} \gtrsim 90 \\ 0 & \text{otherwise} \end{cases} \qquad (5.6b)$$

Finally, for $\tilde{U} < 17.6$, τ is given by

$$\tau = 5.0 \times 10^{-3}\, \tilde{U}^2 \qquad (5.5)$$

With the foregoing relations a stepwise solution technique can be obtained. Starting from given inlet conditions which indicate initial values of parameters like T_L, U_g, U_L, δ_L and other related quantities, the local interfacial heat or mass transfer coefficient and the shear stress on small elements in the gas and liquid are calculated using (5.21) and (5.25) for u_{*e} and (5.23) or (5.24) for h_e or k_{Le}, respectively. In the gas phase the pressure gradient is assumed to be a function of x only. The pressure gradient can be calculated if the upper wall shear is estimated by an appropriate turbulent shear stress correlation. In this work the Blasius formula was a reasonable estimate of this contribution since the interface shear with condensation was so much greater than the smooth wall shear. This is also likely true of the floor shear contribution in the liquid layer so that the Blasius relation may tentatively be recommended to estimate the solid wall shear in the liquid layer. In the liquid phase, the hydrostatic pressure is also considered. From mass and force balances, the liquid depth and gas and liquid average velocities are calculated at the downstream surfaces of the gas and liquid, assuming that the heat transfer coefficient is constant over the streamwise length of the small element. For gas absorption the mass balance yields the bulk average liquid concentration at the downstream cell boundary. For condensation heat transfer, an energy balance yields the bulk average liquid temperature at that boundary. The process is repeated for the next cell in each of the gas and liquid phases based on the new values for U_g, U_L, T_L or Y_L, δ_L, and gas phase pressure. The entire flow field and the total condensate or dissolved gas flux can be computed at any location in this manner. Incorporated into a predictive code, the engineering estimate formulas could also be used as an initial guess in a solution technique having (5.13) and (5.14) as convergence criteria when iterating between coupled scalar transport and momentum equations.

As a technique for obtaining engineering estimates, the equations for h_e and k_{Le} would likely be useful for turbulent films thicker than that of Linehan's experiments since the thin films in his work may not be fully turbulent. Because these equations are based on a mechanistic correlation rather than a simple least squares fit of laboratory data, one can expect that they will be less sensitive to scale and hence more readily applied to industrial problems. Further refinement of this technique should be the result of a comprehensive numerical modeling study comparing data with calculations based on this and other works. The unresolved discrepancies are then the topics for further experimental research which have the highest potential value. By this sort of iteration between experiment and numerical analysis, investigators will more quickly converge on the most reliable method to estimate interfacial transport for sheared, cocurrent gas and liquid flows.

CHAPTER 6

CONCLUSION

This work has achieved the following goals with some measure of success:

1. Measurement of local heat, mass, and momentum transport and liquid phase turbulence for a cocurrent, condensing stratified steam and water flow;
2. Establishment of a correlations for noncondensing and condensing flows:

$$\tau^*/\tau = 1 - b_f \tag{2.31}$$

with

$$b_f = -G\left(U_g - U_i\right)$$

where for strongly sheared interfaces the Couette flow assumption yields

$$U_i = 2U_L \tag{B.6}$$

The correlation for τ for $\tilde{U} \geq 17.6$

$$\tilde{\tau} = 7.3 \times 10^{-6}\, \tilde{U}^{3.8}\left(18.4\ \delta_L/\delta_c\right)^{\mu} \tag{5.6a}$$

with

$$\mu = \begin{cases} 1 & \text{for} \quad \dfrac{x}{\delta_c - \delta_L} \geq 37\ ,\ \dfrac{x}{\delta_L} \geq 90 \\ 0 & \text{otherwise} \end{cases} \tag{5.6b}$$

For data where $\tilde{U} < 17.6$

$$\tilde{\tau} = 5 \times 10^{-3}\, \tilde{U}^2 \tag{5.5}$$

3. Establishment of a correlation between a scalar transport coefficients and the interface shear velocity from Eq. (5.13) and (5.14):

$$\frac{k_L\, Sc^{\alpha}}{u_*} \sim .14 \quad \text{for} \quad \frac{U_L x}{\nu} > 1.8 \times 10^5$$

and

$$\frac{h_{sp} Pr^{\beta}}{\rho c_p u_*} \sim .1 \quad \text{for} \quad \frac{U_L x}{\nu} < 1.8 \times 10^5$$

$$\sim .14 \quad \text{for} \quad \frac{U_L x}{\nu} \geq 1.8 \times 10^5$$

where α and β are given by (5.12).

4. Formulation of a mechanistic model (specifically substitution of inner scales into Lamont's eddy cell results) to explain important features of the correlation;
5. A reasonable engineering algorithm which is based on the data correlations such that the momentum and scalar transport are estimated on the basis of bulk flow parameters, facilitating application to flows where the shear velocity is not known a priori.

Useful extensions of this work can be recommended:

1. Verification of the basic data correlation with additional sheared interface data, particularly gas absorption data in the low $U_L x/\nu$ range;
2. More careful measurement of the turbulence length scales of the interface to establish the relation of those scales to the transport coefficient;
3. Verification and refinement of the engineering algorithm for the transport coefficient;
4. Refinement of the shear stress correlation with regard to fetch and entrance length influences;
5. Further efforts such as that of Daly and Harlow to numerically predict local variables in condensing stratified flows using the present, more accurate data set.

It is expected that new numerical analysis efforts will yield improved insight into the nature of the turbulent shear stress and scalar flux distribution through the liquid and the effects of variable gas phase velocity and liquid phase depth for condensing flows. This may help identify the reason for the more or less sudden change in the correlation at a streamwise Reynolds number of 1.8×10^5.

Indeed, it would seem that the fifth point may be the most necessary in order to optimize experimental planning. New experimental work should be oriented not only to address the other four points but also to answer new questions that will undoubtedly develop in the effort to numerically predict transport rates. In this manner it is hoped that the present work might facilitate the development of more reliable reactor component and system codes which is the ultimate goal.

APPENDIX A.1

CHARACTERISTICS OF A CONVERGING BEAM PAIR OBLIQUELY INCIDENT ON A MULTILAYER SYSTEM

In this section the effect, if any, on the convergence angle caused by the oblique incidence at the window of the beam pair axis of symmetry and the displacement of the measurement volume due to changes in index of refraction for a multilayer system are considered. The focusing lens for the present experiment was oriented such that the axis of symmetry of the two beam system made an angle of approximately 10° to the window surface unit normal. The axis of symmetry is defined to be the bisector of the angle formed by the converging beams.

Consider Figs. A.1 and A.2. For simplicity only one of the two input beams is represented. Two coordinate systems are discussed: the (x,y,z) system and the (x',y',z') system. The y and y' axes are oriented vertically downward. The x axis is in the streamwise dimension, the z axis is oriented spanwise, and the origin of the (x,y,z) system is at the center of the flow inlet. The x'-z' plane is at the lower glass surface. The projection of the $\vec{k}_1$, vector on the glass is the x' axis. Note that $\vec{k}_i$ is the incident beam propagation vector for the ith medium. Here i=1, 2, and 3 refer to air, glass, and water respectively. The angle υ_1 is the angle between the x and x' axes. The measurement volume is at O.

As shown by Fowles (1968), the condition at the interface of two media is

$$\vec{k}_i \cdot \vec{r} = \vec{k}_{i+1} \cdot \vec{r} \tag{A.1.1}$$

where $\vec{r}$ is an arbitrary unit vector in the horizontal plane between the i and i+1 media and hence perpendicular to the y axis. The magnitude of $\vec{k}_i$ is

$$|\vec{k}_i| = \frac{\omega n_i}{c} = 2\pi/\lambda_i$$

where ω is the angular frequency of the electromagnetic wave, λ_i is the wavelength, c is the speed of light in a vacuum and n_i is the refractive index of the ith medium.

With the coordinate system x'y'z' in Figs. A.1 and A.3, it is found that the indicted angles υ_i are all equal to a constant, υ. This can be verified by letting $\vec{r}$ be a unit vector in the plane between the i=1 and 2 media and oriented in the z' direction. Substituting into (A.1.1)

$$\vec{k}_1 \cdot \vec{r} = 0 = \vec{k}_2 \cdot \vec{r}$$

This implies that the $\vec{k}_1$ and $\vec{k}_2$ both lie in the x'-y' plane because there is no component of $\vec{k}_2$ in the z' direction. Hence $\vec{k}_2$ lies in the same vertical plane as $\vec{k}_1$. Since $\vec{k}_2$ is coplanar with $\vec{k}_1$, $\vec{k}_3$ can be similarly shown to be coplanar with $\vec{k}_1$ and $\vec{k}_2$. Hence the angles υ_i are equal:

$$\upsilon_1 = \upsilon_2 = \upsilon_3 \equiv \upsilon$$

Equation (A.1.1) implies Snell's Law which is

$$n_1 \sin \Omega_1 = n_2 \sin \Omega_2 = n_3 \sin \Omega_3 \qquad (A.1.2)$$

The angles Ω_i are the angles that the wavenumber vectors make with the y' axis in the x'-y' plane. The angles $\phi_1/2$ and ζ_1 indicated in Fig. A.2 are known by measurement. In particular $\phi_1/2$ is the beam convergence half angle in air and ζ_1 is the tilted angle (angle between $\vec{k}_1$ vector and the projection of the $\vec{k}_1$ vector in the x-y plane). The beam convergence half angle in water, $\phi_3/2$ (not illustrated) and Ω_3 are unknowns. Using the indicated line segments in the geometric construction of Fig. A.2, the general expressions for $\phi_i/2$ and ζ_i are

$$\sin^2\phi_i/2 = \frac{(x_i - x_{i+1})^2}{(x_i - x_{i+1})^2 + (y_i - y_{i+1})^2 + (z_i - z_{i+1})^2}$$

and

$$\sin^2\zeta_i = \frac{(z_i - z_{i+1})^2}{(x_i - x_{i+1})^2 + (y_i - y_{i+1})^2 + (z_i - z_{i+1})^2}$$

where $\phi_i/2$ and ζ_i are defined analogously to $\phi_1/2$ and ζ_1 . The angle Ω_i is obtained from

$$\sin\Omega_i = \left(\frac{(x_i-x_{i+1})^2 + (z_i-z_{i+1})^2}{(x_i-x_{i+1})^2 + (y_i-y_{i+1})^2 + (z_i-z_{i+1})^2}\right)^{1/2}$$

$$= \left[\sin^2\phi_i/2 + \sin^2\zeta_i\right]^{1/2} \qquad \text{(A.1.3)}$$

and

$$\tan\upsilon = \frac{|(z_i - z_{i+1})|}{(x_i - x_{i+1})} = \frac{\sin\zeta_i}{\sin\phi_i/2} \qquad \text{(A.1.4)}$$

This last result is due to the fact that the beam remains in the x'-y' plane as discussed.

For the first and third layers (air and water) in Eq. (A.1.2), it is found that

$$n_1\sqrt{\sin^2\phi_1/2 + \sin^2\zeta_1} = n_3\sqrt{\sin^2\phi_3/2 + \sin^2\zeta_3}$$

so that usig (A.1.4)

$$n_1\sin\phi_1/2 = n_3\sin\phi_3/2 \qquad \text{(A.1.5)}$$

In the liquid, the doppler frequency (Durst, et al. (1976)) is

$$f_D = \frac{2u\sin\phi_3/2}{\lambda_3} \qquad \text{(3.1)}$$

where u is the velocity in the plane of the two beams and perpendicular to their bisector, the axis of symmetry.

Since the relationship between the moduli of the electromagnetic fields at an interface is time independent, the optical frequency ω must be unchanged. Thus the wavelength varies and λ_i is given by

$$\lambda_i = \frac{n_j \lambda_j}{n_i}$$

for the ith and jth media. For $i=3$, $j=1$, and $n_1 = 1$ for air the doppler frequency f_D is substituting (A.1.5) into (3.1)

$$f_D = \frac{2u \sin \phi_3/2}{\lambda_3} = \frac{2u\ n_3 \sin \phi_1/2}{\lambda_1 n_3}$$

$$= \frac{2u \sin \phi_1/2}{\lambda_1} \qquad \text{(A.1.6)}$$

Hence the doppler frequency is unchanged for passage through media with different indices of refraction, irrespective of the angle of incidence.

It is necessary however to account for a displacement of the focal point in water, relative to the location if only air were present. From Fig. A.3 which shows one of the two input beams in the x'-y' plane, Δy_3, the unknown elevation of the measurement volume at O from the upper surface of the window (which has index n_2), is found to be

$$\Delta y_3 = |x_2' - x_1'|/\tan \Omega_3$$

In terms of the (x,y,z) system, the depth at which the measurement volume is located is y_L such that

$$y_L = \delta_L - \Delta y_3$$

where δ_L is the liquid film depth.

To calculate Δy_3, the relationships between the measurement volume locations if the optical path passed through only air, air and glass, and air, glass, and water media will be considered. In Fig. A.3, y_1' and y_2'

are the elevations at which the focal point would be located for air only and for air and glass optical media respectively. For x_2' and y_1' as indicated the following result is obtained

$$|x_2| = y_1' \tan \Omega_1$$

It is noted that any change in y_1' is exactly equal to the displacement of the focusing lens by the traversing stage on the third mirror module. Now x_1' is given by

$$|x_1'| = \delta_{gl} \tan \Omega_2$$

where δ_{gl} is the glass window thickness so that

$$\Delta y_3 = (y_1' \tan \Omega_1 - \delta_{gl} \tan \Omega_2)/\tan \Omega_3$$

Let

$$y_1' = \Delta y_1 + \delta_{gl} \frac{\tan \Omega_2}{\tan \Omega_1}$$

so that Δy_1 is the displacement (in air) of the lens beyond the location at which the measurement volume was at the upper surface of the window. Then the simple relation

$$\Delta y_3 = \Delta y_1 \tan \Omega_1/\tan \Omega_3 \qquad \text{(A.1.7)}$$

is obtained. This agrees with Durst et al. (1976), although different in form. In practice, the dial gauge reading (in air) at which the beam crossing point intersects the upper window surface is used as a reference and Δy_1 for velocity measurements is obtained by subtraction.

Measurement of ζ_1 and $\phi_1/2$ yielded 13.9° and 13.52°, respectively. For these values, Δy_3 is given by

$$\Delta y_3 = 1.366 \Delta y_1 \qquad \text{(A.1.8)}$$

using (A.1.2), (A.1.3), and (A.1.7). As an indication of the relative insensitivity of this relationship to the value for ζ_1, for $\zeta_1 = 15^\circ$

$$\Delta y_3 = 1.369 \Delta y_1$$

which is a +.2% difference from (A.1.8) and for $\zeta_1 = 10^\circ$

$$\Delta y_3 = 1.357\Delta y_1$$

which is a -.7% difference.

APPENDIX A.2

ESTIMATES OF LDA MEASUREMENT VOLUME DIMENSIONS

Two techniques to estimate the effective measurement volume dimensions were used. The first is a straightforward but laborous application of the ABCD Law (Kogelnik (1965)) to calculate the Gaussian beam parameter following passage through a lens and several media having different indices of refraction. The second technique was to measure the length of the region where the two input beams overlapped. These techniques are discussed in order and the results compared at the conclusion of A.2.

The ABCD law is a bilinear transformation which allows calculation of the diameter and radius of curvature of the phase fronts of paraxial Gaussian beams following passage through homogeneous media, lenses, and interfaces between homogeneous media with differing indices of refraction. The transformation which relates complex Gaussian beam parameters $q(Z_i)$ and $q(Z_j)$ is

$$q(Z_j) = \frac{Aq(Z_i) + B}{Cq(Z_i) + D} \qquad (A.2.1)$$

where A, B, C, and D are determined from the product of fundamental ray matrices for the optical elements and media that constitute the beam path. Here Z_i and Z_j are optical path coordinates such that $Z_j \geq Z_i$.

Spectra Physics provides the following information on the Model 164-08 Argon-ion laser: the beam is 1.5mm in diameter at the 1/e intensity points approximately 11.8cm from the output mirror and exhibits a 5×10^{-4} radian divergence angle, Θ . From this information, one can calculate $q(Z_0)$, where Z_0 is the laser exit plane coordinate. The value of the complex beam parameter $q(Z_i)$ where Z_i is the optical path coordinate for a Gaussian beam propagating in a homogeneous medium is given by (Yariv (1971))

$$q(Z_i) = \frac{\pi\omega_o^2}{\lambda}\left[\frac{\omega_b^2(Z_i)}{\omega_o^2} - 1\right]^{1/2} + i\,\frac{\pi\omega_o^2}{\lambda} \tag{A.2.2}$$

where $\omega_b(Z_i)$ is the Gaussian beam radius (based on the 1/e intensity location) and ω_o is the minimum ω_b (at the beam waist). An approximate relation for ω_o is given by

$$\omega_o \simeq \frac{\lambda}{\pi\Theta} \tag{A.2.3}$$

where Θ has been measured at $Z_i \gg \omega_o^2/\lambda$.

For a lens with focal length f_ℓ , the beam path coordinates Z_0, Z_1, Z_2, δ_{g1} and Δy_3 ; the indices of refraction n_1, n_2, and n_3 ; and beam plane inclination angles T_i (with rspect to the vertical y axis) as shown in Figs. A.1-b and A.4, the total ray matrix is given by the product of the following fundamental ray matrices

$$\begin{vmatrix} A & B \\ C & D \end{vmatrix} = \begin{vmatrix} 1 & \dfrac{\Delta y_3}{\cos T_3} \\ 0 & 1 \end{vmatrix} \begin{vmatrix} 1 & 0 \\ 0 & \dfrac{n_2}{n_3} \end{vmatrix} \begin{vmatrix} 1 & \dfrac{\delta_{g1}}{\cos T_2} \\ 0 & 1 \end{vmatrix} \begin{vmatrix} 1 & 0 \\ 0 & \dfrac{n_1}{n_2} \end{vmatrix}$$

$$\times \begin{vmatrix} 1 & Z_2 - Z_1 \\ 0 & 1 \end{vmatrix} \begin{vmatrix} 1 & Z_1 - Z_0 \\ -\dfrac{1}{f_\ell} & 1 - \dfrac{(Z_1 - Z_0)}{f_\ell} \end{vmatrix}$$

Then A, B, C, and D are given by

$$A = 1 - \frac{(Z_2 - Z_1)}{f_\ell} - \frac{1}{f_\ell}\left(\frac{\delta_{g1}}{n_2 \cos T_2} + \frac{\Delta y_3}{n_3 \cos T_3}\right)$$

$$B = (Z_1 - Z_0) + \left(1 - \frac{(Z_1 - Z_0)}{f_\ell}\right) \left[Z_2 - Z_1 + \left(\frac{\delta_{g1}}{n_2 \cos T_2} + \frac{\Delta y_3}{n_3 \cos T_3}\right)\right]$$

$$C = -(f_\ell n_3)^{-1} \tag{A.2.4}$$

$$D = \frac{1}{n_3}\left(1 - \frac{(Z_1 - Z_0)}{f_\ell}\right)$$

The cosine of the inclination angle is

$$\cos T_i = [\tan^2 \Omega_i \cos^2 \upsilon + 1]^{-1/2}$$

with Ω_i and υ defined in Appendix A.1. The beam parameter of the focal point, $q(Z_3)$ is obtained from Eqs. (A.2.1) and (A.2.4). From Yariv (1971) the Gaussian beam radius at Z_i is

$$\omega_b(Z_i) = \left[-\frac{\pi}{\lambda}\left(\text{Im}\left(\frac{1}{q(Z_i)}\right)\right)\right]^{-1/2} \tag{A.2.5}$$

The vertical extent of the volume is approximated by the product of $\cos T_3$ and the major axis length of the roughly ellipsoidal measurement volume. The major axis length ℓ_m is then given by

$$\ell_m = \frac{2\omega_b(Z_3)}{\sin(\phi_3/2)} = \frac{2n_3\omega_b(Z_3)}{n_1 \sin(\phi_1/2)}$$

so that assuming relatively constant $\omega_b(Z_3)$ in the neighborhood of Z_3 and using Eq. (A.1.5), the vertical extent of the volume is

$$\ell_v = \frac{2n_3}{n_1}\frac{\omega_b(Z_3)\cos T_3}{\sin(\phi_1/2)} \tag{A.2.6}$$

After lengthy but straightforward calculations, the beam diameter of the focal point is found to be

$$d_b = 2\omega_b(Z_3) = 1.0 \times 10^{-4}\text{m}.$$

which is also approximately the streamwise dimension of the scattering volume. As shown above the angle of inclination from the vertical can be calculated knowing Ω_3 and υ

$$T_3 = 10.6^{\circ}$$

The vertical dimension of the volume is from (A.2.6)

$$5.7 \times 10^{-4}\text{m.} \lesssim \ell_v \lesssim 5.8 \times 10^{-4}\text{m.}$$

varying slightly with measurement location. This compares with an average value of the vertical extent of the measurement volume of

$$\ell_{ve} = 5 \times 10^{-4}\text{m.}$$

as measured by observing the beams as they impinged on a target submerged in a stagnant liquid layer in the facility. The observer's criterion of noting the distance over which the beams touch is subjective and hence the discrepancy is understandable. However, it was also found that the beams do not cross perfectly due to slight misalignment of the lens at any given location. Such misalignments would reduce the volume dimensions. The average experimental value will be thus used as the basis of all further calculations because this value takes into account all nonideal aspects of the optical system. Thus for the value of ℓ_{ve} and using (A.2.6) the measurement volume diameter is

$$d_{be} = 9. \times 10^{-5}\text{m.}$$

This value for the measurement volume length is the overall dimension. For a system which requires N fringes to be crossed (N zero crossings of the filtered Doppler signal) the effective volume is only a subregion of the volume common to both beams. For N=32 and for the classical fringe width is (Durst et al. (1976))

$$d_f = \frac{\lambda}{2 \sin \phi/2}$$

Use of $\ell_{ve} = 5 \times 10^{-4}$m the experimentally derived value, yields

$$\ell_{v32} = 3 \times 10^{-4}\text{m} \qquad \text{(A.2.7)}$$

where ℓ_{v32} is the length of the subvolume which has a minimum of 32 fringes. This value is used in the computation of velocity gradient corrections to the u' profile in Appendix A.3.

APPENDIX A.3

BROADENING CONSIDERATIONS

Durst et al. (1976) indicates that the square of the apparent fluctuation u'^2_a is equal to the sum of the square of the actual turbulent rms fluctuation, u'^2_t , plus broadening contributions, u'^2_{bi} which are ficticious increases in the fluctuation level due to various sources. The relation is then

$$u'^2_a = u'^2_t + \sum_i u'^2_{bi}$$

The true fluctuation level u'_t might then be estimated by

$$u'_t = \left[u'^2_a - \sum_i u'^2_{bi}\right]^{1/2} \qquad (A.3.1)$$

The broadening contribution for the present experiment in which a counter type anemometer was used was primarily due to velocity gradient broadening. Errors in the processor clock rate which could also contribute to the broadening error were found by calibration to be negligible. Durst suggests the formula

$$u'^2_{bg} \simeq \ell^2_v \left(\frac{d\bar{u}}{dy}\right)^2 \qquad (A.3.2)$$

to approximate the broadening or apparent increase in the rms fluctuation value when a velocity gradient is aligned along the major axis of the measurement volume. Here u'_{bg} is the apparent increase and $d\bar{u}/dy$ is the mean velocity gradient.

To implement (A.3.2) the mean velocity profile was fitted with an exponential function (which yields finite gradients at the interface) and differentiated. The effective measurement volume major axis ℓ_{v32} from (A.2.7) was substituted for ℓ_v . Then u'^2_{bg} is subtracted from the raw data fluctuation level u'^2_a as indicated in (A.3.2).

A typical value for the ratio u'_{bg}/u'_{a} is .23 at the interface. If the velocity gradient is less steep the ratio will be less than .23. This is true of measurements below the interface in the bulk flow.

APPENDIX B.1

DERIVATION OF THE HEAT TRANSFER COEFFICIENT

A mass balance on the elemental volume in the gas phase yields

$$G = \frac{1}{\Delta x}\left[\int_o^{\delta_c - \delta_L(x_i)} \rho_g u_g(x_i, y_g)dy_g - \int_o^{\delta_c - \delta_L(x_{i+1})} \rho_g u_g(x_{i+1}, y_g)dy_g\right] \quad (B.1)$$

where G is the condensing mass flux, which is positive in the indicated direction.

The condensing heat flux is simply

$$Q_T = GH_g \quad (B.2)$$

where H_g the steam enthalpy is essesntially constant for adiabatic walls and high interfacial condensation rates. Note that all H_2O enthalpies will be defined relative to the 0^oC datum, for which the enthalpy is zero. The thermal energy convected into the liquid layer from the liquid interface is

$$Q_S = G\ c_p\ T_S$$

Following Spalding (1963) the heat transfer coefficient h_{sp} is defined as

$$h_{sp} \equiv \frac{Q_T - Q_S}{T_S - T_L}$$

where T_L is the bulk average (mixed) temperature. Then

$$h_{sp} = G\left(\frac{H_g - c_p T_S}{T_S - T_L}\right) \quad (B.3)$$

This is the heat transfer coefficient definition used in the calculations for the present work. Linehan's data have also been reevaluated using (B.3). Also

$$Q_T = G\ H_g = h_{sp}\left(\frac{H_g}{H_g - c_p\ T_S}\right)(T_S - T_L)$$

$$= h_{sp}\left(1 + \frac{c_p\ T_S}{H_g - c_p\ T_S}\right)(T_S - T_L)$$

and the condensing mass flux is

$$G = h_{sp}\left(1 + \frac{c_p T_S}{H_g - c_p T_S}\right) \frac{(T_S - T_L)}{H_g} \qquad (B.4)$$

The enthalpy term in parentheses which distinguishes (B.4) from the form used by Linehan is

$$\left(1 + \frac{c_p T_S}{H_g - c_p T_S}\right) \sim 1.2$$

typically for the Northwestern data and Linehan's work.

B.2 INTEGRAL ANALYSIS OF MOMENTUM TRANSPORT

From Fig. B.2 for two dimensional flow, a flat interface is assumed so that no streamwise convection of momentum in the two phase region is significant and G and τ^*, the shear stress with condensation, are constant over Δx . Then the force balance on the small element in Fig. B.2

$$\begin{aligned}
0 = -\Delta x b\tau^* &+ b\Big[\int_0^{\delta_c - \delta_L(x_i)} \rho_g u_g^2(x_i, y_g)\,dy_g - \int_0^{\delta_c - \delta_L(x_{i+1})} \rho_g u_g^2(x_{i+1}, y_g)\,dy_g\Big] \\
&+ \Big[P(x_i)b(\delta_c - \delta_L(x_i)) - P(x_{i+1})b(\delta_c - \delta_L(x_{i+1}))\Big] \\
&+ b\,\frac{P(x_i) + P(x_{i+1})}{2}\Big[\delta_L(x_i) - \delta_L(x_{i+1})\Big] \qquad \text{(B.5)} \\
&- U_i b\Big[\int_0^{\delta_c - \delta_L(x_i)} \rho_g u_g(x_i, y_g)\,dy_g - \int_0^{\delta_c - \delta_L(x_{i+1})} \rho_g u_g(x_{i+1}, y_g)\,dy_g\Big] \\
&- \frac{\Delta x}{2}\Big[\tau_w(x_i)\big(2(\delta_c - \delta_L(x_i)) + b\big) + \tau_w(x_{i+1})\big(2(\delta_c - \delta_L(x_{i+1})) + b\big)\Big]
\end{aligned}$$

In (B.5) the first term is the shear force at the interface with condensation. The second term is the change in the gas momentum flux overΔx. The third and fourth terms are streamwise pressure forces on the elemental volume in the gas. The fifth term is the momentum flux convected into the liquid by the mean condensing flow and the last term is the smooth wall shear force.

Note that τ_w, the upper smooth wall shear is represented by an average over Δx and that P is a function only of the streamwise coordinate. The Blasius correlation is assumed valid for the small effect that τ_w represents in condensing flow.

To obtain U_i, the interface velocity, the liquid film is approximated by a Couette flow such that the average velocity U_L is

$$U_L = \frac{1}{\delta_L}\int_0^{\delta_L} u(y_L)\,dy_L = \frac{U_i}{2}$$

Rearranging yields

$$U_i = 2U_L \quad . \tag{B.6}$$

In the results section, LDA measurements confirm the reasonableness of (B.6) for the magitude of the effect considered.

It is noted that

$$P(x_i)\,(\delta_c - \delta_L(x_i)) - P(x_{i+1})(\delta_c - \delta_L(x_{i+1}))$$
$$+ \frac{P(x_i) + P(x_{i+1})}{2}\,[\delta_L(x_i) - \delta_L(x_{i+1})]$$
$$= (P(x_i) - P(x_{i+1}))[\delta_c - (\delta_L(x_i) + \delta_L(x_{i+1}))/2]$$

Thus simplifying the interface shear with condensation is

$$\begin{aligned}\tau^* = {} & \frac{1}{\Delta x}\,\Big[\int_o^{\delta_c - \delta_L(x_i)} \rho_g u_g^2(x_i,y_g)dy_g - \int_o^{\delta_c - \delta_L(x_{i+1})} \rho_g u_g^2(x_{i+1},y_g)dy_g\Big] \\ & + \frac{1}{\Delta x}\,(P(x_i) - P(x_{i+1}))[\delta_c - \frac{1}{2}\,(\delta_L(x_i) + \delta_L(x_{i+1}))] \\ & - \frac{2U_L}{\Delta x}\,\Big[\int_o^{\delta_c - \delta_L(x_i)} \rho_g u_g(x_i,y_g)dy_g - \int_o^{\delta_c - \delta_L(x_{i+1})} \rho_g u_g(x_{i+1},y_g)dy_g\Big] \\ & - \frac{1}{2b}\,[\tau_w(x_i)(2(\delta_c - \delta_L(x_i)) + b) + \tau_w(x_{i+1})(2(\delta_c - \delta_L(x_{i+1})) + b)]\end{aligned} \tag{B.7}$$

Data from the five pitot traverse locations are plotted vs. x, smooth curves for G, the integrated gas momentum flux, δ_L, and P are faired by hand. Values for these parameters are taken from the faired curves at Δx = .1m intervals to calculate local values of h_{sp} and τ^*.

REFERENCES

Adrian, R. J. "Laser Velocimetry," T&AM Report No. 442, Univ. of Illinois, Urbana (1980).

Akai, M., Inoue, A., Aoki, S., and Endo, K. "A Co-Current Stratified Air-Mercury Flow with Wavy Interface," Int. J. Multiphase Flow, Vol. 6, No. 3, p. [illegible] (1980).

Asia, L., Caussade, B., George, J., and Masbernat, L. "Exchanges De Gaz Dissous En Écoulements Stratifies De Gaz Et De Liquide," Int. J. Heat and Mass Transfer, Vol. 24, No. 6, p. 1005 (1981).

Bankoff, S. G. "Brief Literature Review Pertinent to Steam Generator Waterhammer," PWR Steam Generator Water Hammer Workshop, EPRI, Palo Alto, CA. (1978).

Batchelor, G. K. The Theory of Homogeneous Turbulence, Cambridge Univ. Press, London (1967).

Block, J. A. "Condensation-Driven Fluid Motions," Int. J. Multiphase Flow, 6, p. 113 (1980).

Buchhave, P., et al., ed. The Accuracy of Flow Measurements by Laser Doppler Methods, Proceedings of The LDA-Symposium, Copenhagen 1975, Hemisphere Publishing, Washington, DC (1976).

Butterworth, D., and Hewitt, G. F., ed. Two-Phase Flow and Heat Transfer, Oxford Univ. Press (1977).

Calderbank, P. H., and Moo-Young, M. B. "The Continuous Phase Heat and Mass-Transfer Properties of Dispersions," Chem. Eng. Sci., 16, p. 39 (1961).

Carpenter, E. F., and Colburn, A. P. "The Effect of Vapor Velocity on Condensation Inside Tubes," The Instn. of Mech. Eng., Proc. of the General Discussion on Heat Transfer, p. 20 (1951).

Chang, P. C., Plate, E. J., and Hidy, G. M.: "Turbulent Air Flow Over the Dominant Component of Wind-Generated Water Waves," J. Fluid Mech., 47, pt. 1, p. 183 (1971).

Charnock, H. "Wind Stress on a Water Surface," Quart. J. Roy. Met. Soc., 81, p. 639 (1955).

Cohen, L. S. "Interaction Between Turbulent Air and a Flowing Liquid Film," Ph.D. Thesis, Univ. of Illinois, Urbana (1964).

Cohen, L. S., and Hanratty, T. J. "Effect of Waves at a Gas-Liquid Interface on a Turbulent Air Flow," J. Fluid Mech., 31, pt. 3, p. 467 (1968).

Daly, B. J., and Harlow, F. H. "Numerical Study of Condensation in Cocurrent Stratified Flows," NUREG/CR-1108 (1980).

Danckwerts, P. V. "Significance of Liquid-Film Coefficients in Gas Absorption," Ind. Eng. Chem., 43, No. 6, p. 1460 (1951).

Davidson, S. "An Experimental Investigation of Steam-Water Condensation in a Horizontal Channel," M.S. Thesis, Northwestern Univ. (1978).

Davies, J. T. Turbulence Phenomena, Academic Press NY (1972).

Davies, J. T., and Lozano, F. J. "Turbulence Characteristics and Mass Transfer at Air-Water Surfaces," AIChE J., Vol. 25, No. 3, p. 405 (1979).

Durst, F., Melling, A., and Whitelaw, J. H. Principles and Practice of Laser-Doppler Anemometry, Academic Press NY (1976).

Eloubaidy, A. F. "Wind Waves and the Reaeration Coefficient in Open Channel Flow," Ph.D. Thesis, Colorado State Univ. (1969).

Fortescue, G. E., and Pearson, J. R. A. "On Gas Absorption into a Turbulent Liquid," Chem. Eng. Sci., 22, p. 1163 (1967).

Fowles, G. R. Introduction to Modern Optics, Holt, Rinehart and Winston, NY (1968).

Gayral, B. "Bilans d'Énergie Turbulente en Écoulement Stratifié Cocourant de Gas et de Liquide," PhD. Thesis, L'Institute National Polytechnique de Toulouse (1979).

George, W. K., Jr. "Limitations to Measuring Accuracy Inherent in the Laser Doppler Signal," in Proceedings of the LDA Symposium, Copenhagen 1975, Hemisphere Publishing, Washington, DC (1976).

Hadj-Fredj, A. "Structure Cinematique de l'Écoulement Stratifié ou Ondulé d'un Gaz et d'un Liquide," Ph.D. Thesis, L'Institut National Polytechnique de Toulouse (1978).

Hanjalić, K., and Launder, B. E. "Fully Developed Asymmetric Flow in a Plane Channel," J. Fluid Mech., 51, pt. 2, p. 301 (1972).

Hanratty, T. J., and Engen, J. M. "Interaction Between a Turbulent Air Stream and a Moving Water Surface," AIChE J., 3, No. 3, p. 299 (1957).

Harriott, P., and Hamilton, R. M. "Solid-Liquid Mass Transfer in Turbulent Pipe Flow," Chem. Eng. Sci., 20, p. 1073 (1965).

Hidy, G. M., and Plate, E. J. "Wind Action on Water Standing in a Laboratory Channel," J. Fluid Mech., 26, pt. 4, p. 651 (1966).

Higbie, R. "The Rate of Absorption of a Pure Gas Into a Still Liquid During Short Periods of Exposure," Trans. AIChE, 31, p. 365 (1935).

Hinze, J. O. Turbulence, McGraw-Hill, NY (1975).

Hughmark, G. A. "Heat and Mass Transfer for Turbulent Pipe Flow," AIChE J., 17, No. 4, p. 902 (1971).

Jeffries, R. B., Scott, D. S., and Rhodes, E. "Structure of Turbulence Close to the Interface in the Liquid Phase of a Co-Current Stratified Two-Phase Flow," Proc. Instn. Mech. Engrs., 184, pt. 3c, p. 204 (1969).

Kays, W.M., and Crawford, M. E. Convective Heat and Mass Transfer, McGraw-Hill, NY (1980).

Kim, H. T., Kline, S. J., and Reynolds,W. C. "The Production of Turbulence Near a Smooth Wall in a Turbulent Boundary Layer," J. Fluid Mech., 50, pt. 1, p. 133 (1971).

King, C. J. "Turbulent Liquid Phase Mass Transfer at a Free Gas-Liquid Interface," I. and E.C. Fund., 5, No. 1, p. 1 (1966).

Kishinevsky, M. Kh. "Two Approaches to the Theoretical Analysis of Absorption Processes," J. Appl. Chem. USSR, 28, p. 881 (1955).

Kishinevsky, M. Kh., and Serebryansky, V. T. "The Mechanism of Mass Transfer at the Gas-Liquid Interface with Vigorous Stirring," J. Appl. Chem. USSR, 29, p. 29 (1956).

Kogelnik, H. "Imaging of Optical Modes -- Resonators with Internal Lenses," Bell System Technical J., p. 455 (1965).

Kondo, J. "Parameterization of Turbulent Transport in the Top Meter of the Ocean," J. of Phys. Oceanography, 6, p. 712 (1976).

Krenkel, P. A., and Orlob, G. T. "Turbulent Diffusion and the Reaeration Coefficient," ASCE, J. of Sanitary Engineering Div., 88, SA2, p. 53 (1962).

Krieth, F. Principles of Heat Transfer, 2nd ed., Internat'l Textbook Co., Scranton, PA. (1968).

Lamb, H. Hydrodynamics, 6th ed., Dover, NY (1945).

Lamont, J. C. "Gas Absorption in Cocurrent Turbulent Bubble Flow," Ph.D. Thesis, Univ. British Columbia (1966).

Laufer, J. "Investigaton of Turbulent Flow in a Two-Dimensional Channel," NACA Report No. 1053 (1954).

Laufer, J. "The Structure of Turbulence in Fully Developed Pipe Flow," NACA Report No. 1174 (1954).

Lee, L. "Studies of Condensation Rate in Steam-Water Cocurrent Flow," M.S. Thesis, Northwestern Univ. (1979).

Levich, V. G. Physicochemical Hydrodynamics, Prentice Hall, Inc., Englewood Cliffs, NJ (1962).

Lewis, W. K., and Whitman, W. G. "Principles of Gas Absorption," Ind. Eng. Chem., 16, No. 12, p. 1215 (1924).

Lim, I. "Cocurrent Steam and Water Flow in a Horizontal Channel," M.S. Thesis, Northwestern Univ. (1981).

Linehan, J. H. "The Interaction of Two-Dimensional, Stratified, Turbulent Air-Water and Steam-Water Flows," Ph.D. Thesis, University of Wisconsin (1968).

Mattlingly, G. E. "Experimental Study of Wind Effects on Reaeration," J. Hydraulics Div., HY3, 103, p. 311 (1977).

McQuivey, R. S., and Richardson, E. V. "Some Turbulence Measurements in Open Channel Flow," J. of Hydraulics Div., Proc. of ASCE, Vol. 95, No. HY1, p. 209 (1969).

Mickley, H. S., Ross, R. C., Squyers, A. L., and Stewart, W. E. "Heat, Mass, and Momentum Transfer for Flow over a Flat Plate with Blowing or Suction," NACA TN 3208 (1954).

McLaughlin, D. K., and Tiederman, W. G. "Biasing Correction for Individual Realization of Laser Anemometer Measurements in Turbulent Flows," Phys. of Fluids, 16, 12, p. 2082 (1973).

Nalluri, C., and Novak, P. "Turbulence Characteristics in a Smooth Open Channel of Circular Cross Section," J. of Hydraulic Res., No. 4, p. 343 (1973).

O'Connor, D. J., and Dobbins, W. E. "Mechanism of Reaeration in Natural Streams," Trans. ASCE, 123, p. 641 (1958).

Otnes, R. K., and Enochson, L. Digital Time Series Analysis, John Wiley and Sons, NY. (1972).

Plate, E. J., Chang, P. C., and Hidy, G. M. "Experiments on the Generation of Small Water Waves by Wind," J. Fluid Mech., 35, pt. 4, p. 625 (1969).

Raichlen, F. "Some Turbulence Measurements in Water," J. of Eng. Mech. Div., Proc. of ASCE, Vol. 93, No. EM2, p. 73 (1967).

Richardson, E. V., and McQuivey, R. S. "Measurement of Turbulence in Water," J. of Hydraulics Div., Proc. of ASCE, Vol. 94, No. HY2, p. 411 (1968).

Rohatgi, U. S. and Saha, P. "Constitutive Relations in TRAC-P1A," NUREG/CR-1651 (1980).

Schlichting, H. Boundary - Layer Theory, McGraw-Hill, NY (1968).

Segev, A., Flanigan, L. J., Kurth, R. E., and Collier, R. P. "Countercurrent Steam Condensation and Its Application to ECC Penetration," Int. J. Heat Transfer (in press) (1981).

Shankar, P. N., and Marble, F. E. "Kinetic Theory of Transient Condensation and Evaporation at a Plane Surface," Physics of Fluids, Vol. 14, No. 3, p. 510 (1971).

Shemdin, O. H. "Wind Generated Current and Phase Speed of Wind Waves," J. of Phys. Oceanography, 2, p. 411 (1972).

Spalding, D. B. Convective Mass Transfer, McGraw-Hill. NY (1963).

Street, R. L. "Turbulent Heat and Mass Transfers Across a Rough, Air-Water Interface: A Simple Theory," Int. J. Heat and Mass Transfer, Vol. 22, p. 885 (1979).

Street, R. L., and Miller, A. W. "Determination of the Aqueous Sublayer Thicknesses at an Air-Water Interface," J. Phys. Oceanography, 7, p. 110 (1977).

Suzanne, Ch. "Etude d'un Écoulement Stratifié Gaz-Liquide," Ph.D. Thesis, L'Institut National Polytechnique de Toulouse (1977).

Tchen, C. M. "On the Spectrum of Energy in Turbulent Shear Flow," J. Nat'l Bur. of Stds., Vol. 50, No. 1, p. 51 (1953).

Tennekes, H., and Lumley, J. L. A First Course in Turbulence, MIT Press, Cambridge, MA (1972).

Theofanous, T. G., Houze, R. N., and Brumfield, L. K. "Turbulent Mass Transfer at Free, Gas-Liquid Interfaces, with Applications to Open-Channel, Bubble, and Jet Flows," Int. J. Heat Mass Trans., 19, p. 613 (1976).

Theofanous, T. G., Houze, R. N., and Johns, D. M.: "Horizontal, Stratified Gas-Liquid Flow: the Interfacial Region," AIChE Symposium on Heat Transfer, San Francisco, CA. (1975).

Thomas, R. M. "Condensation of Steam on Water in Turbulent Motion," Int. J. Multiphase Flow, Vol. 5, p. 1 (1979).

Ueda, H., Moeller, R., Komori, S., and Mizushina, T. "Eddy Diffusivity Near the Free Surface of Open Channel Flow," Int. J. Heat Mass Transfer, 20, p. 1127 (1977).

Wallis, G. B. One-Dimensional Two-Phase Flow, McGraw-Hill, NY (1969).

BEST DOCUMENT AVAILABLE

Wu, J. "Laboratory Studies of Wind-Wave Interactions," J. Fluid Mech., 34, pt. 1, p. 91 (1968).

Yariv,A. Introduction to Optical Electronics, Holt, Rinehart and Winston, NY (1971).

NOMENCLATURE

A = Coefficent in Gaussian beam propagation law (Appendix A.2).

a = Dimensional coefficient in King's model for the liquid eddy diffusivity.

a_g = Speed of sound in gas (m/s).

B = Coefficient in Gaussian beam propagation law (Appendix A.2).

b = Channel width (m).

b_f = Blowing parameter.

b_* = Argument in quadratic formula for u_{*e} (m/s).

C = Coefficient in Gaussian beam propagation law (Appendix A.2).

C_1,C_2 = Constants in Eqs. (4.22) and (4.23).

c_f = Friction coefficient.

c_m = Minimum wave phase speed from classical theory (m/s).

c_p = Specific heat of water at constant pressure (kj/kg ^oC) .

D = Coefficient in Gaussian beam propagation law (Appendix A.2).

D = Laminar binary diffusion coefficient (m^2/s) .

D_f = Damping factor in Ueda's model.

D_{eff} = Effective diffusivity (m^2/s) .

D_h = Liquid film hydraulic diameter (m).

D_p = Pipe diameter (m).

D_t = Turbulent diffusion coefficient (m^2/s) .

d = Thermal boundary layer thickness in Daly and Harlow's model (m).

d_b = Calculated LDV measurement volume diameter at the waist (m).

d_{be} = Experimentally observed LDV measurement volume diameter at the waist (m).

d_f = LDV measurement volume fringe width (m).

d_1, d_2, d_3 = Constants in Eqs. (4.30), (4.31), and (4.32).

$E(n_w)$ = One dimensional turbulence energy spectrum function (m^3/s^2) (m^2/s^3 for E(n)).

$\vec{E}_{ls}, \vec{E}_{rs}$ = Scattered light electromagnetic wave vectors (v).

$F(n)$ = Energy spectrum function E(n) normalized by turbulence intensity (s^{-1}) .

f = Pipe flow resistance coefficient.

f_ℓ = Focal length (m).

f_D = Doppler frequency (Hz).

G = Interphase mass flux ($kg/m^2 s$) .

g = Gravitational acceleration (m/s^2) .

g_{sp} = Spalding conductance ($kg/m^2 s$) .

H_{fg} = Heat of vaporization (kj/kg) .

H_g = Steam enthalpy relative to 0°C datum (kj/kg) .

h = Heat transfer coefficient.

= $Q_T/(T_S - T_L)$ ($kw/m^2\ ^\circ C$) .

h_e = Engineering estimate value of h_{sp} ($kw/m^2\ ^\circ C$) .

h_{sp} = Spalding heat transfer coefficient = $Q_{SD}/(T_S - T_L)$ ($kw/m^2\,^oC$) .

$I(t)$ = Scattered light intensity (w/m^2) .

$I(t_T)$ = Inlet effect function Theofanous's large eddy model.

J_c = Constant in Daly and Harlow's model.

K = Generalized transport coefficient (m/s).

k_e = Engineering estimate for k_L (m/s).

k = Liquid thermal conductivity (kw/m^oC) .

$k_H = h/\rho c_p$ = Davies' thermal transport group (m/s).

k_L = Mass transfer coefficient (m/s).

k_{Le} = Engineering estimate for k_L (m/s).

k_{LFS} = Mass transfer coefficient in Lamont's free surface model (m/s).

k_{LS} = Mass transfer coefficient in Lamont's sheared interface model (m/s).

k_s = Equivalent sand grain roughness for the interface (m)

k_t = Turbulent thermal conductivity (kw/m^oC) .

$\vec{k}_i$ = Optical wave propagation vector for ith medium; (m^{-1}) i=1,2, and 3 refer to air, glass, and water, respectively.

$\vec{k}_{li}, \vec{k}_{ri}$ = Incident wave propagation vectors at measurement volume (m^{-1}) .

$\vec{k}_{sc}$ = Scattered wave propagation vector (m^{-1}) .

ℓ = Lamont eddy cell length scale (m).

ℓ_m = Calculated LDA measurement volume length (m).

ℓ_v = Calculated vertical extent of the measurement volume (m).

ℓ_{ve} = Experimentally observed vertical extent of the measurement volume (m).

ℓ_{v32} = Length of subvolume having a minimum of 32 fringes and based on ℓ_{ve} (m).

M = Molecular weight.

m = Exponent in King's model for eddy diffusivity.

N = Number of doppler cycles.

N_{ev} = Number of doppler events in a data sample.

$Nu_{\delta_L} = \frac{h_{sp}\delta_L}{k}$ = Nusselt number based on liquid layer thickness.

$Nu_t = \frac{h_{sp}\Lambda}{k}$ = Turbulent Nusselt number.

$Nu_x = \frac{h_{sp}x}{k}$ = Nusselt number based on streamwise distance.

n = Frequency of turbulent motion (Hz).

n_i = Index of refraction for ith medium; i=1,2, and 3 indicates air, glass and water respectively.

n_w = wavenumber (m^{-1}).

Δn = Fundamental frequency increment between energy spectrum estimates (Hz).

O = LDV measurement volume location (Appendix A).

Pr = Liquid Prandtl number.

p = Pressure (Pa).

p_g = Gas pressure (Pa).

P_L = Liquid phase equilibrium vapor pressure at surface temperature (Pa).

Δp = Difference between the gas phase vapor pressure and the equilibrium vapor pressure at the surface temperature (Pa).

Q_S = Convected flux of θ at the interface.

Q_{SD} = Laminar or turbulent diffusive flux of θ at the interface in the liquid.

Q_T = Total transverse flux of θ in the bulk gas phase.

q = Gaussian beam parameter (m).

q_L = Liquid turbulence kinetic energy per unit mass (m^2/s^2) .

R = Universal gas constant (kj/kg mole ^oK) .

Re_g = Reynolds number based on gas phase hydraulic diameter.

Re_h = Reynolds number of liquid channel flow based on film hydraulic diameter.

Re_L = Reynolds number of liquid based on thickness
= $U_L \delta_L / \nu$.

Re_t = Turbulence Reynolds number = $u' \Lambda / \nu$.

$\vec{r}$ = Unit vector in the plane of the lower glass surface (Appendix A.1).

r_L = Thickness of region of surface damped turbulence in Levich model (m).

Sc = Schmidt number.

Sh_{δ_L} = Sherwood number based on liquid thickness = $k_L \delta_L / D$.

Sh_x = Sherwood number based on streamwise distance = $k_L x/D$.

S_L = Liquid turbulence decay length in Daly and Harlow's model (m).

s = Danckwerts's surface renewal rate (s^{-1}) .

T = Temperature (^{o}C or ^{o}K) .

T_L = Bulk liquid temperature (^{o}C) .

T_S = Liquid temperature at the interface (^{o}C) .

T_{sd} = Data sampling period (s).

t = Time (s).

t_a = Surface age (time elapsed since a surface renewal) in King's model (s).

t_e = Surface renewal period (s).

t_{ex} = Interface exposure time (from the inlet) in Theofanous's model (s).

t_k = Dimensionless phase contact time in King's model.

t_T = Dimensionless interface exposure time in Theofanous's model.

Δt = Sampling interval (s).

$\tilde{U}$ = Dimensionless relative gas velocity = $(U_g - U_L)/c_m$.

U_∞ = Free stream velocity (m/s).

$\tilde{U}_{crit}$ = Critical dimensionless velocity for the appearance of waves.

U_g = Gas phase mean velocity (m/s).

U_i = Interface velocity (m/s).

U_L = Liquid phase average velocity (m/s).

$\vec{u}$ = Streamwise velocity (m/s).

u' = Streamwise rms turbulent velocity fluctuation (m/s).

u'_a = Apparent rms velocity fluctuation as measured by LDV (Appendix A.3) (m/s).

u'_{bg} = Velocity gradient induced broadening term (Appendix A.3) (m/s).

u'_{bi} = The ith contribution to the rms velocity fluctuation broadening term where i indicates the source of the broadening term (Appendix A.3) (m/s).

u'_t = True rms velocity fluctuation (m/s).

u'_i = Interface rms turbulent velocity fluctuation (m/s).

$u'_{.5}$ = Liquid rms fluctuation at $y/\delta_L = .5$ (m/s).

u_* = Liquid phase interface shear velocity (m/s).

u_{*e} = Engineering estimate for shear velocity (m/s).

$u_*|_c$ = Calculated interface shear velocity based on Eqs. (5.5) and (5.6) (m/s).

$u_*|_{c*}$ = Calculated interface shear velocity for condensing flow based on $u_*|_c$ and Linehan's correlation for the effect of condensation on the shear stress (m/s).

$u_*|_{5.4}$ = Calculated interface shear velocity based on Eq. (5.4) (m/s).

u_{*f} = Floor or pipe wall shear velocity (m/s).

u_{*FB} = Interface shear velocity from gas phase force balance (m/s).

u_{*g} = Gas phase interface shear velocity (m/s)

= $u_*(\rho/\rho_g)^{1/2}$.

u_{*LDA} = Interface shear velocity from LDA velocity profile (m/s).

u_c = Characteristic turbulent velocity scale in Lamont's model (m/s).

$u_g(x,y)$ = Local gas phase velocity (Appendix B) (m/s).

$u_L(x,y)$ = Local mean liquid velocity.

V_i = Instantaneous velocity based on a single doppler event (m/s).

$\langle V \rangle$ = Event averaged velocity (m/s).

$\bar{V}$ = Time average velocity (m/s).

v = Transverse velocity (m/s).

v' = Transverse fluctuation velocity (m/s).

We = Weber number.

w_g = Gas mass flow rate (kg/s).

w_L = Liquid mass flow rate (kg/s).

x = Streamwise distance from the inlet; with numerical subscripts refers to specific points in Appendix A figures (m).

x' = Distance along an axis defined by the projection of $\vec{k}_1$ on the lower glass surface (m).

x_B = Hughmark's turbulence burst length scale (m).

Δx = Increment in streamwise coordinate (m).

Y_L = Mass fraction in the bulk liquid flow.

Y_S = Mass fraction in the liquid at the interface.

Y_T = Mass fraction in the gas phase.

y = Vertical distance from the plane of the inlet; with numerical subscripts refers to specific points in Appendix A figures (m).

y_+ = Normalized vertical depth below the local interface $= y_L u_{*LDA}/\nu = (\delta_L - \Delta y_3) u_{*LDA}/\nu$.

y' = Vertical distance referenced to the lower glass surface (Appendix A) (m).

y_g = Vertical distance above the interface in the gas (m).

y_L = Vertical distance below the interface in the liquid (m).

Δy_1 = Elevation of focusing lens in air above point where the measurement volume is at the channel floor (m).

Δy_3 = Actual measurement volume elevation above the channel floor (m).

z_0 = Optical path coordinate at laser head (m).

z_1 = Optical path distance from beam waist to lens (m).

z_2 = Optical path distance from beam waist to the outside glass surface (m).

z_3 = Optical path distance from beam waist to the LDA measurement volume (m).

z = Spanwise distance from the center of the inlet; with coordinates refers to specific points in Appendix A figures (m).

z' = Distance normal to x' axis and in the plane of the glass (m).

SUBSCRIPTS

g = Gas phase quantity.

i = Refers to angle or distance in ith medium where $i=1$ or 2 for air or glass, respectively. For $i=3$ or 4 for the medium is water (Appendix A).

i = Refers to streamwise coordinate of control volume boundary (Appendix B).

GREEK NOTATION

α = Exponent of Pr in correlating group.

β = Exponent of Sc in correlating group.

Γ = Function containing effects of Schmidt and Reynolds numbers on K.

γ = Generalized diffusivity in Fick's Law diffusion of θ (m^2/s).

= $k/\rho c_p$ for heat transfer

= D for mass transfer.

δ = Diffusion boundary layer thickness (m).

δ_c = Channel height (m).

δ_{gl} = Glass window thickness (m).

δ_{gmax} = Displacement of the maximum in the gas velocity profile from the interface (m).

δ_L = Average liquid film thickness (m).

δ'_L = Liquid wave amplitude (m).

δ'_{LE} = Effective wave amplitude (m).

ζ_i = Angle between $\vec{k}_i$ and projected component of $\vec{k}_i$ in the x-y plane (deg).

Θ = Gaussian angular beam spread, half angle (rad).

θ = Scalar quantity, either enthalpy or mass fraction.

$\Delta\theta$ = Driving potential for $\theta = \bar{\theta}_S - \bar{\theta}_L$.

$\bar{\theta}_S$ = Time average value of θ at the interface in the liquid

$\bar{\theta}_L$ = Time average value of θ in the bulk liquid flow.

$\bar{\theta}_T$ = Time average value of θ in gas phase.

ϵ = Dissipation rate of turbulence energy per unit mass (m^2/s^3) .

κ = Von Karman constant.

Λ = Turbulence length macroscale (m).

λ = Wavelength (m).

λ_+ = Normalized spanwise surface wavelength in Ueda's eddy diffusivity model $= \lambda u_{*f}/\nu$.

μ = Exponent of liquid fraction term in equation for τ .

ν = Liquid kinematic viscosity (m^2/s) .

ν_g = Gas kinematic viscosity (m^2/s) .

ν_t = Turbulent liquid eddy viscosity (m^2/s) .

ξ = Constant of proportionality between eddy length scale ℓ and ν/u_*.

ρ = Liquid density (kg/m^3) .

ρ_g = Gas density (kg/m^3) .

ρ_S = Density at state S (interface in liquid) (kg/m^3).

σ = Surface tension (N/m).

τ = Interface shear stress with no mass transfer (N/m^2) .

τ^* = Interface shear stress with mass transfer (N/m^2) .

$\tau^*|_{2.31}$ = Predicted value of τ^* based on Linehan's model (N/m^2) .

$\tau^*|_{2.33}$ = Predicted value of τ^* based on Mickley's model (N/m^2) .

τ_b = Shear stress at a fluid boundary (N/m^2) .

τ_w = Solid wall shear stress (N/m^2) .

T_i = Angle between the plane of the input beams in the ith medium and the y axis (deg).

υ = Angle between the plane containing the $\vec{k}_i$ vectors and x axis (deg).

υ_i = Angle between the projection of the $\vec{k}_i$ vector in the x-z plane and the x axis (deg).

ϕ = Danckwerts's function for the fractional surface area renewal rate (Hz).

ϕ_i = Beam convergence angle in the ith medium (deg).

Ω = Value of the constant in Eq. (5.13) and (5.14).

Ω_i = Angle between the $\vec{k}_i$ vector and the y axis.

ω = Optical frequency of incident laser beams (Angular) (rad/s).

ω_b = Gaussian beam radius (m).

ω_D = Doppler shift frequency (Angular) (rad/s).

ω_o = Gaussian beam radius at beam waist (m).

TABLE 2-1

SUMMARY OF OTHER COCURRENT FLOW EXPERIMENTS

Experiment	Length(m)	Width(m)	Height(m)	Re_g		Re_L	
Linehan (1968)	.457	.152	.0167	1.4×10^4	1.75×10^4	2.5×10^2	1.8×10^3
Asia, et al (1981) Small Contactor	6.	.2	.1	1.7×10^4	7.8×10^4	3.5×10^3	1.6×10^4
Asia, et al (1981) Large Contactor	19.5	.6	.95	2.7×10^5	6.4×10^5	3.27×10^3	2.13×10^4
Mattingly (1977)	8	.55	.54	9×10^4	3.6×10^5	1.2×10^4	4.9×10^4
Eloubaidy (1969)	15.8	.61	.76	2.8×10^5	4.8×10^5	2.7×10^4	4.3×10^4
Hidy and Plate (1966) Plate, et al. (1969) Chang, et al. (1971)	12	.61	.76	3.1×10^5	6.6×10^5	-----	-----
Cohen and Hanratty (1968) Cohen (1964)	6.4	.304	.0258	7.2×10^3	1.9×10^4	2.1×10^2	6.57×10^2
Theofanous, et al. (1975)	6.4	.914	.076	1.2×10^4	6×10^4	4.8×10^3	2.1×10^4
Wu (1968)	14	1.5	1.5	1.4×10^5	5.3×10^5	-----	-----

TABLE 5-1

LDA Test Matrix

Run	w_L(kg/s)	w_g(kg/s)
254	.7	.074
274	1.1	.076
294a	1.4	.079
294b	1.7	.075
297	1.4	.125

TABLE 5-2
INTERFACE SHEAR VELOCITY MEASUREMENTS

LDA Run No.	Steam Run No.	Location	u_{*FB}	u_{*LDA}	$\frac{u_{*FB}-u_{*LDA}}{u_{*FB}}$
153	274	3	.0254	.0294	-.157
154	294a	3	.0293	.0391	-.334
155	294a	3	.0293	.0309	-.055
156	294b	3	.0197	.0286	-.452
158	297	3	.0511	.0476	.0685
159	274	1	.0486	.0446	.0823
160	294a	1	.0420	.0436	-.0381
161,2	294b	1	.0405	.0413	-.0198
163	294b	1	.0405	.0409	-.0099
165	297	1	.0665	.0804	-.209
166	274	2	.0404	.0410	-.0149
167	294a	2	.0407	.0483	-.187
168	294b	2	.0357	.0451	-.263
170	297	2	.0396	.0600	-.515
171	294a	2	.0407	.0392	.0369
171-A	297	2	.0396	.0406	-.0253
171-B	297	2	.0396	.0465	-.174
173	254	1	.0178	.0110	.382
174	274	1	.0486	.0418	.140
175	254	3	.0412	.0345	.163
176	294b	1	.0405	.0397	.0198
177	294a	1	.04[illegible]	.0426	-.0143
179	274	3	.0254	.0304	-.197
180	294a	3	.0293	.0343	-.171
181	297	3	.0511	.0509	.004

TABLE 5-3

LIST OF SYMBOLS FOR AIR-WATER SHEAR DATA

□	Asia, et al. (1981)	Small Contactor
△	Asia, et al. (1981)	Large Contactor
○	Mattingly (1973)	
+	Theofanous, et al. (1975)	
×	Hidy and Plate (1966) and Plate, et al. (1969)	
Y	Cohen (1964)	
◇	Wu (1968)	

TABLE 5-4

LIST OF SYMBOLS FOR HEAT AND MASS TRANSFER DATA

□	NU Data,	x = .157m
○	NU Data,	x = .306m
△	NU Data,	x = .586m
+	NU Data,	x = .868m
×	NU Data,	x = 1.23m
Y	Linehan Data	
◇	Gas Absorption Data	

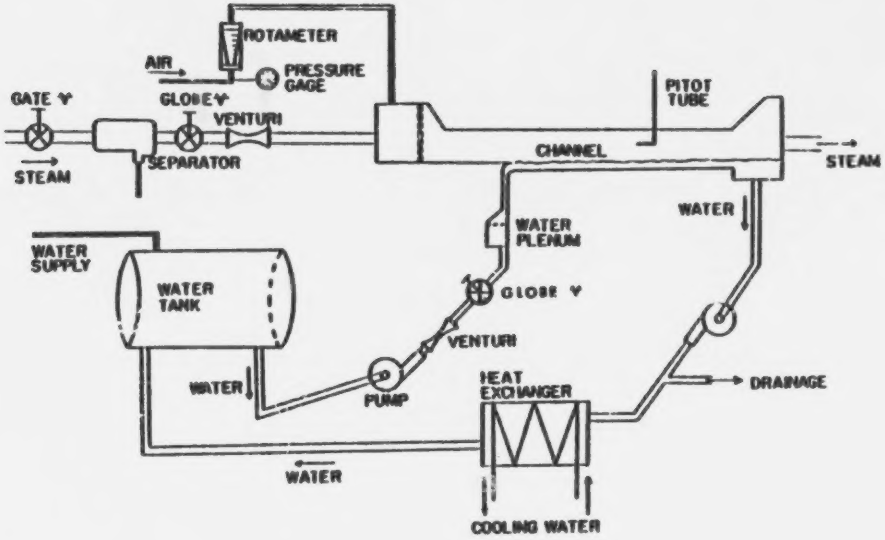
ROTAMETER
AIR
PRESSURE GAGE
GATE V
GLOBE V
VENTURI
PITOT TUBE
STEAM
SEPARATOR
CHANNEL
STEAM
WATER
WATER PLENUM
WATER SUPPLY
WATER TANK
GLOBE V
VENTURI
WATER
PUMP
HEAT EXCHANGER
DRAINAGE
WATER
COOLING WATER

Figure 3.1 Schematic Diagram of the Steam and Water Loop

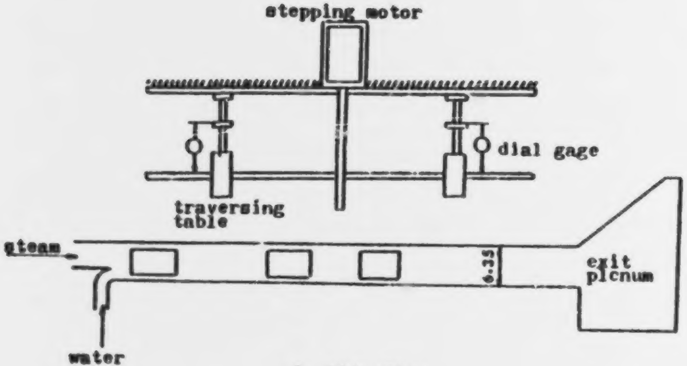
stepping motor
dial gage
traversing table
steam
water
6.35
exit plenum

a). Side View

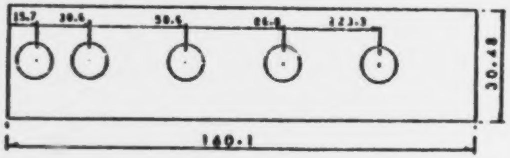
15.7
30.6
58.5
86.8
123.3
30.48
140.1

b). Plan View

Figure 3.2 Channel View. Dimensions in Centimeters

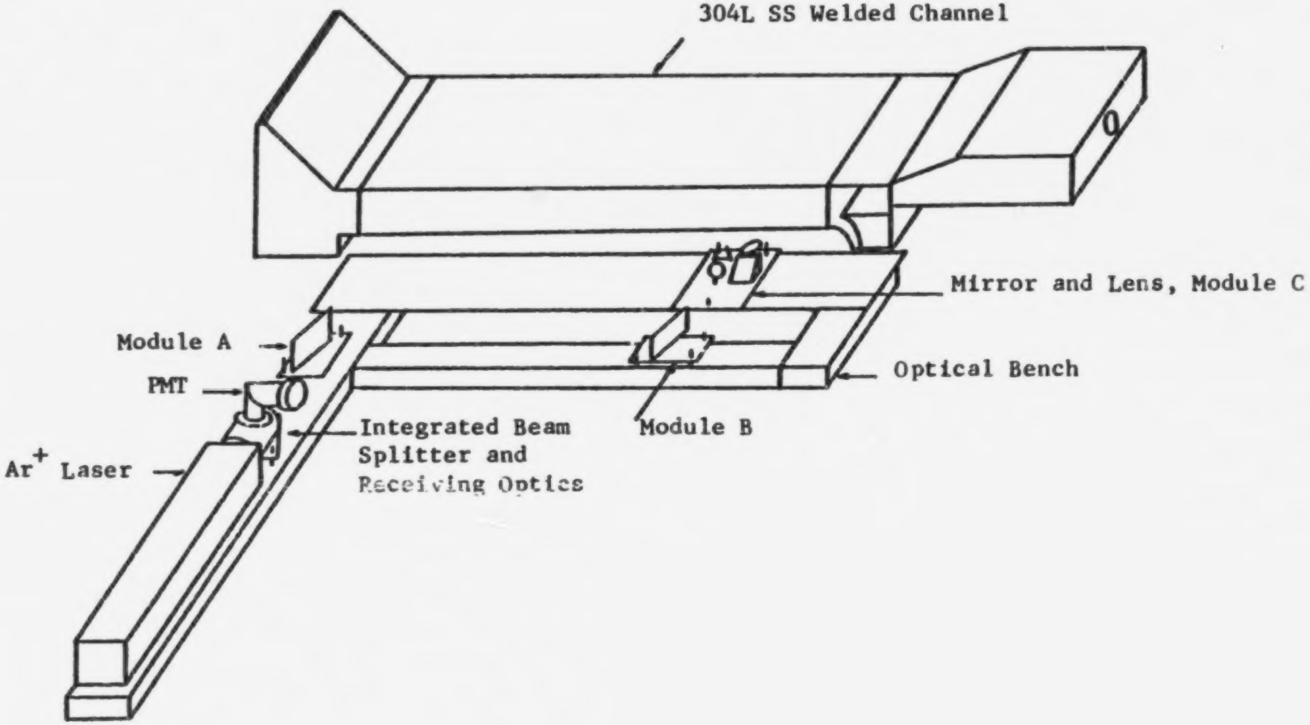
304L SS Welded Channel
Mirror and Lens, Module C
Module A
Optical Bench
PMT
Integrated Beam Splitter and Receiving Optics
Module B
Ar^+ Laser

Figure 3.3 Laser Anemometer and Optical Bench

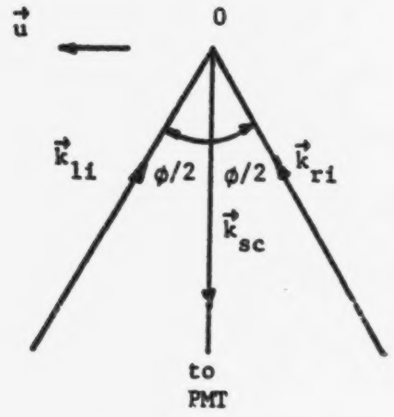
$\vec{u}$
0
$\vec{k}_{li}$
$\phi/2$
$\phi/2$
$\vec{k}_{ri}$
$\vec{k}_{sc}$
to
PMT

Figure 3.4 Incident and Scattered Propagation Vectors

BEST DOCUMENT AVAILABLE

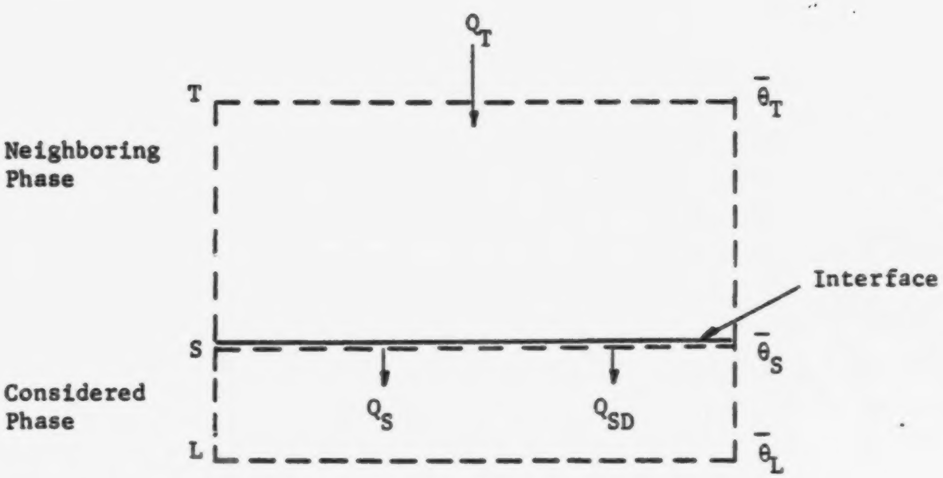
Q_T
T
$\bar{\theta}_T$
Neighboring Phase
Interface
S
$\bar{\theta}_S$
Considered Phase
Q_S
Q_{SD}
L
$\bar{\theta}_L$

Figure 4.1 Illustration of T, S, and L States with Fluxes Indicated

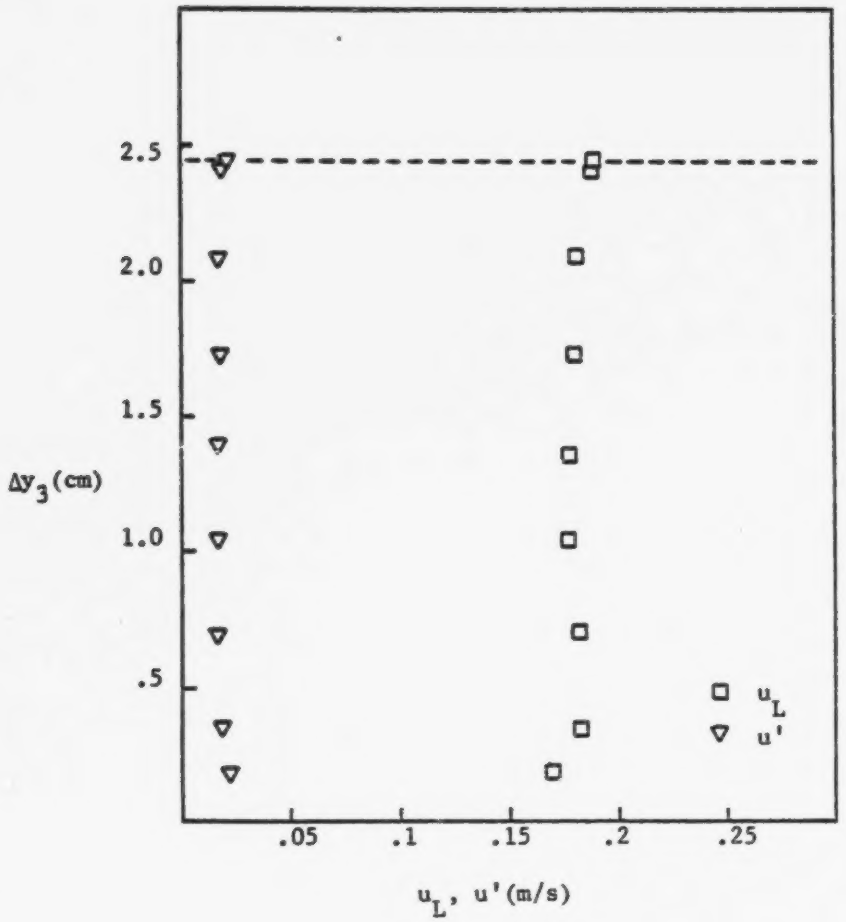

Figure 5.1 Liquid Layer Velocity Profile, w_L = 1.3 kg/s, w_g = 0, x = .157m. Dotted Line is Interface Location

BEST DOCUMENT AVAILABLE

BEST DOCUMENT AVAILABLE

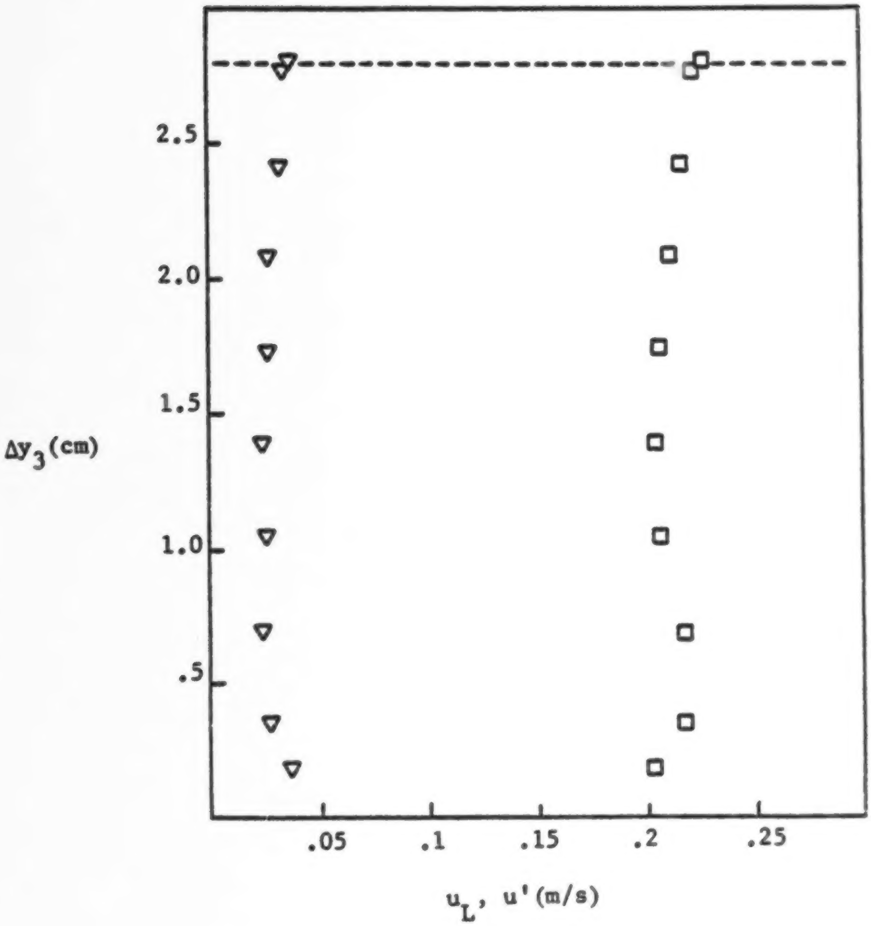

Figure 5.2 Liquid Layer Velocity Profile, $w_L = 1.8$ kg/s, $w_g = 0$, $x = .157$m

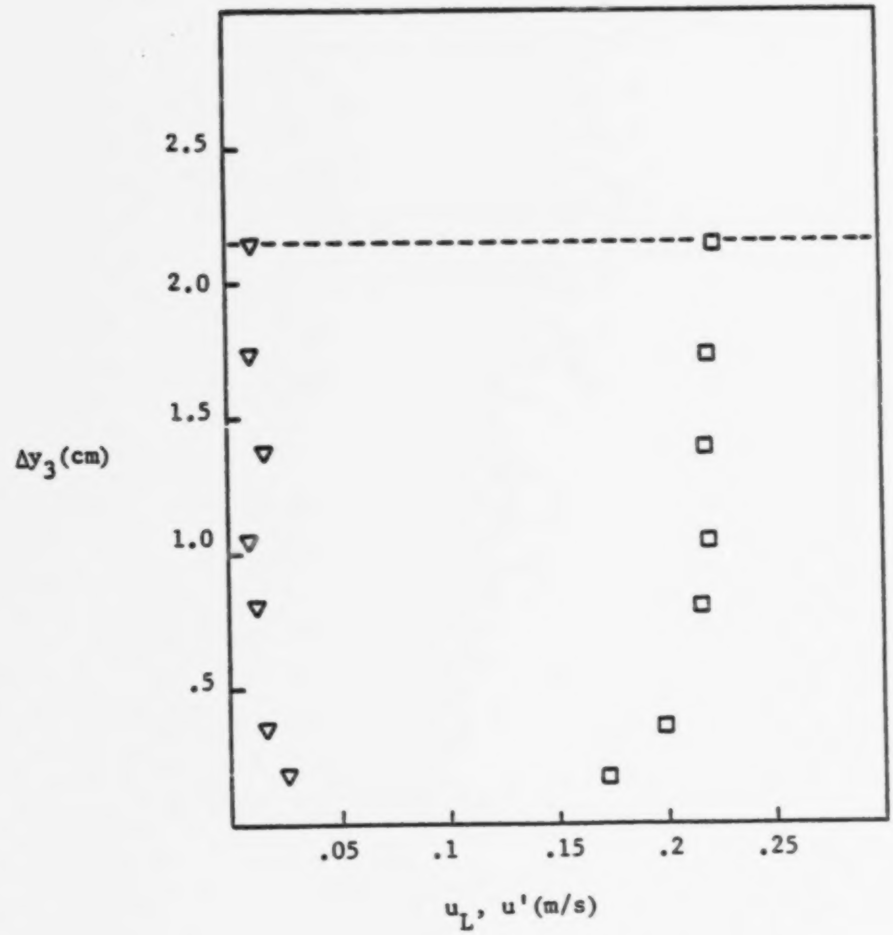

Figure 5.3 Liquid Layer Velocity Profile, w_L = 1.3 kg/s, w_g = 0, x = .586m

BEST DOCUMENT AVAILABLE

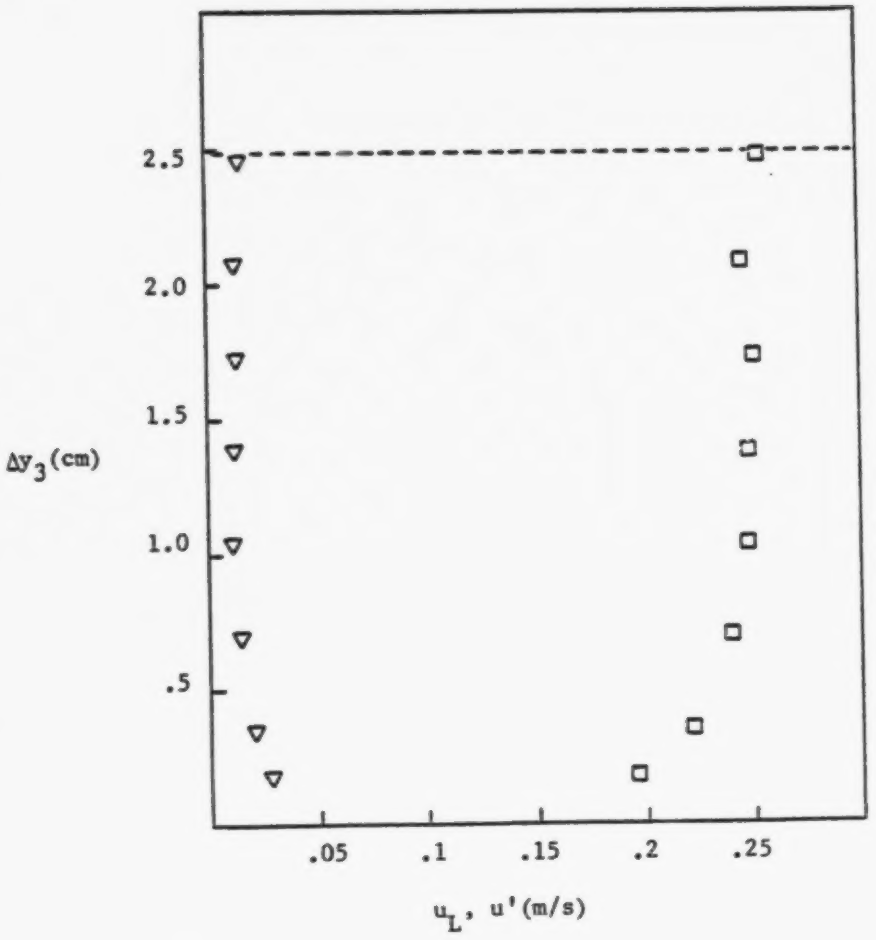

Figure 5.4 Liquid Layer Velocity Profile, w_L = 1.8 kg/s, w_g = 0, x = .586m

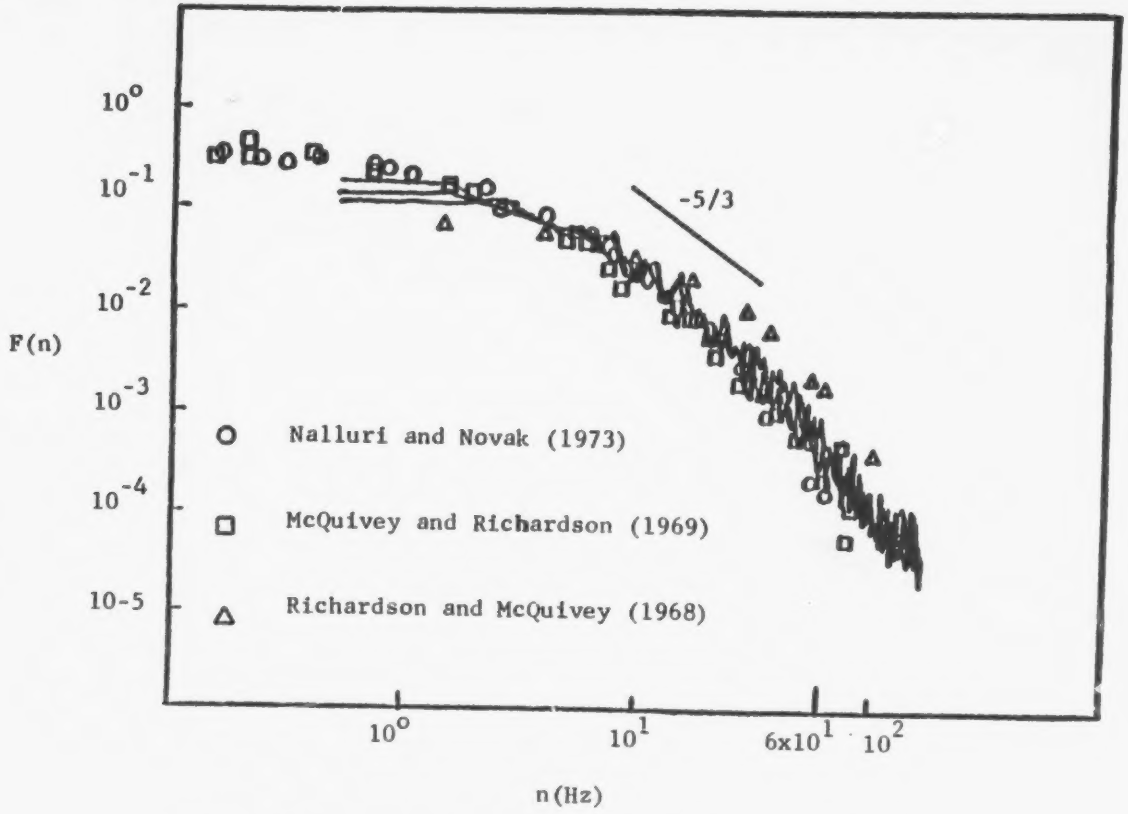

Figure 5.5 Energy Spectra Taken at the Interface for $w_L = 1.1$ kg/s, x ≈ .157m

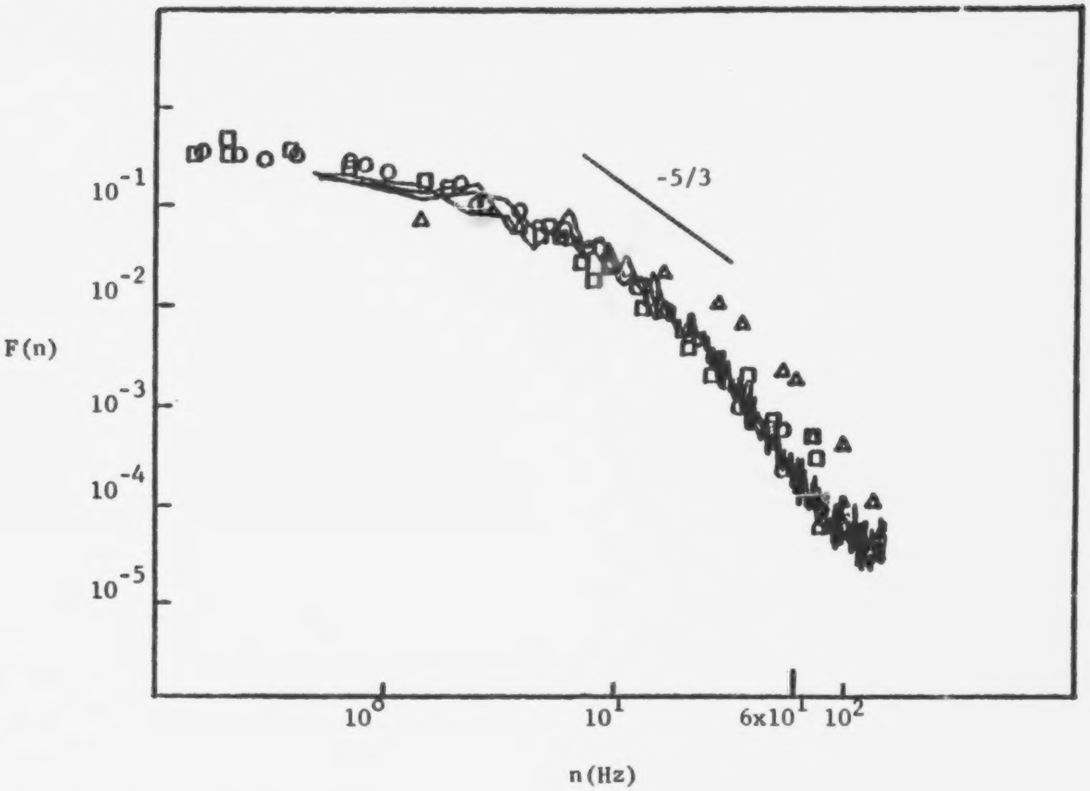

Figure 5.6 Energy Spectra Teken at the Interface for w_L= 1.8 kg/s, x = .157

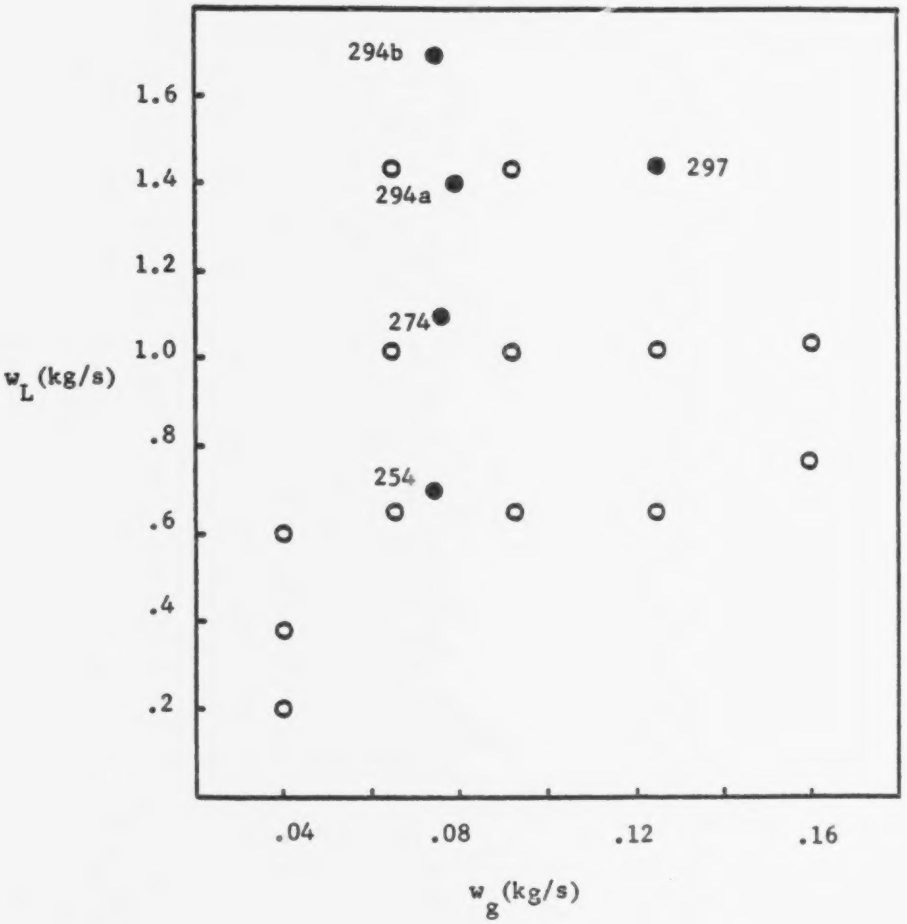

Figure 5.7 Data Matrix. Darkened, Numbered Symbols Indicate Conditions at which LDA Measurements Were Made

BEST DOCUMENT AVAILABLE

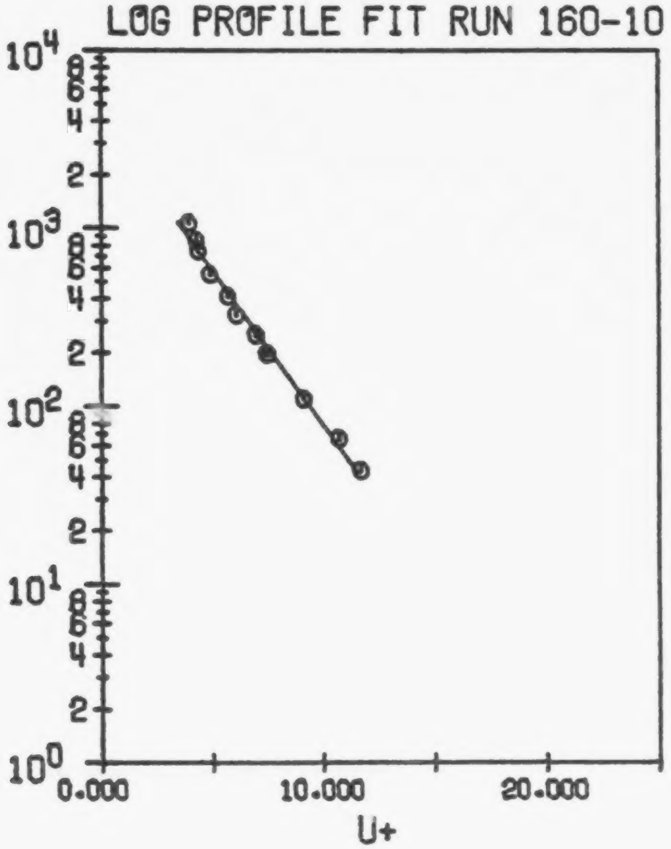

Figure 5.8a Mean Liquid Velocity for Steam Run 294a, x = .157m

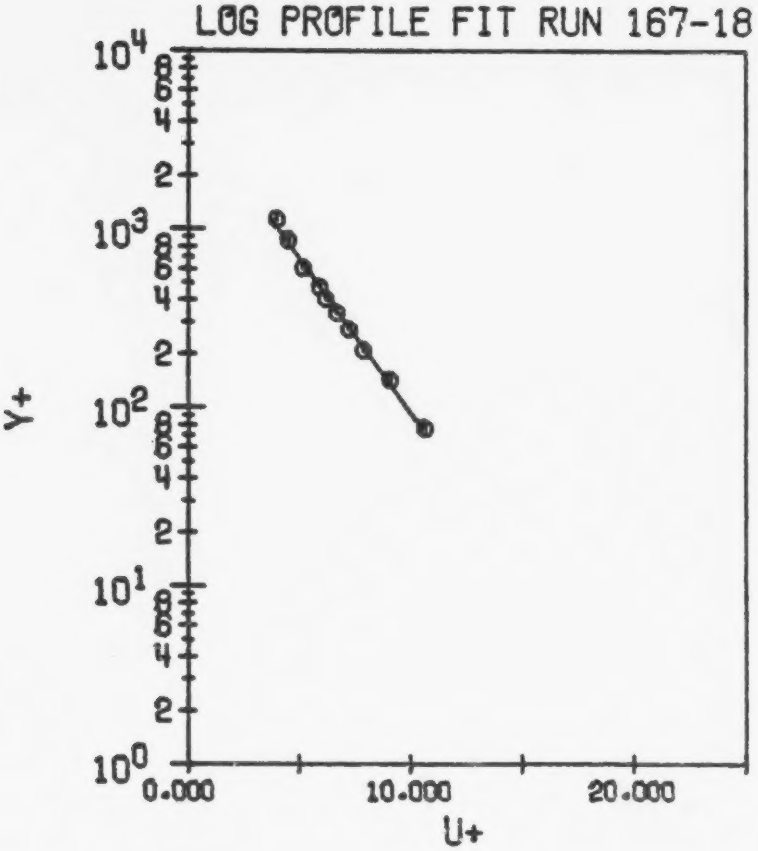

Figure 5.8b Mean Liquid Velocity for Steam Run 294a, x = .306m

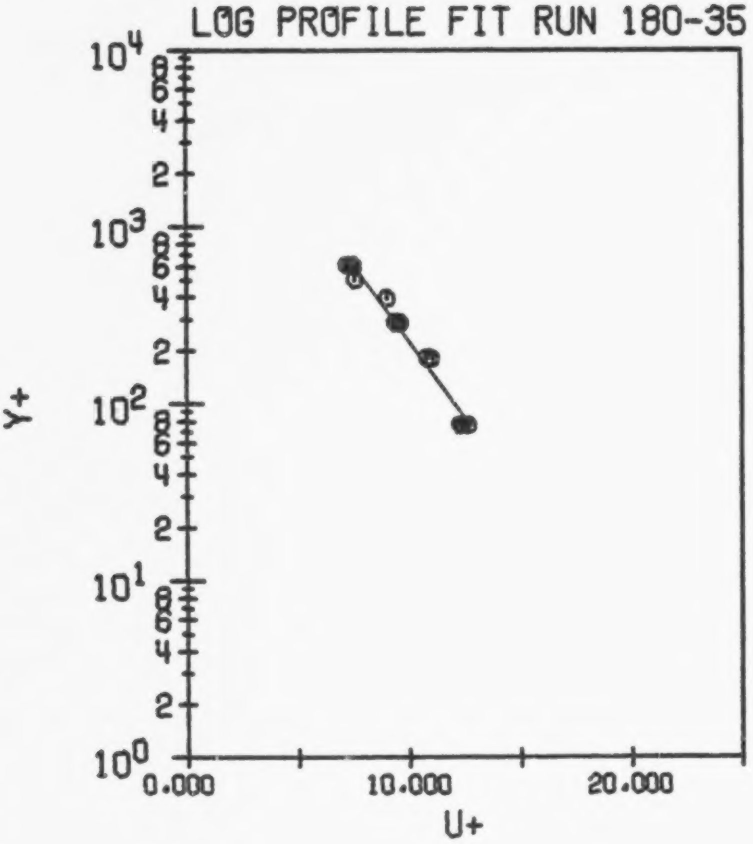

Figure 5.8c Mean Liquid Velocity for Steam Run 294a, x = .586

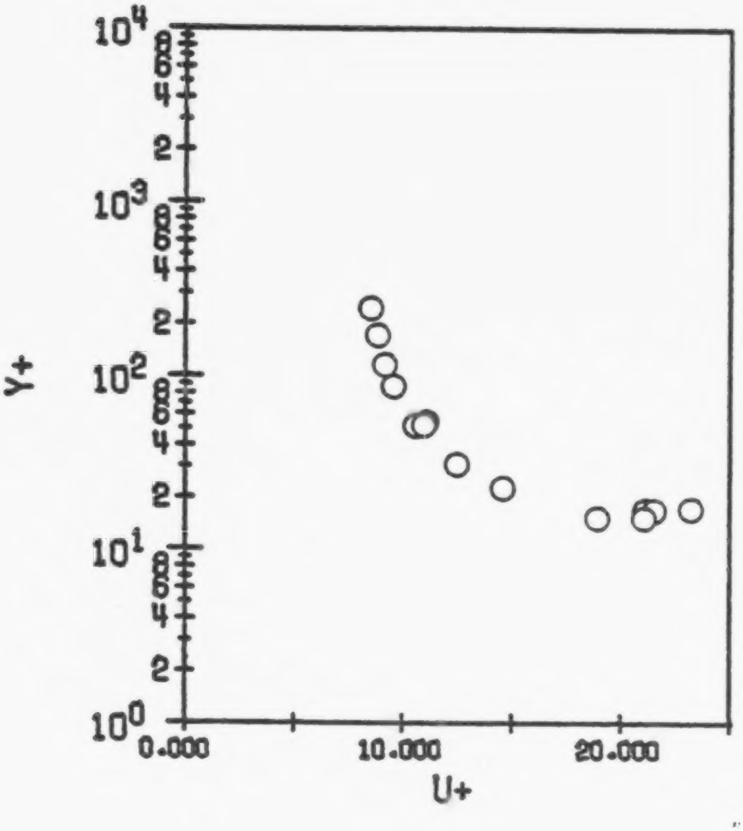

Figure 5.9a Mean Liquid Velocity for Steam Run 254, $x = .157\text{m}$. Note $u_* = u_{*FB}$ here.

BEST DOCUMENT AVAILABLE

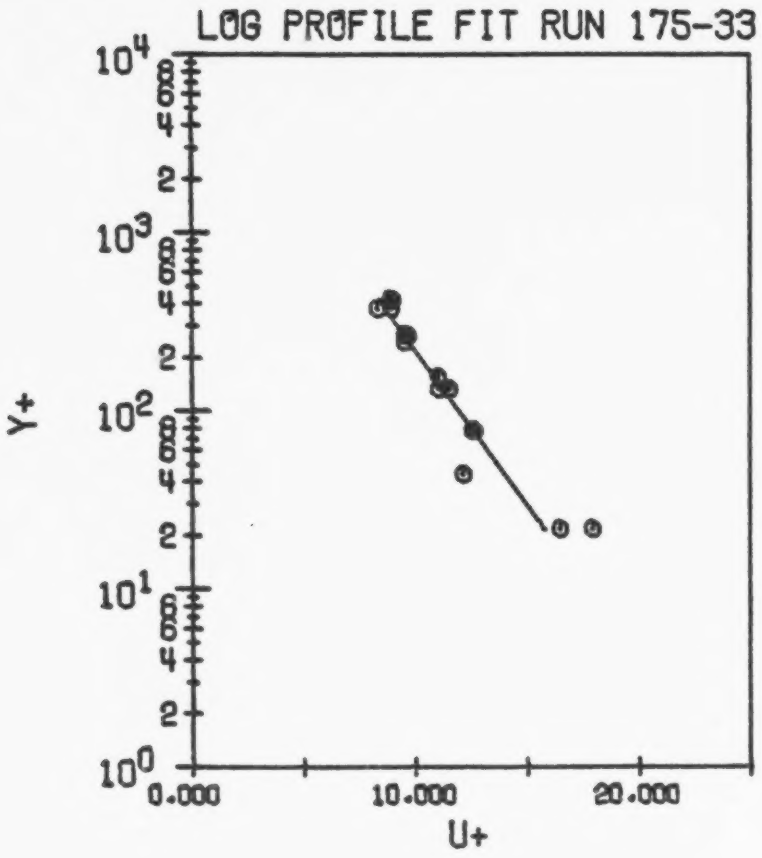

Figure 5.9b Mean Liquid Velocity for Steam Run 254,
x = .586m

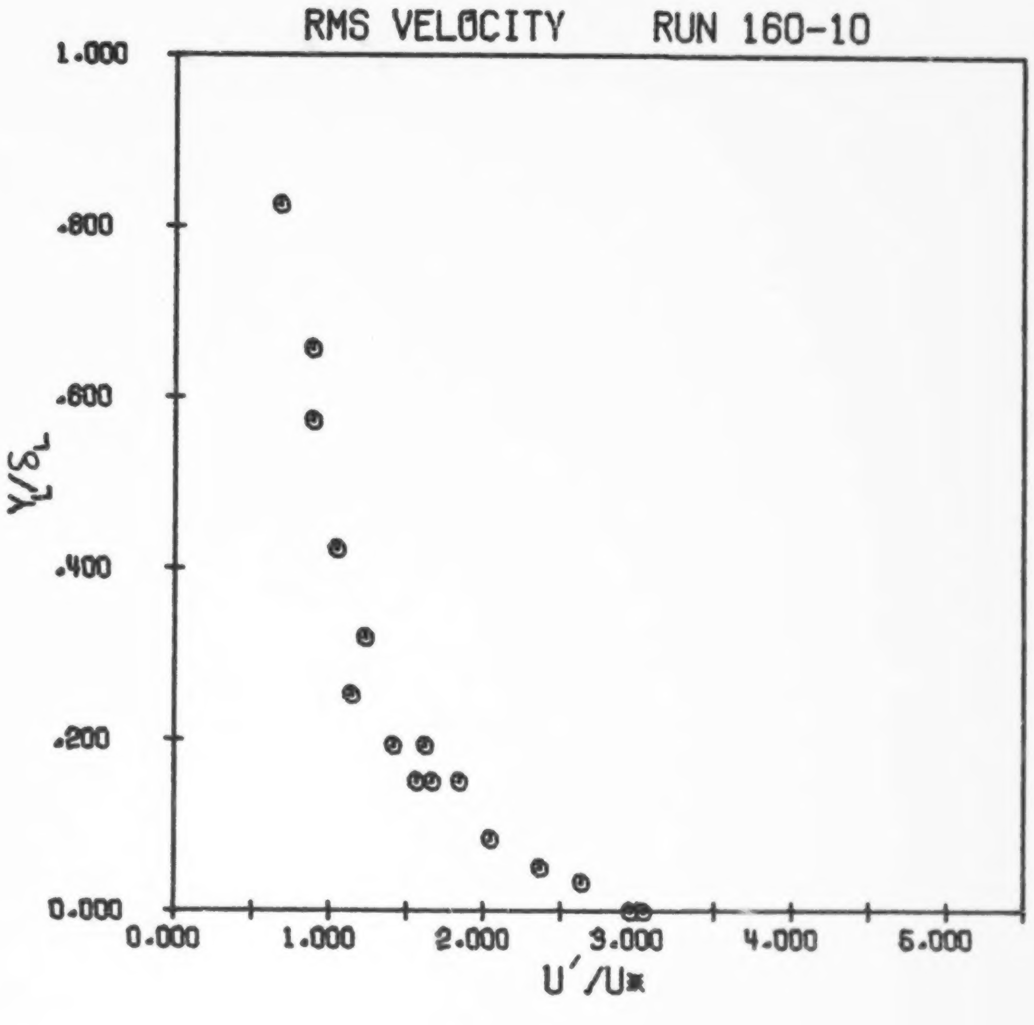

Figure 5.10a Rms Liquid Fluctuation for Steam Run 294a, x = .157m

BEST DOCUMENT AVAILABLE

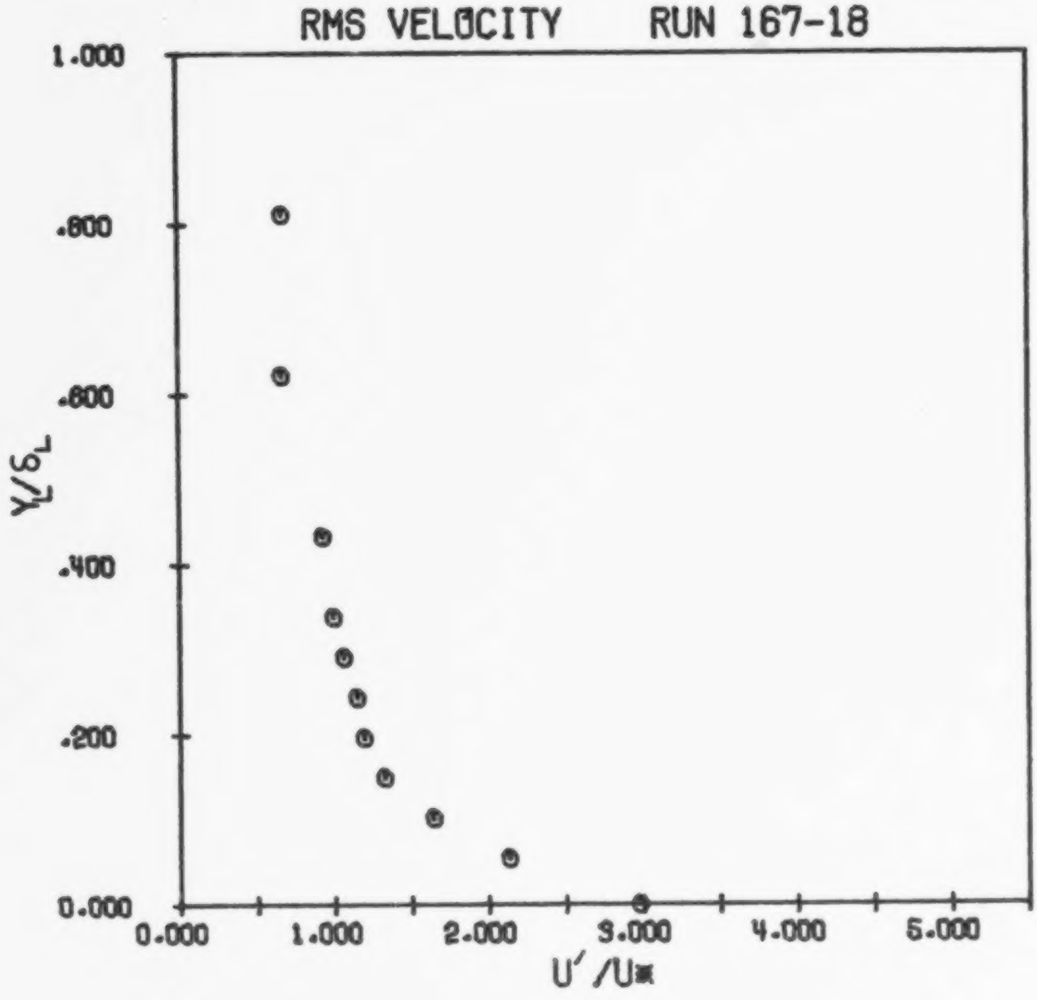

Figure 5.10b Rms Liquid Fluctuation for Steam Run 294a,
x = .306m

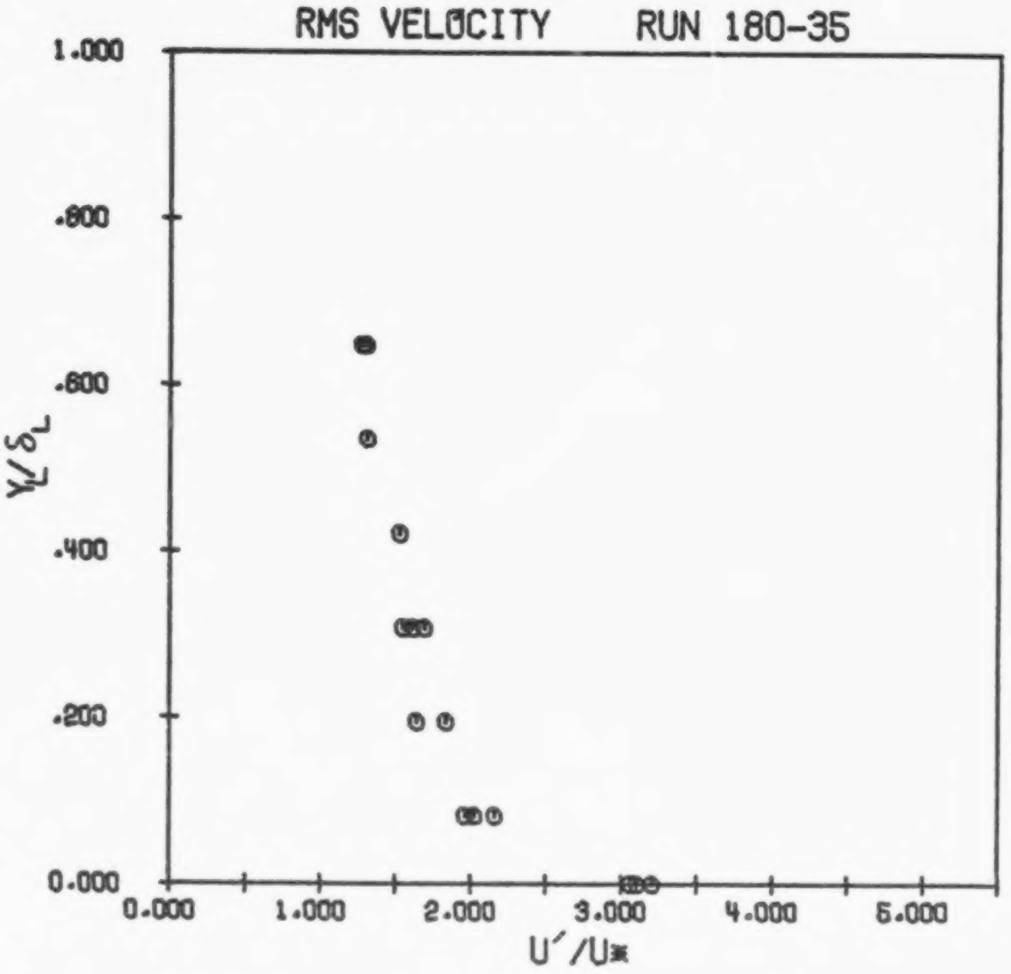

Figure 5.10c Rms Liquid Fluctuation for Steam Run 294a, x = .586m

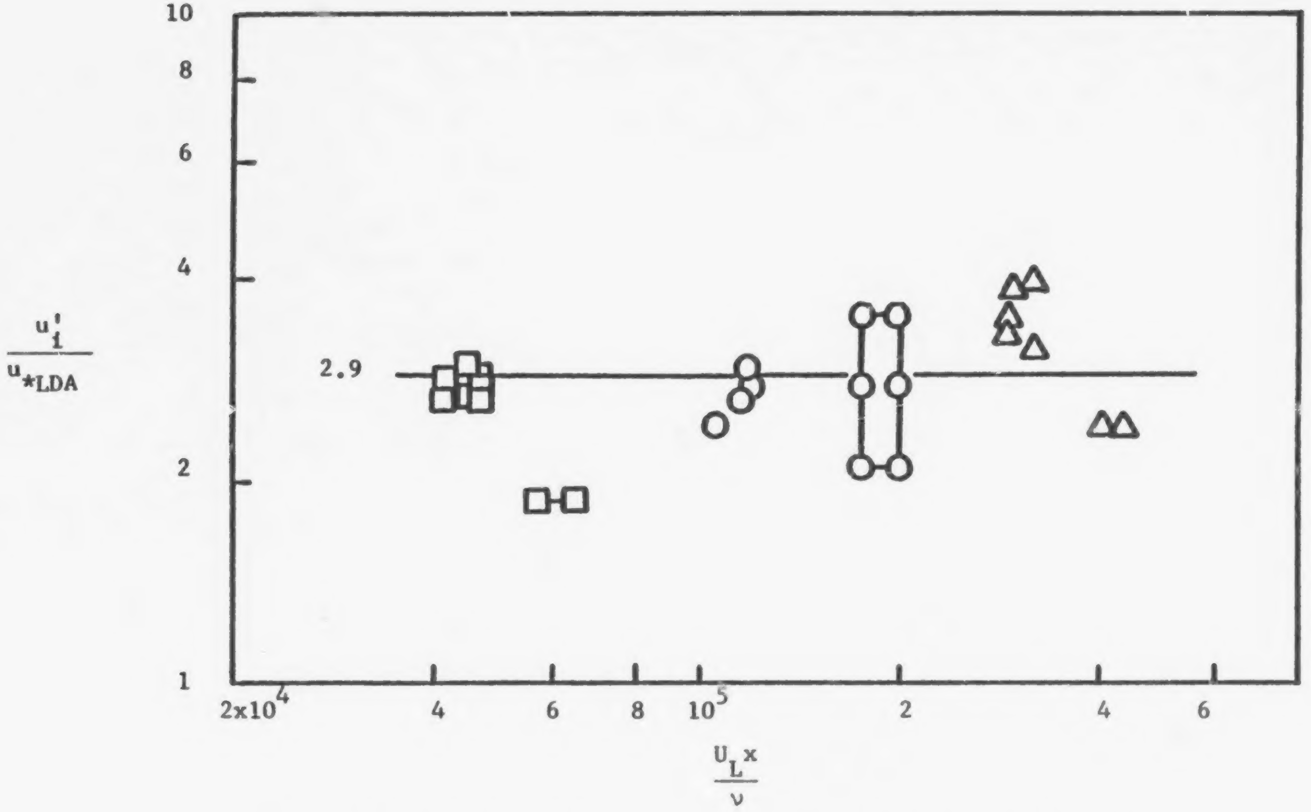

Figure 5.11 Ratio of Streamwise Interface Fluctuation to u_{*LDA}. Symbols Given in Table 5-4

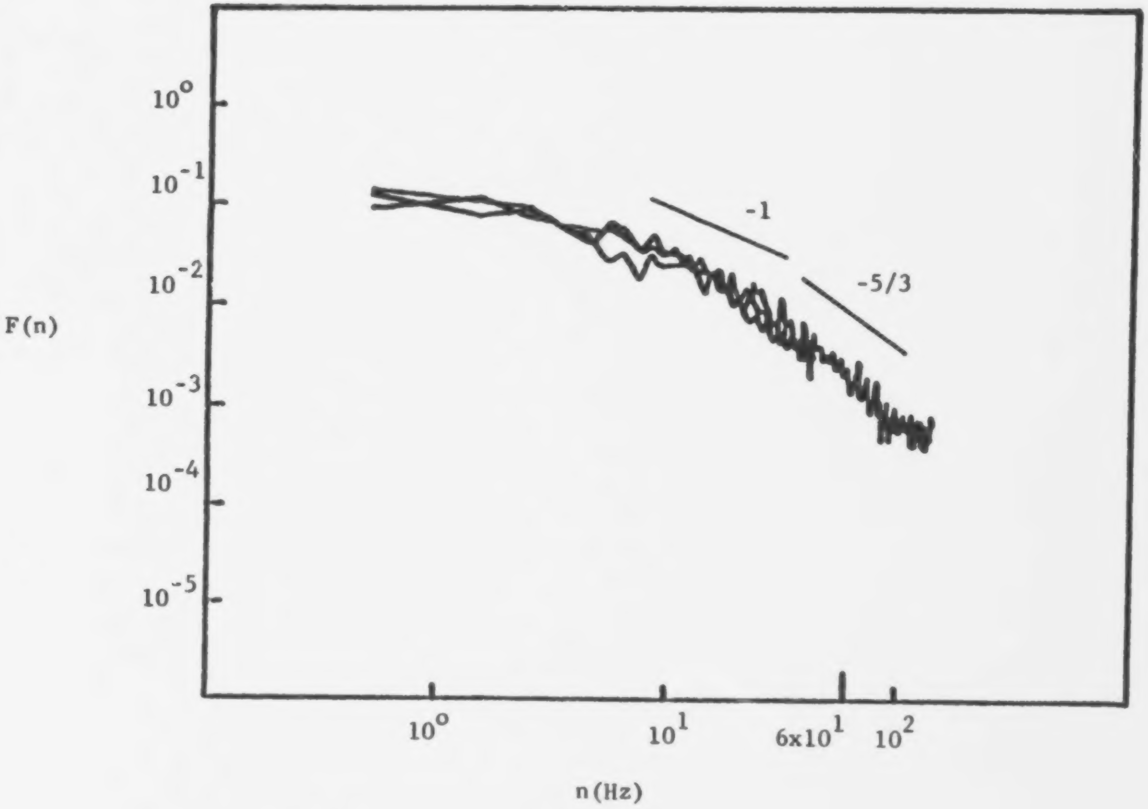

Figure 5.12a Liquid Fluctuation Spectra for Steam Run 254, $x = .586\text{m}$. $y_L = .3$ and 4mm

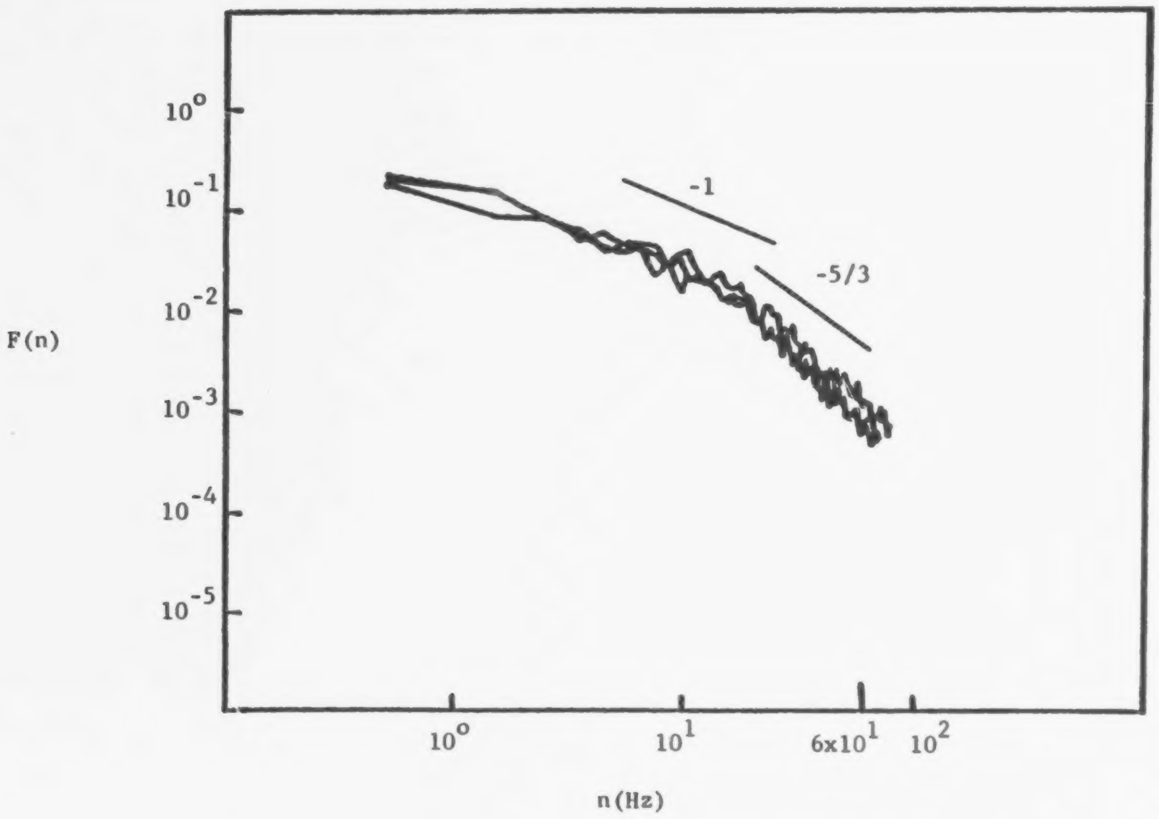

Figure 5.12b Liquid Fluctuation Spectra for Steam Run 294a, $x = .586m$, y_L is 3 to 4mm

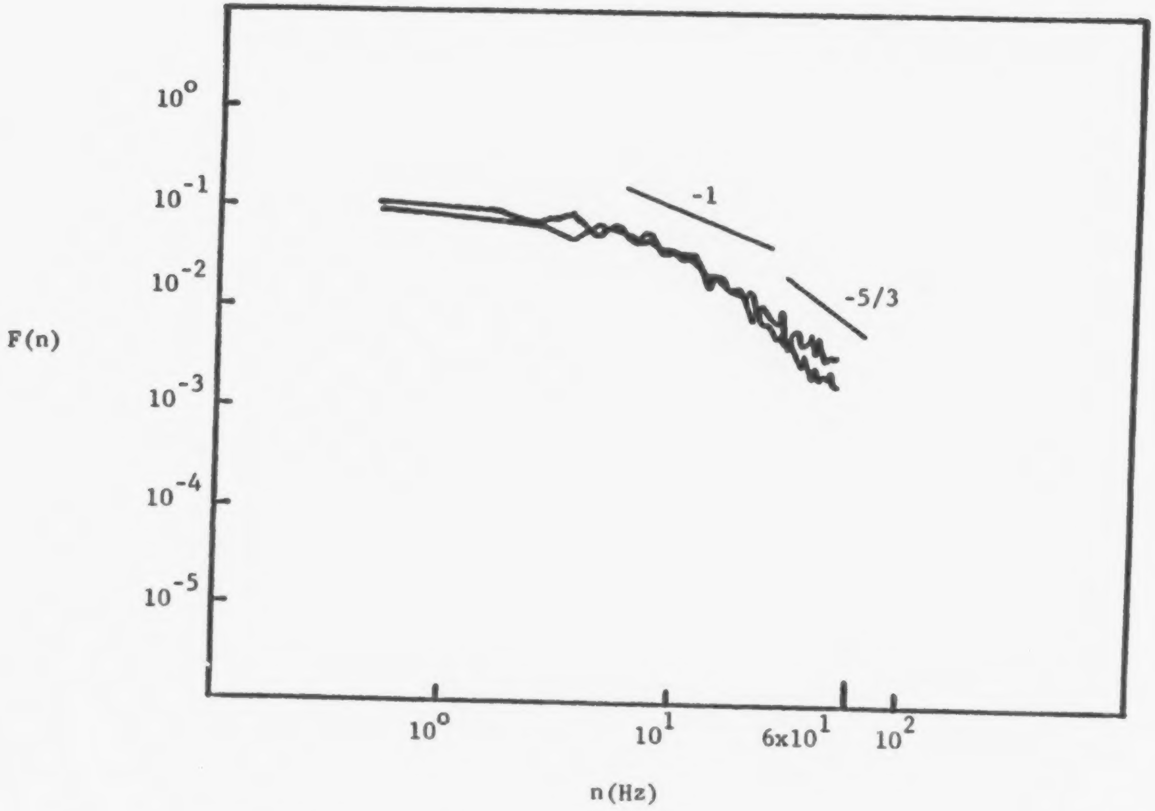

Figure 5.12c Liquid Fluctuation Spectra for Steam Run 297, $x = .586m$, $y_L = 0$ and 6mm

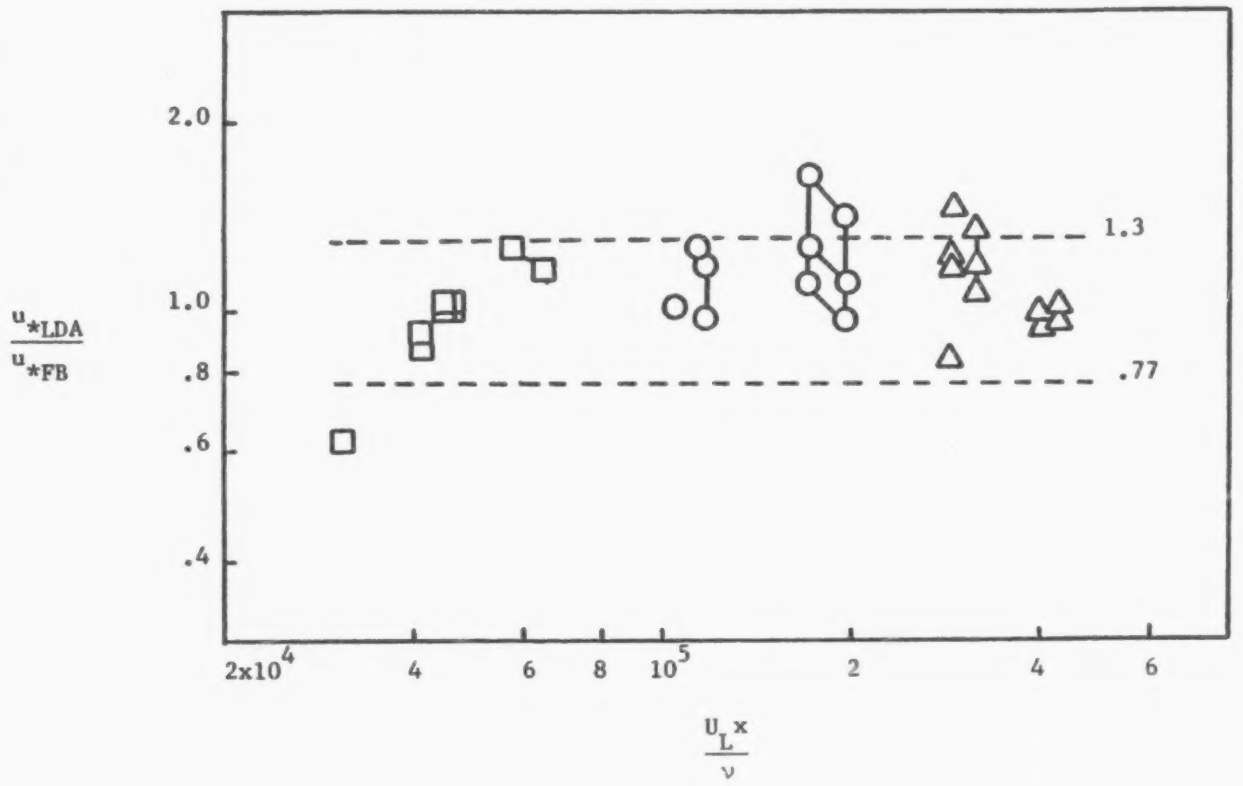

Figure 5.13 Ratio of Laser Anemometer Profile Fit u_{*LDA} to u_{*FB} Derived From Force Balance. Symbols Given in Table 5-4

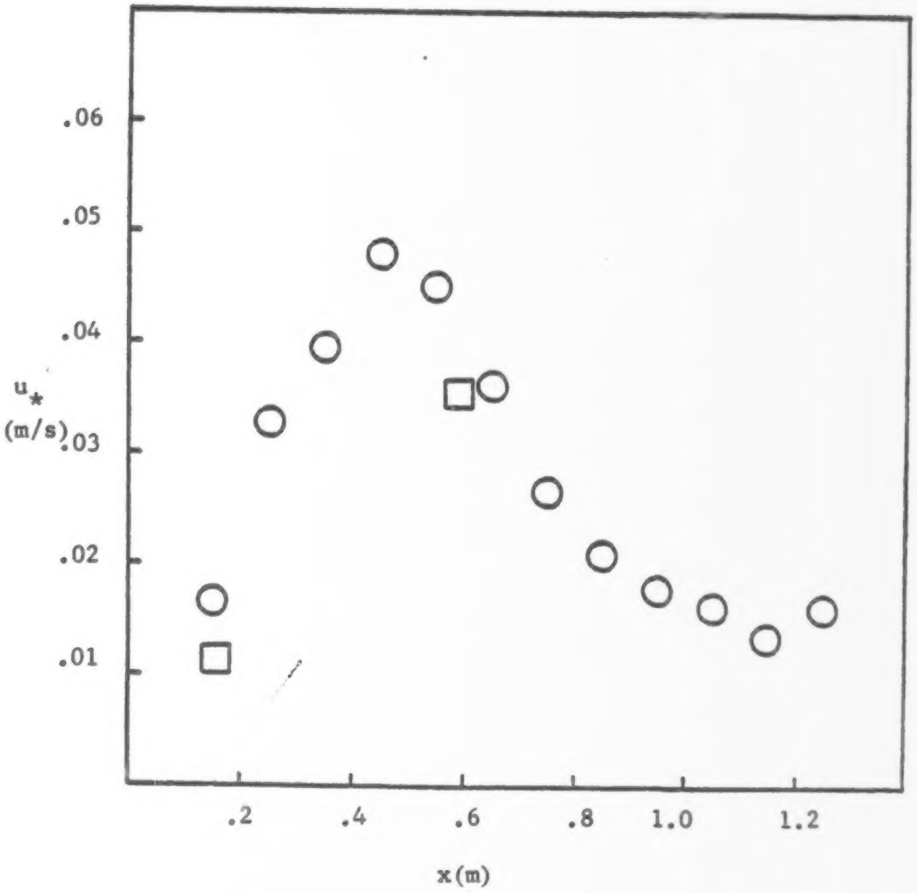

Figure 5.14a Streamwise Shear Velocity Profile Steam Run 254. Circles are u_{*FB} and Squares are u_{*LDA}

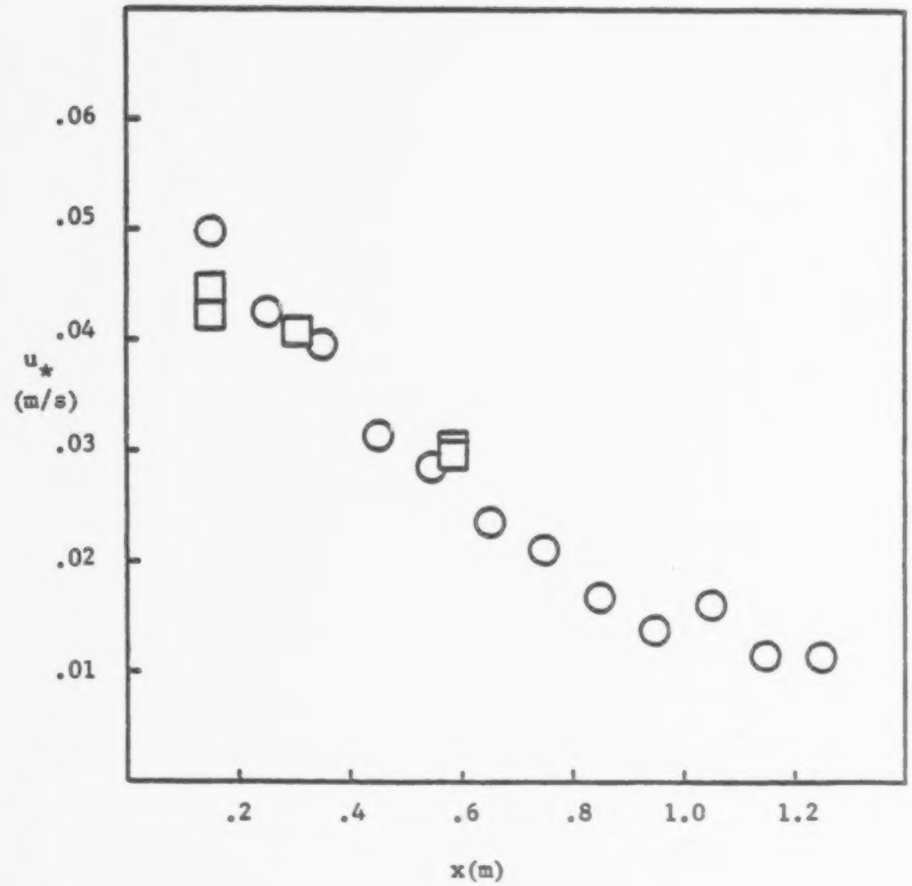

Figure 5.14b Streamwise Shear Velocity Profile Steam Run 274

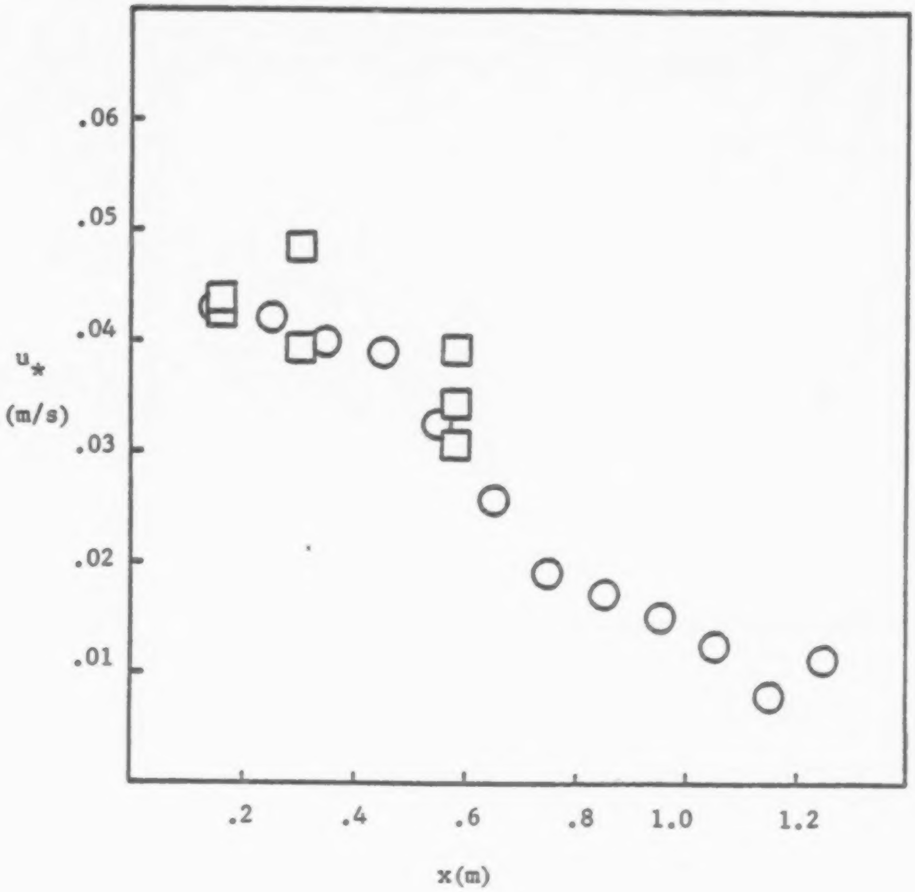

Figure 5.14c Streamwise Shear Velocity Profile Steam Run 294a

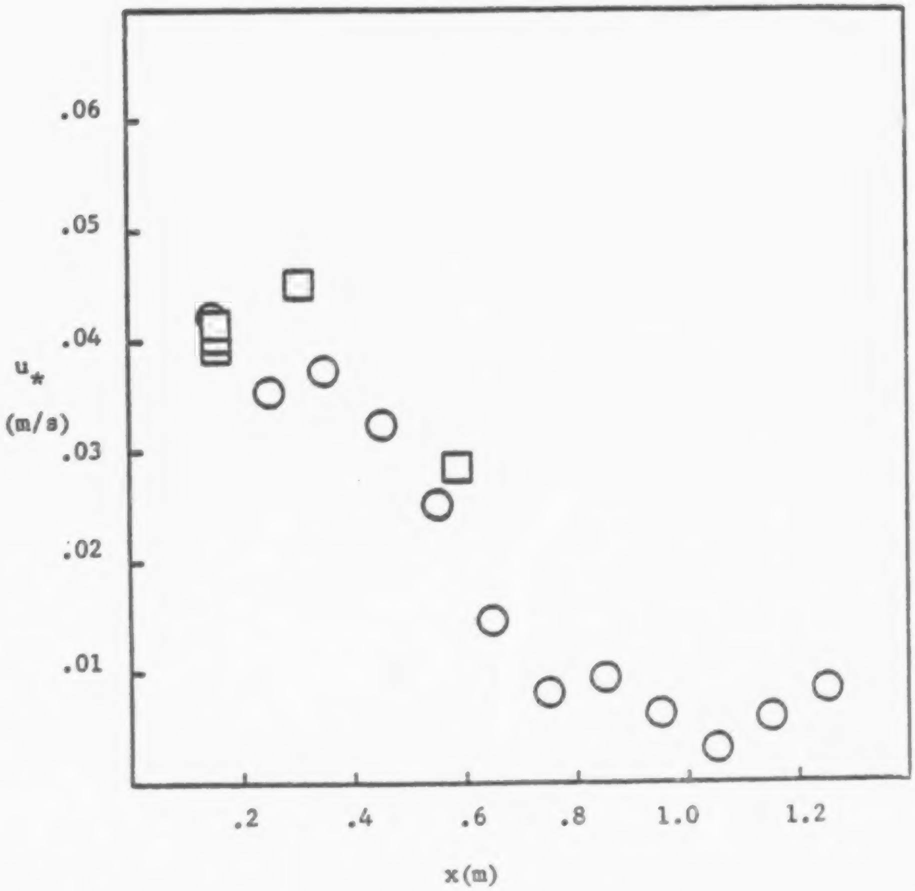

Figure 5.14d Streamwise Shear Velocity Profile Stream Run 294b

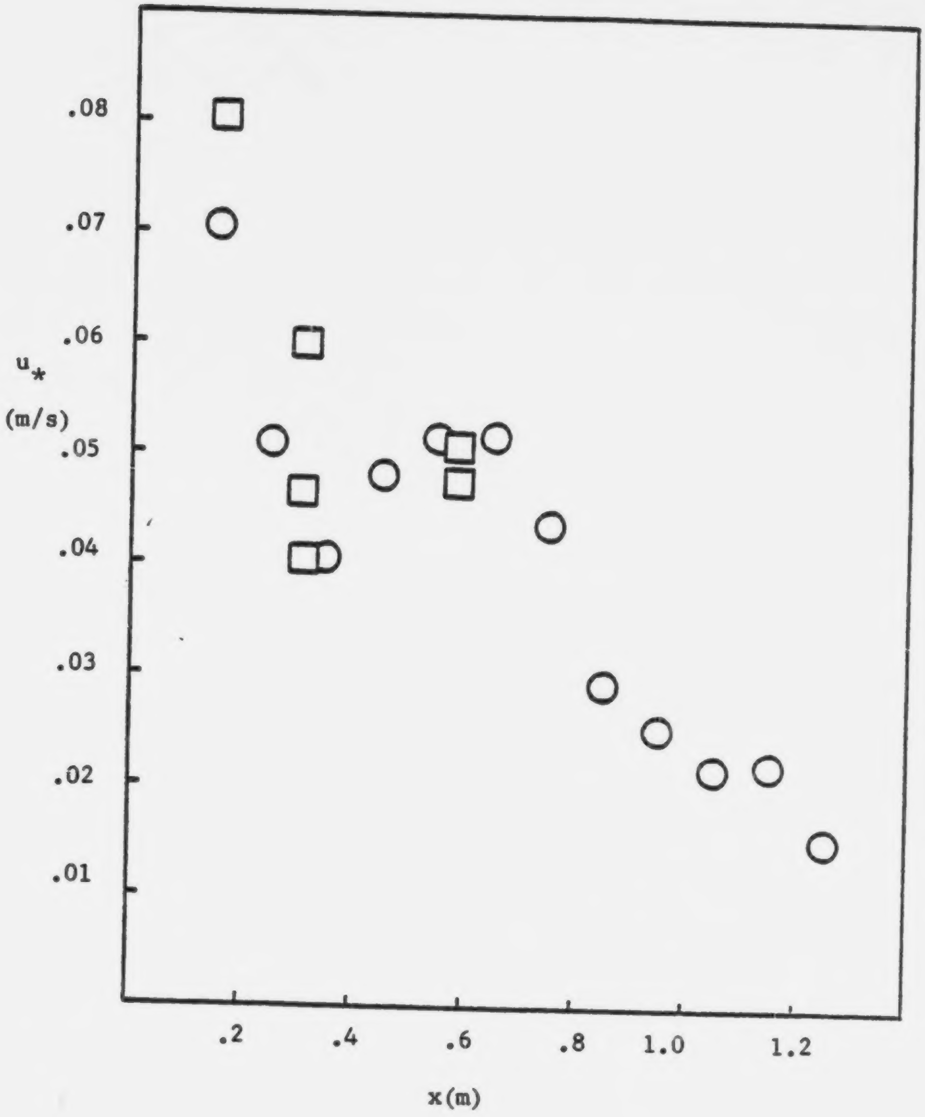

Figure 5.14e Streamwise Shear Velocity Profile Steam Run 297, File 92

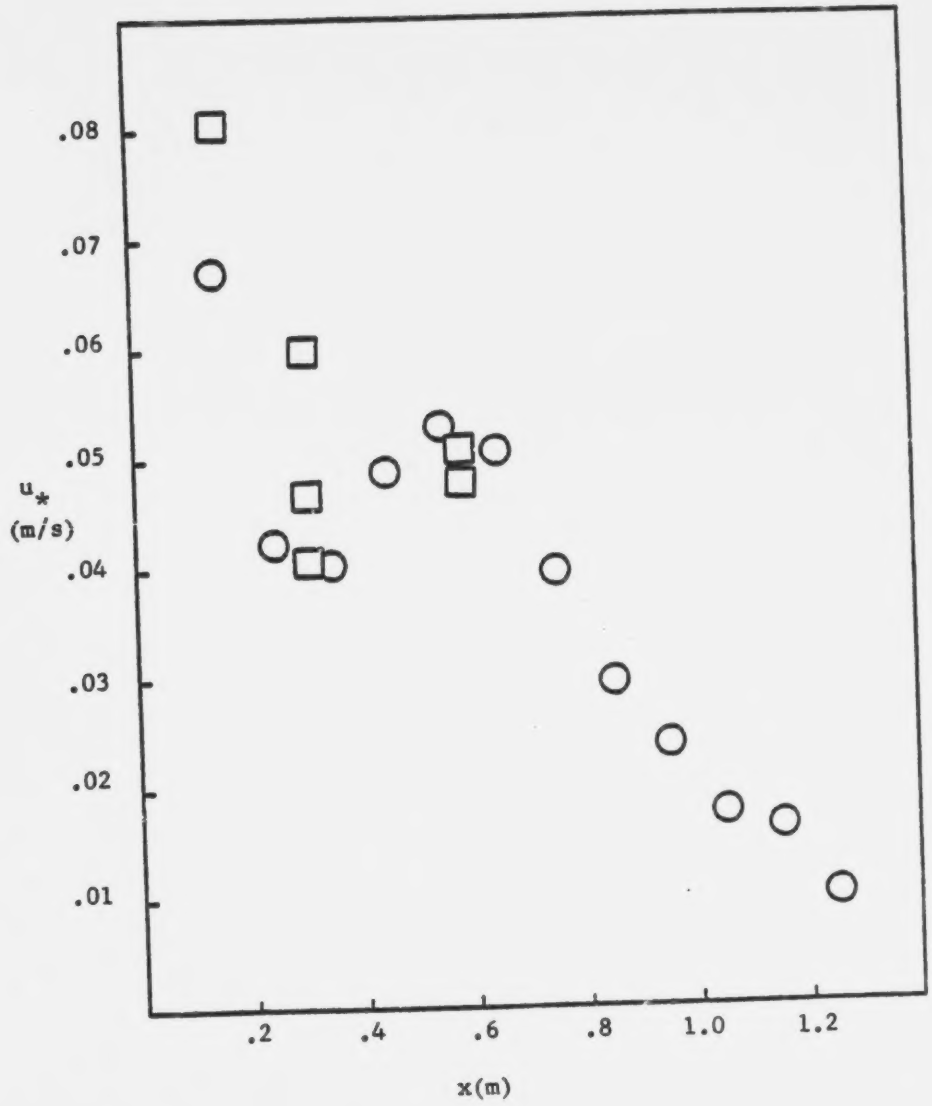

Figure 5.14f Streamwise Shear Velocity Profile Steam Run 297, File 93

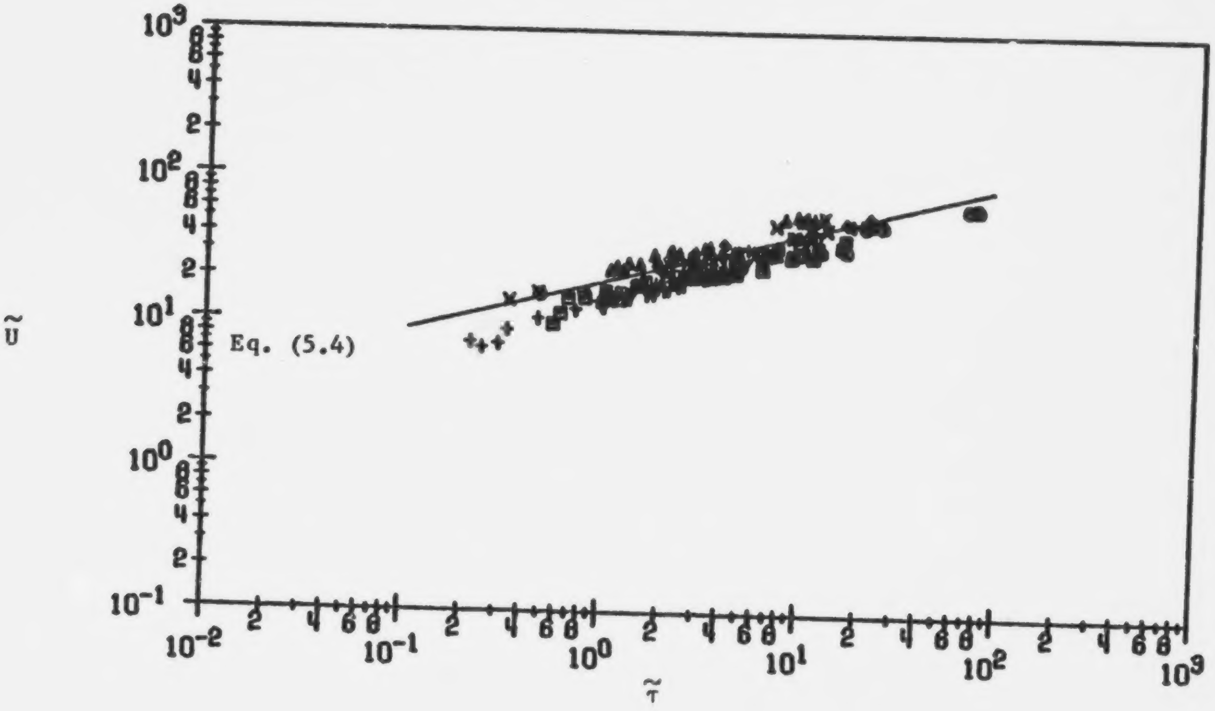

Figure 5.15 Plate's Correlation for Shear Stress

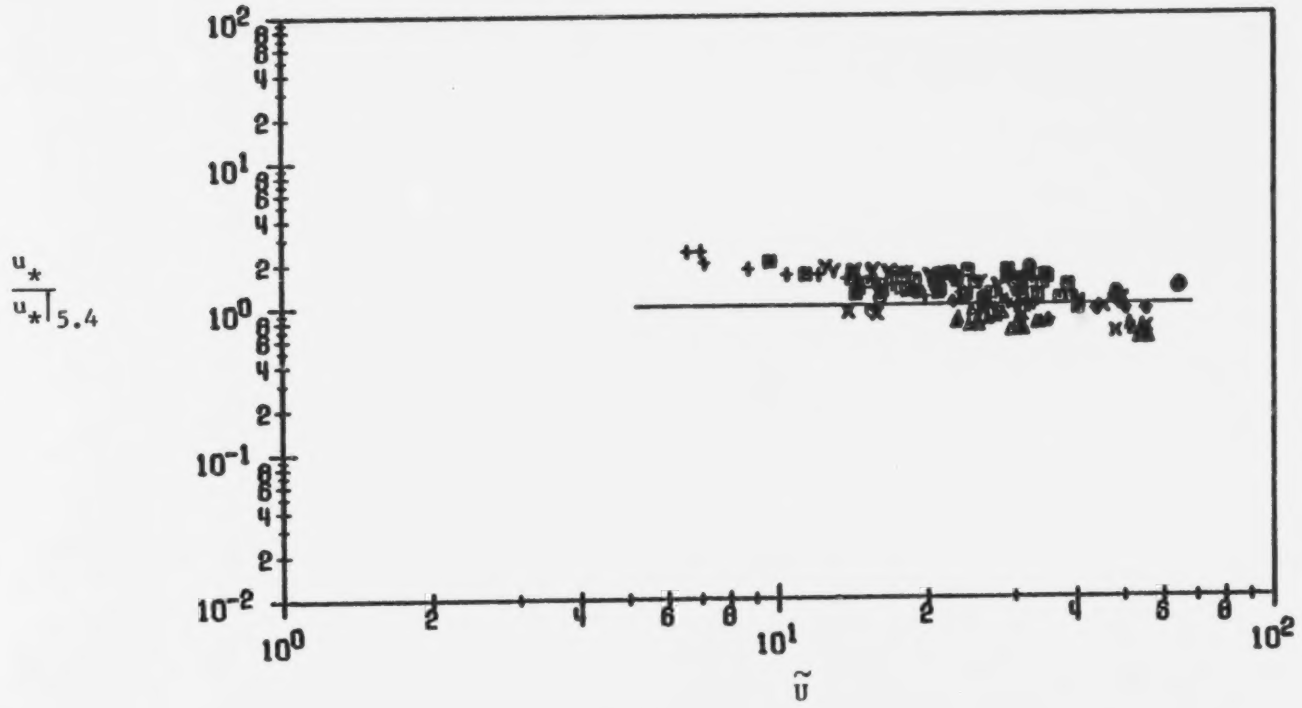

Figure 5.16 Ratio of Actual to Predicted Shear Velocities Using Plate's Correlation

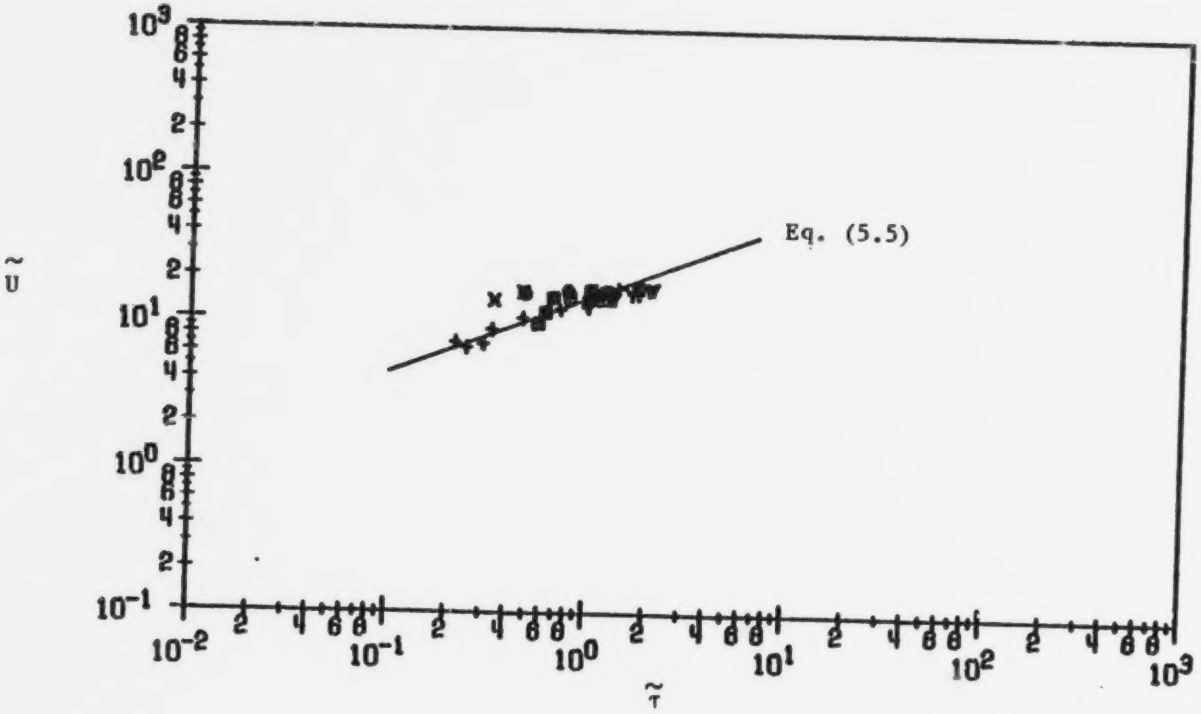

Figure 5.17 $\tilde{U}$ vs. $\tilde{\tau}$ for $\tilde{U} < 17.6$

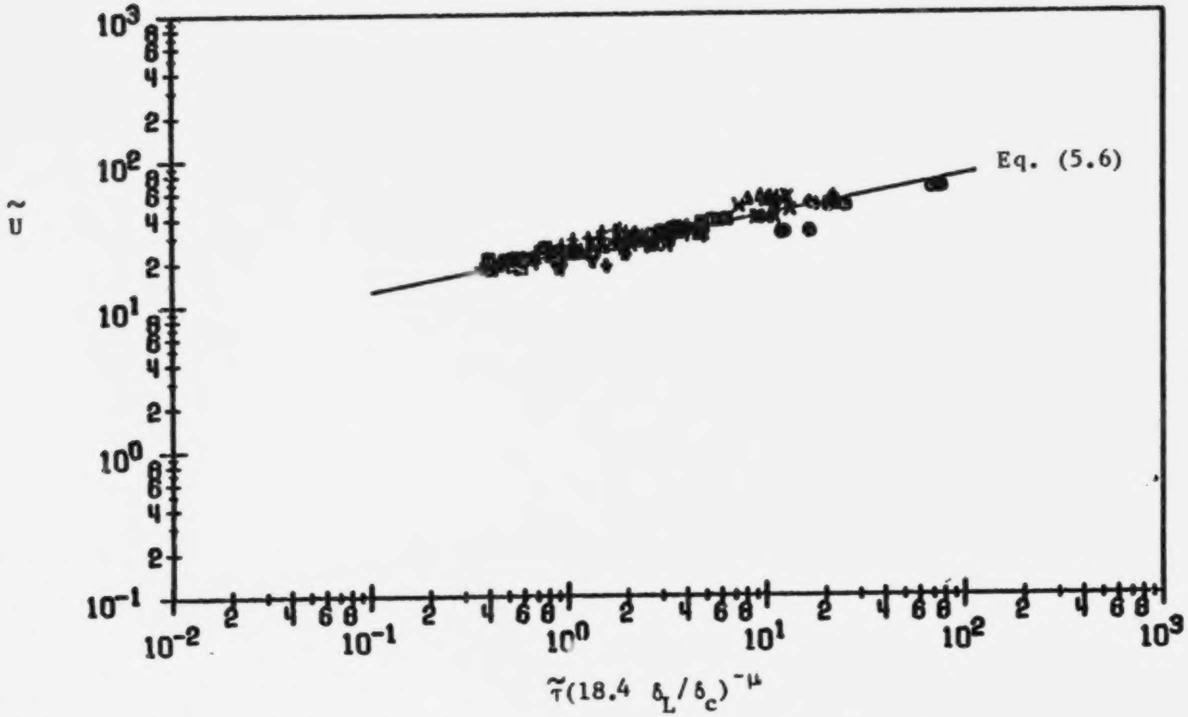

Figure 5.18 $\tilde{U}$ vs. $\tilde{\tau}(18.4 \frac{\delta_L}{\delta_c})^{-\mu}$ for $\tilde{U} \geq 17.6$

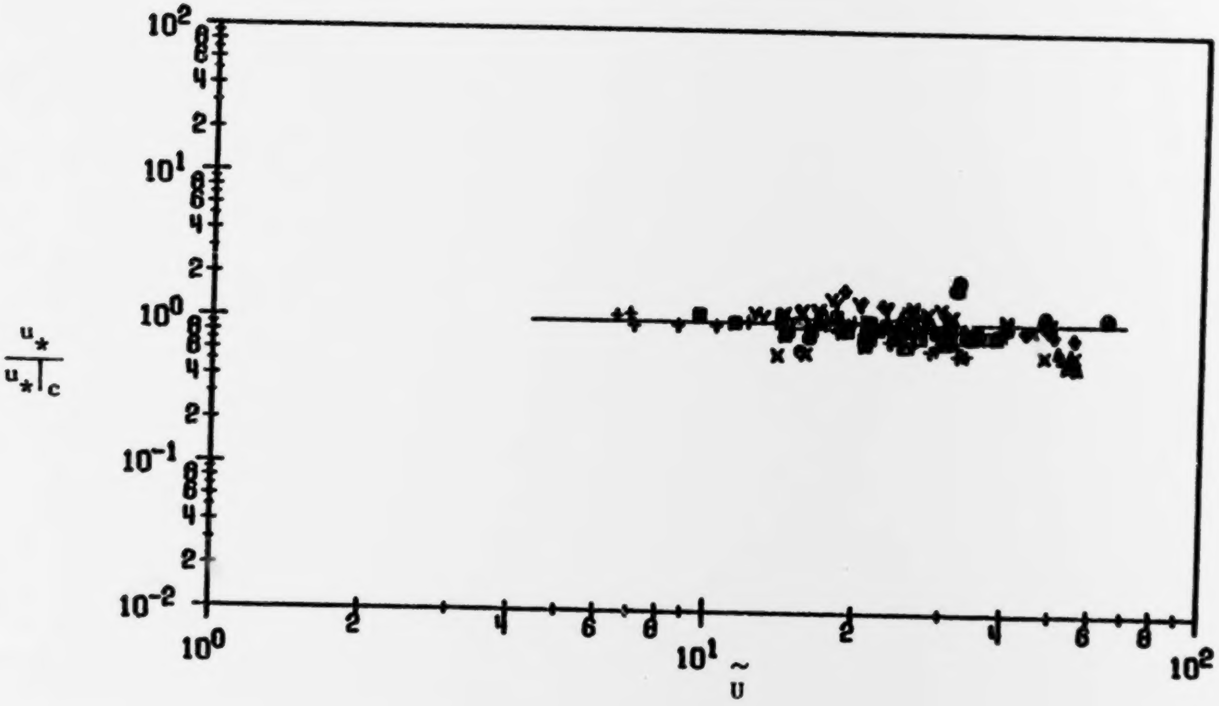

Figure 5.19 Ratio of Actual to Predicted Shear Velocities Using Eq. (5.5) and Eq. (5.6)

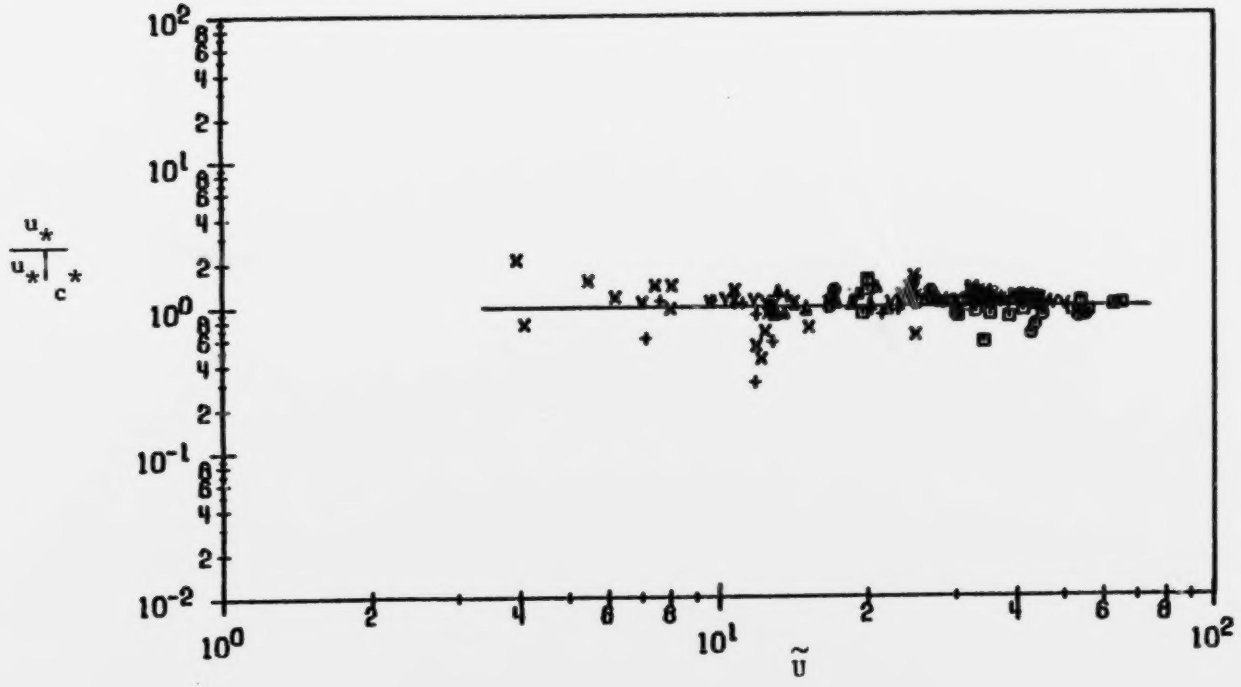

Figure 5.20 Ratio of Actual to Predicted Shear Velocities for Condensation Data Using Linehan's Model for τ^*

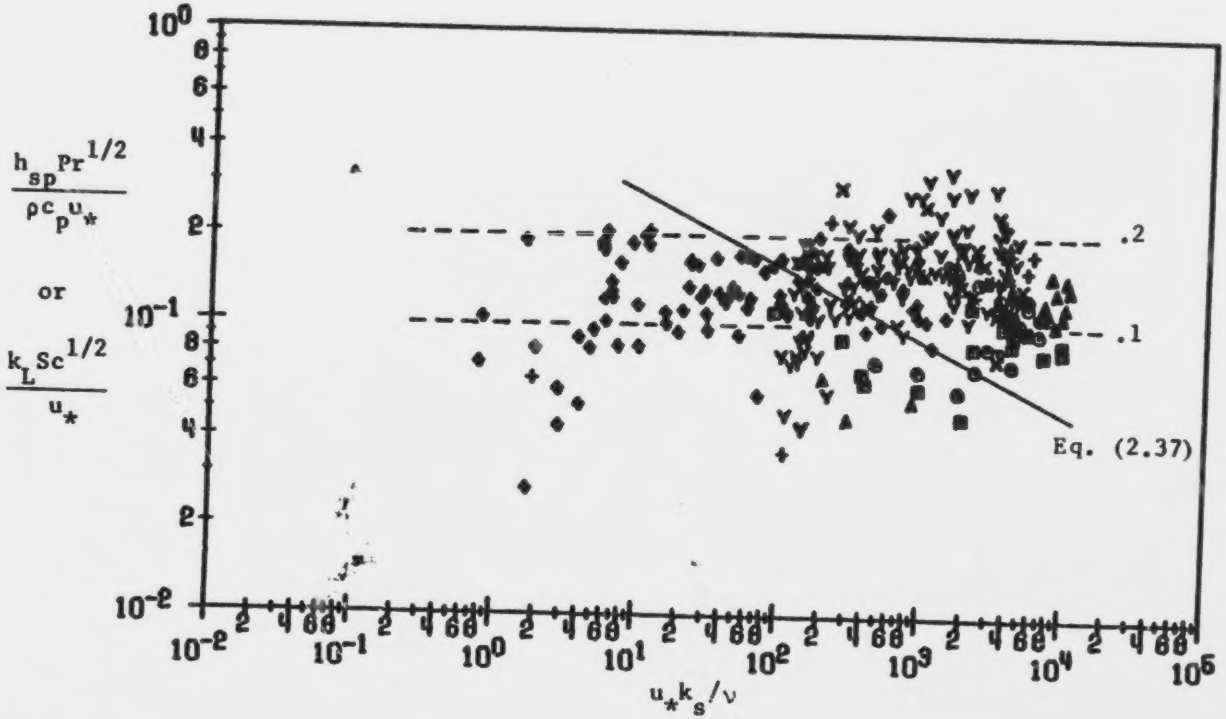

Figure 5.21 Asia et al.'s Correlation

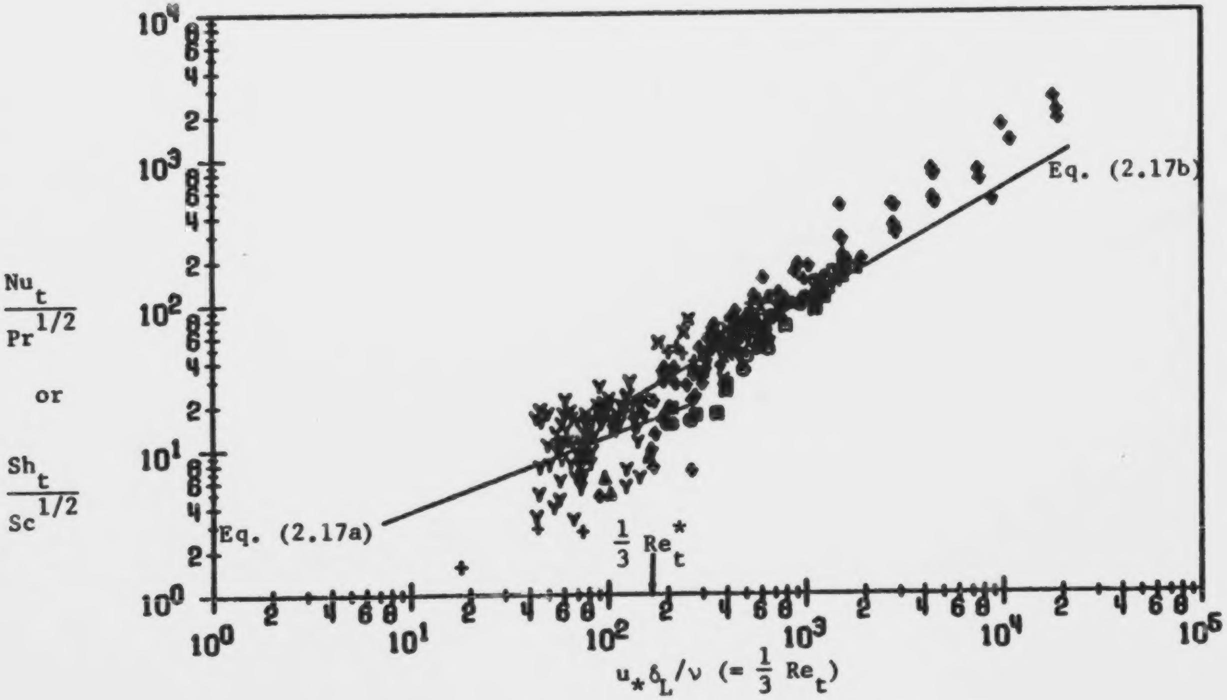

Figure 5.22 Theofanous et al.'s Correlation

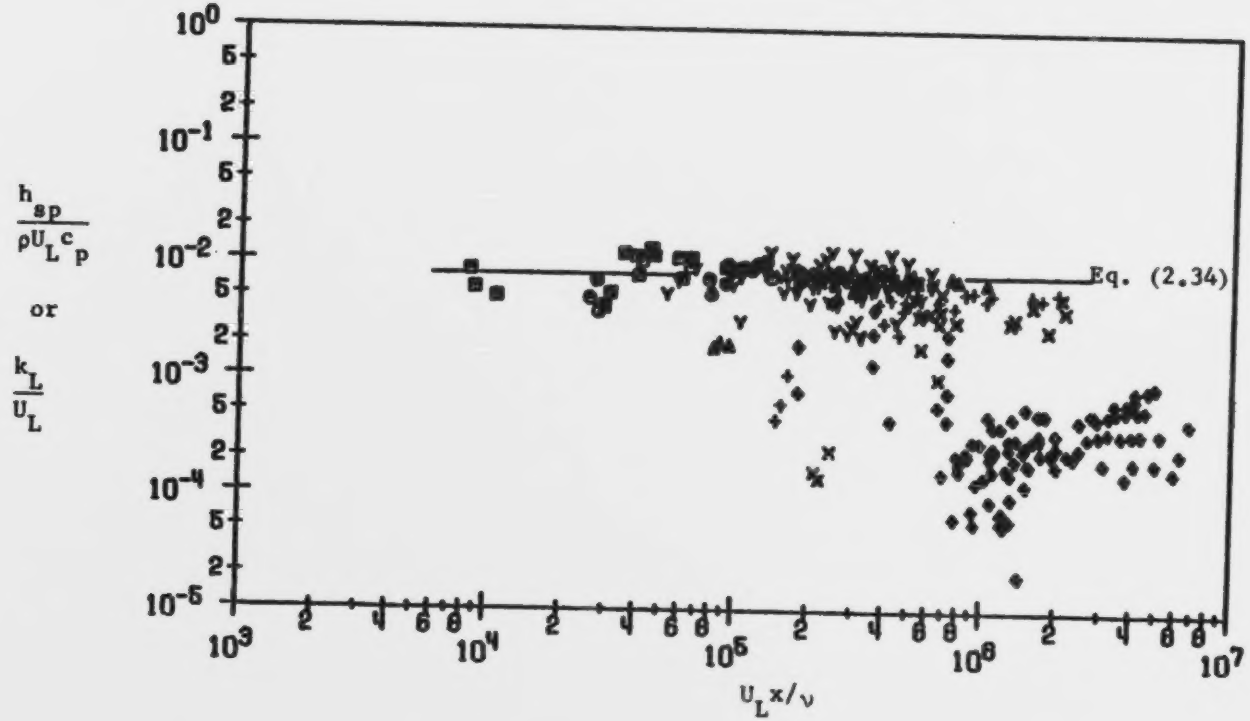

Figure 5.23 Linehan's Stanton Number Correlation

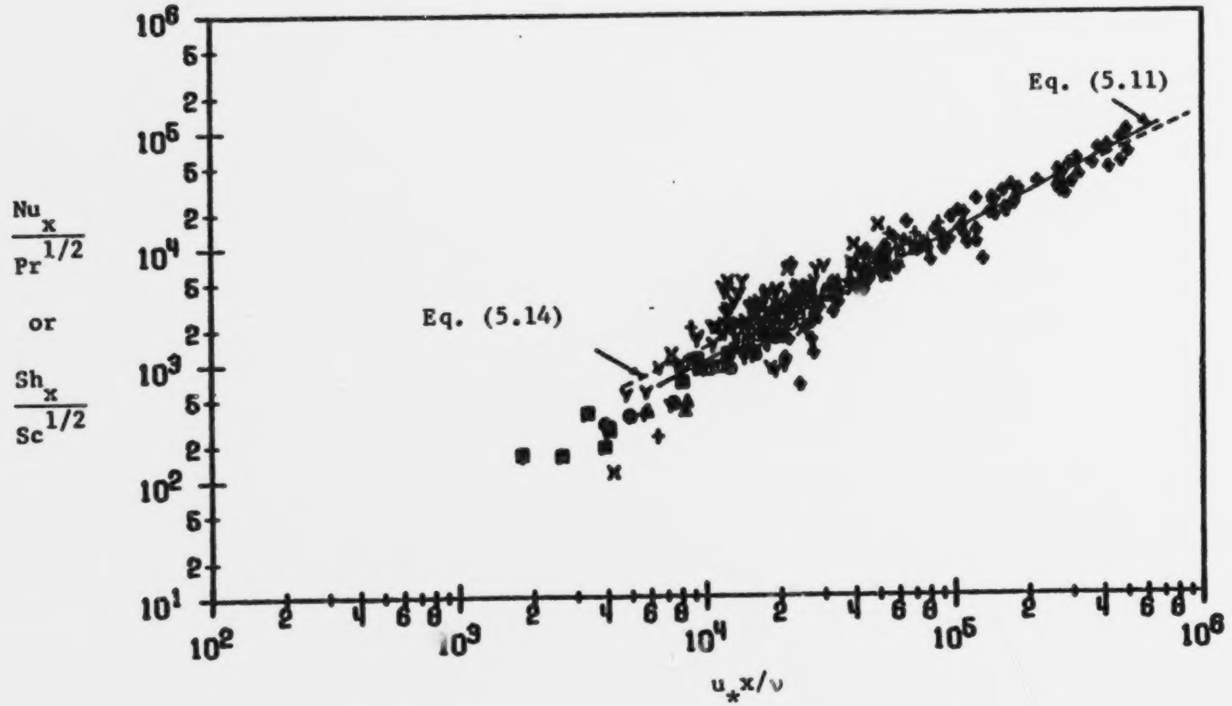

Figure 5.24 Nusselt Number vs. u_*x/ν with Eq. (5.11) and (5.14) Shown

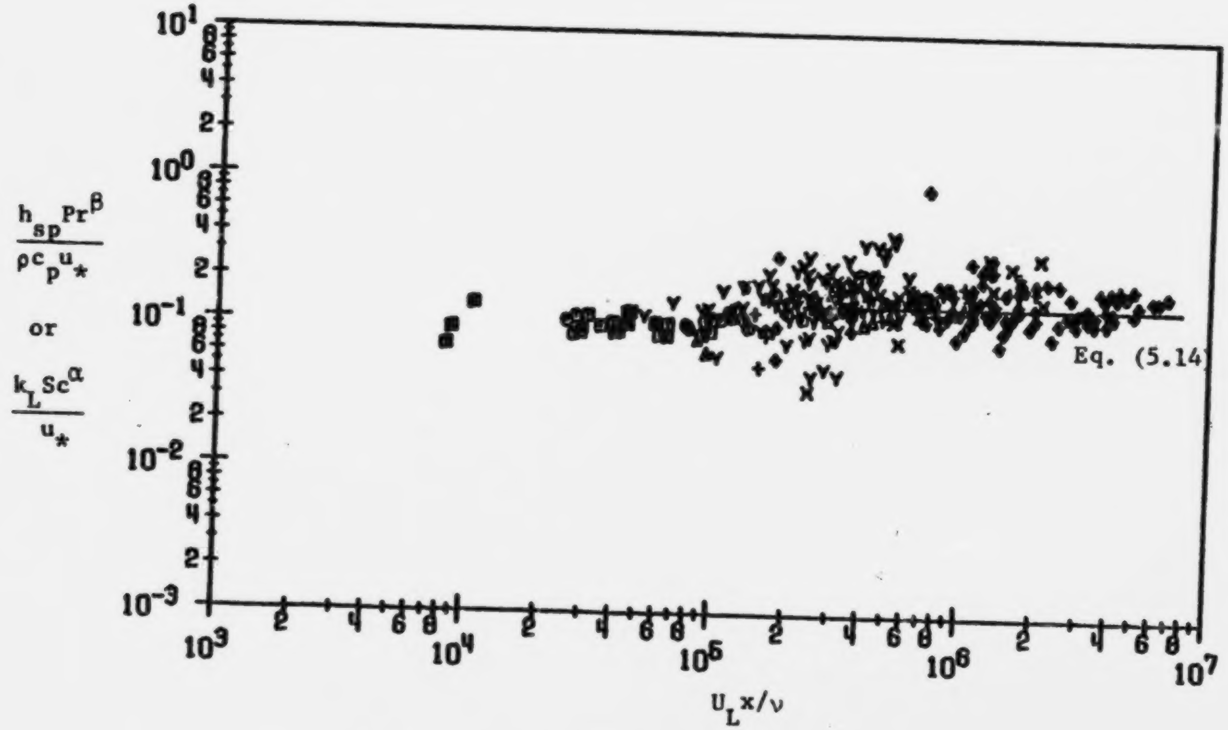

Figure 5.25 Present Correlation with Eq. (5.14) Indicated

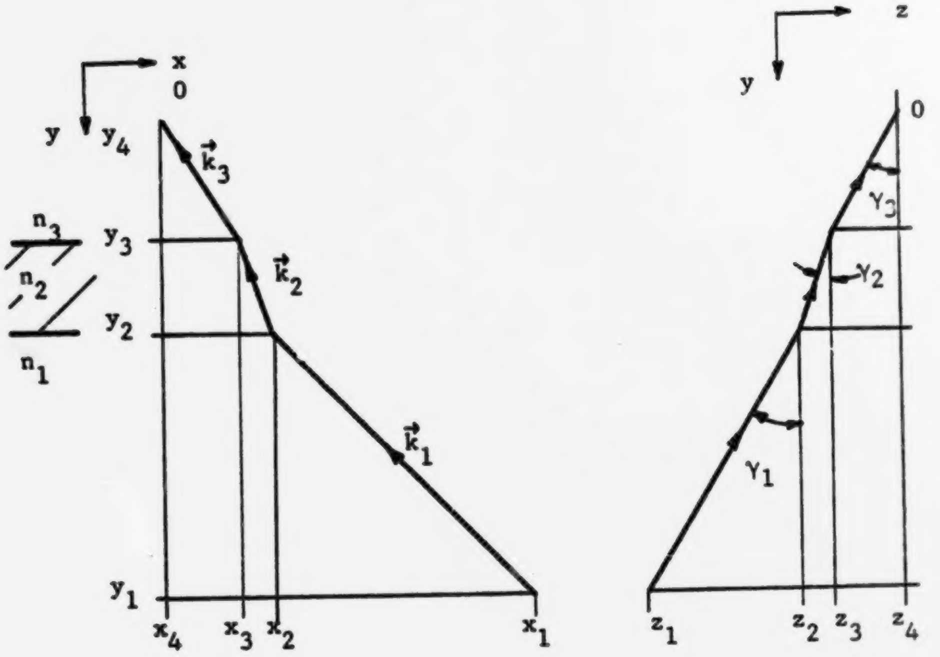
x
0
y
y_4
$\vec{k}_3$
n_3
y_3
n_2
$\vec{k}_2$
y_2
n_1
$\vec{k}_1$
y_1
x_4
x_3
x_2
x_1
z
y
0
γ_3
γ_2
γ_1
z_1
z_2
z_3
z_4

a) x-y projection

b) y-z projection

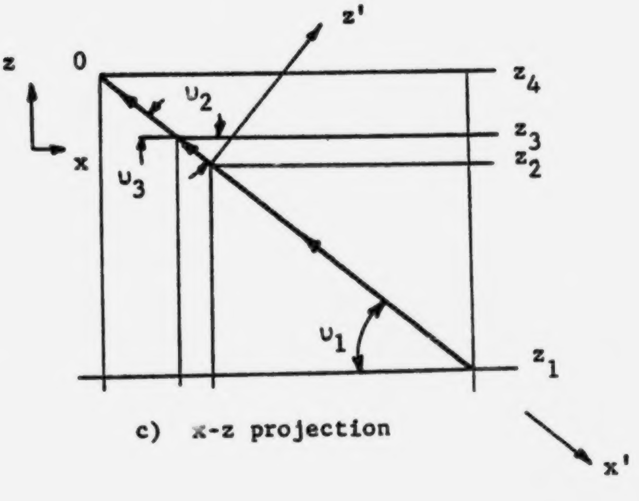
z'
z
0
z_4
υ_2
z_3
x
z_2
υ_3
υ_1
z_1
x'

c) x-z projection

Figure A.1 Incident Beam Geometry in Projection

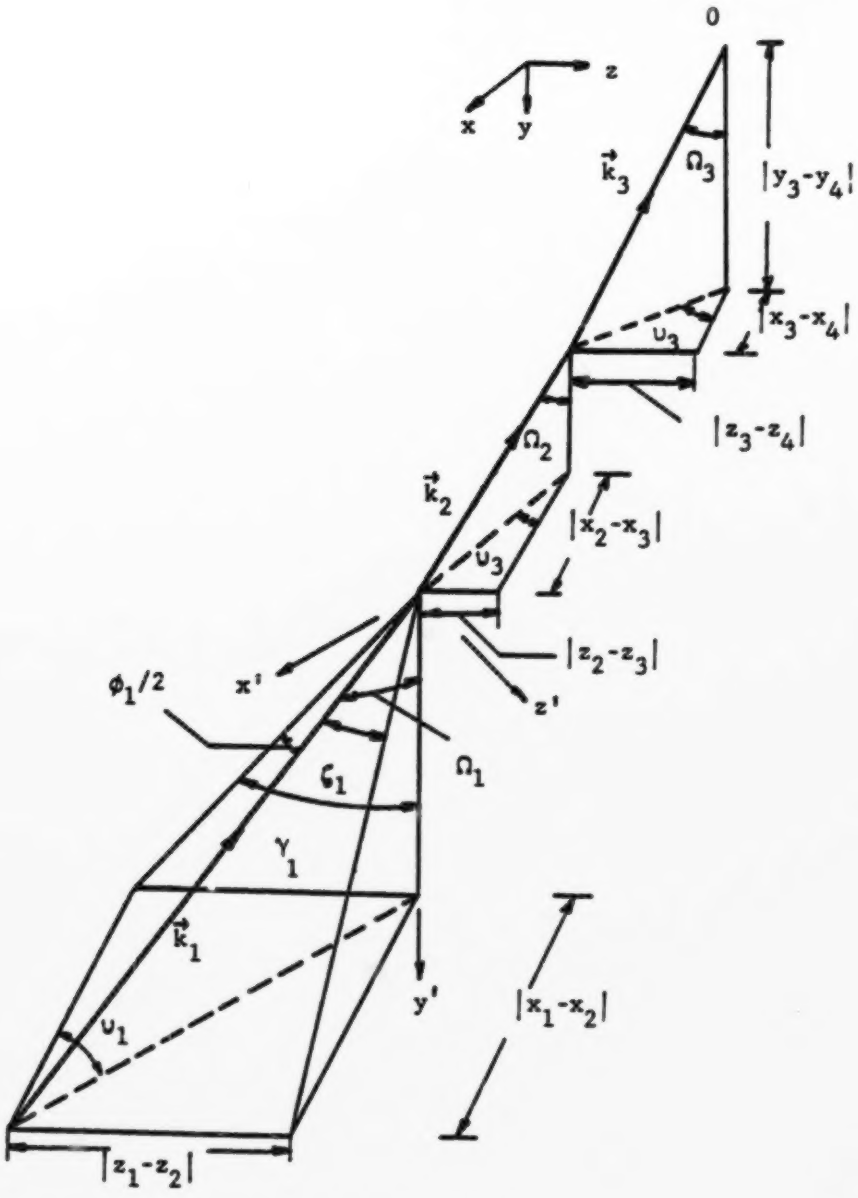
0
z
x
y
$\vec{k}_3$
Ω_3
$|y_3-y_4|$
$|x_3-x_4|$
υ_3
$|z_3-z_4|$
Ω_2
$\vec{k}_2$
$|x_2-x_3|$
υ_3
$|z_2-z_3|$
x'
z'
$\phi_1/2$
Ω_1
ζ_1
γ_1
$\vec{k}_1$
y'
$|x_1-x_2|$
υ_1
$|z_1-z_2|$

Figure A.2 Incident Beam Geometry in Perspective

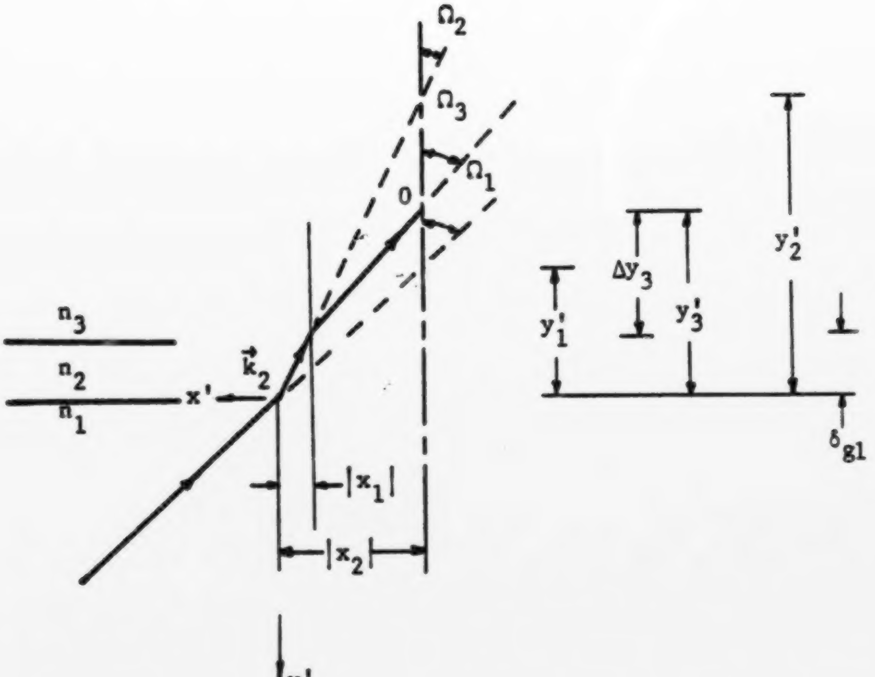

Ω_2
Ω_3
Ω_1
0
n_3
n_2
n_1
x'
$\vec{k}_2$
$|x_1|$
$|x_2|$
y'
y_1'
Δy_3
y_3'
y_2'
δ_{g1}

Figure A.3 Projection of Incident Beam in x'-y' Plane

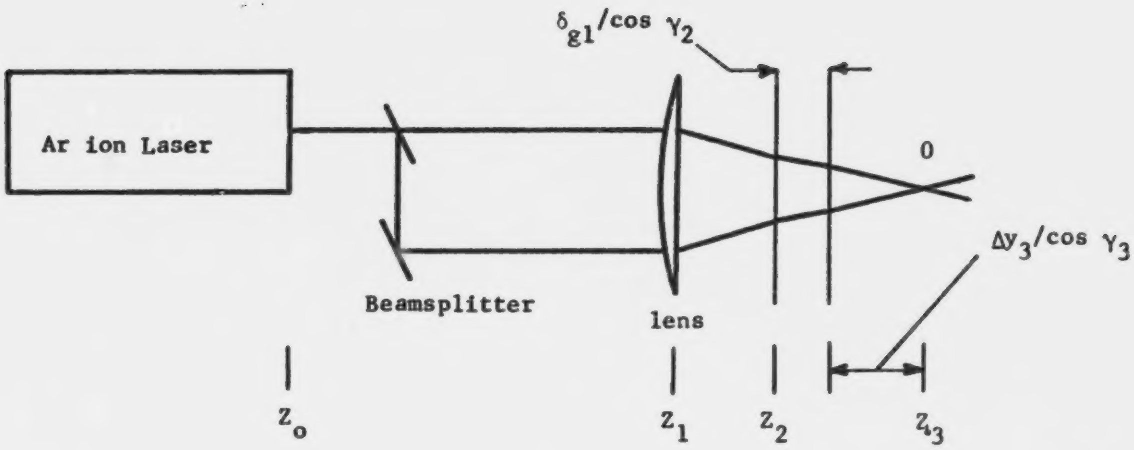
$\delta_{g1}/\cos\gamma_2$
Ar ion Laser
0
$\Delta y_3/\cos\gamma_3$
Beamsplitter
lens
Z_o
Z_1
Z_2
Z_3

Figure A.4 Incident Beam Path

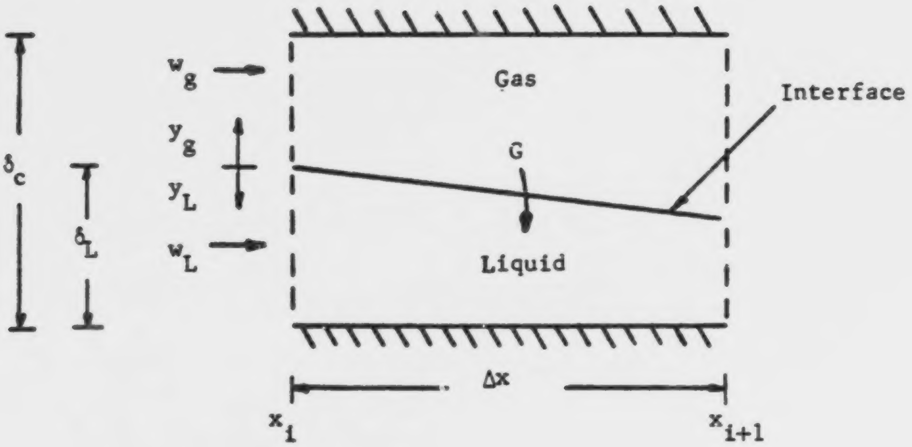

w_g
Gas
Interface
y_g
δ_c
G
y_L
δ_L
w_L
Liquid
Δx
x_i
x_{i+1}

Figure B.1 Geometry of Elements in Stratified Flow Integral Analysis

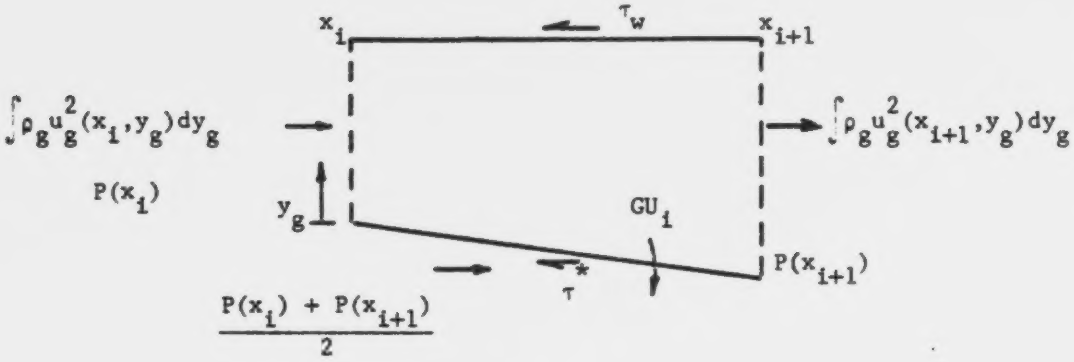

x_i
τ_w
x_{i+1}
$\int \rho_g u_g^2(x_i, y_g) dy_g$
$\int \rho_g u_g^2(x_{i+1}, y_g) dy_g$
$P(x_i)$
y_g
GU_i
$P(x_{i+1})$
τ^*
$\frac{P(x_i) + P(x_{i+1})}{2}$

Figure B.2 Force Balance on Element in Gas Phase

BEST DOCUMENT AVAILABLE

NRC FORM 335
(11-81)
U.S. NUCLEAR REGULATORY COMMISSION
BIBLIOGRAPHIC DATA SHEET

1. REPORT NUMBER *(Assigned by DDC)*
NUREG/CR-2334

4. TITLE AND SUBTITLE *(Add Volume No., if appropriate)*
Interphase Transport in Horizontal Stratified Cocurrent Flow

2. *(Leave blank)*

3. RECIPIENT'S ACCESSION NO

7. AUTHOR(S)
R.J. Jensen, M.C. Yuen

5. DATE REPORT COMPLETED
MONTH April YEAR 1982

9. PERFORMING ORGANIZATION NAME AND MAILING ADDRESS *(Include Zip Code)*
Department of Mechanical and Nuclear Engineering
Northwestern University
Evanston, IL 60201

DATE REPORT ISSUED
MONTH May YEAR 1982

6. *(Leave blank)*

8. *(Leave blank)*

12. SPONSORING ORGANIZATION NAME AND MAILING ADDRESS *(Include Zip Code)*
Division of Accident Evaluation
Office of Nuclear Regulatory Research
U.S. Nuclear Regulatory Commission
Washington, DC 20555

10. PROJECT/TASK/WORK UNIT NO

11. FIN NO
B6188

13. TYPE OF REPORT

PERIOD COVERED *(Inclusive dates)*

15. SUPPLEMENTARY NOTES

14. *(Leave blank)*

16. ABSTRACT *(200 words or less)*

The problem of interfacial transport in cocurrent, horizontal stratified gas-liquid systems is considered. Local condensation heat transfer coefficients and interface shear stress were obtained from mass and force balances. Based on cocurrent stratified air-water flow data, the noncondensing interface shear stress was found to be a function of the relative velocity between the phases and the liquid fraction. Incorporated into Linehan's relation for condensing flow shear stress, the correlation was found to estimate the shear velocity for the condensation data considered. Local condensation heat transfer coefficients and gas absorption mass transfer coefficients were found to be directly proportional to the shear velocity. If the inner scales u_* and ν/u_* are substituted into Lamont's models for the interface mass transfer coefficient, many features of the present correlation for scalar transfer are predicted. The correlations for interfacial shear stress and scalar transport can be combined to yield an iterative technique suitable for an engineering analysis of the interfacial heat, mass, and momentum transfer in a single driving force cocurrent system.

17. KEY WORDS AND DOCUMENT ANALYSIS

17a. DESCRIPTORS

17b. IDENTIFIERS/OPEN-ENDED TERMS

18. AVAILABILITY STATEMENT
Unlimited

19. SECURITY CLASS *(This report)*
Unclassified

20. SECURITY CLASS *(This page)*
Unclassified

21. NO OF PAGES

22. PRICE
$

NRC FORM 335 (11 81)

☆U.S. GOVERNMENT PRINTING OFFICE: 1982-361-297:2197

190